Microscopic Study of Some Deformed Atomic Nuclei in the Actinide Mass region

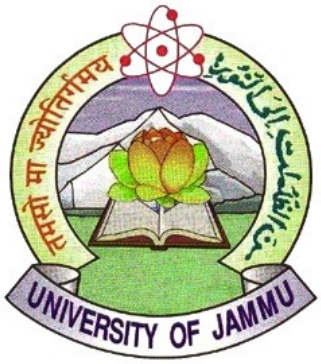

A THESIS

SUBMITTED TO THE UNIVERSITY OF JAMMU

FOR THE AWARD OF DEGREE OF

DOCTOR OF PHILOSOPHY

IN

PHYSICS

By

SAIQA SADIQ

Under the Supervision of

Dr. RANI DEVI

POST-GRADUATE DEPARTMENT OF PHYSICS & ELECTRONICS
UNIVERSITY OF JAMMU
JAMMU-180006

(June-2016)

DECLARATION

I, **Saiqa Sadiq**, declare that the work reported in this thesis has entirely been done by me under the supervision of Dr. Rani Devi, Department of Physics & Electronics, University of Jammu, Jammu. No part of this work has been submitted in part or full for a degree in any other university.

Dated: **(Saiqa Sadiq)**

POST-GRADUATE DEPARTMENT OF PHYSICS & ELECTRONICS, UNIVERSITY OF JAMMU
JAMMU-180006

CERTIFICATE

It is certified that **Ms. Saiqa Sadiq,** worked under my supervision and the work is worthy of consideration for the award of Ph. D. degree in Physics. It is further certified that:

(i) the thesis embodies the work of the candidate herself.

(ii) the candidate worked under my supervision for the period required under statutes.

(iii) the candidate has put in the required attendance in the department.

(iv) the candidate has fulfilled the statutory conditions as laid down in Section 18 of statutes governing degree of Doctor of Philosophy issued vide notification no. 4 dated 04.03.2013.

Prof. Vivek K Gupta
Head of Department

Dr. Rani Devi
Research Supervisor

ACKNOWLEDGEMENTS

First of all, I would like to express my profound sense of gratitude and sincere thanks to the highly esteemed ***Prof. S.K. Khosa*** (Head, Department of Physics and Astronomical Sciences Central University Jammu) who is founder member of Nuclear Theory Group in the Department of Physics and Electronics, University of Jammu, for his expert guidance, enlightening discussions and versatile knowledge. My research work would never be completed without his efforts.

I would also like to express my sincere gratitude to my supervisor ***Dr. Rani Devi***. Her guidance helped me in time of research and writing of this thesis.

Warm thanks to ***Dr. Arun Bharti,*** Professor of Physics, for his valuable advice.

It is my pleasure to acknowledge my thanks to ***Prof. Vivek Gupta*** Head of the Department of Physics and Electronics for providing me the necessary research facilities from time to time.

I would like to thank all the non-teaching staff members of the department for friendly behavior, helpful attitude and good will.

I would also like to thanks to all the esteemed faculty members of the department. I am also deeply thankful to research scholars *Dr. Rawan Kumar, Dr. Neeraj Gupta, Dr. Gopal Krishan*, *Dr. B. D. Sehgal*, *Dr. Daya Ram, Dr. Arvind Bhat, Mr. Rakesh Kumar Pandit, Mr. Shikshit Gupta*, *Mr. Jagjit Singh*, *Mr. Barun Slathia*, *Ms Ritu Choudhary, Mrs. Rohini Sharma, Ms Annu Gupta, Mrs. Deepti Sharma, Mr Narotam Singh* and *Mr. Ajay Kumar Sharma,* for their help during my Ph.D. work.

It was the vision and deep desire of my father Late *Mr. Sadiq Hussain* that actually get translated into my PhD. work. His inspiring thoughts, words, memories and blessing keeps me motivating in the journey of my PhD. Work.

I am highly thankful to *Mr. Mudasir Iqbal, Mr. Younis Zubair, Mrs Meghna Bhat and Mrs Poonam Kotwal,* for their best wishes and moral support.

I express a heartfelt thanks to my mother for her best wishes and moral support. I also express my thanks to my mother-in-law and specially father-in-law *Mr. Mohd Iqbal* for his good will, care, best wishes and moral support. Without his support it was not possible for me to complete my work.

I acknowledge with love to my little master ***Fauzan Nasir*** who spared his crucial time for my research work and my husband ***Mr. Nasir Iqbal***. His patience, care, and good will helped me to complete my doctoral research. Thanks to both of you from the deep core of my heart. I also express a heartfelt thankful to our fifth Khalifa (Huzrat Mirza Masroor Ahmed Sahib) for his good wishes. Finally, I thank Allah for all the good He has done to me through everyone in one or the other way.

SAIQA SADIQ

CONTENTS

List of Tables iii

List of Figures v

List of Publications vii

Abstract ix

Chapter 1 Introduction

1.1 Introduction 1

Chapter 2 Projected Shell Model study of even-even Uranium and Plutonium nuclei

2.1 Introduction 11

2.2 Calculational details 13

2.2.1 Projection operator 14

2.2.2 Shell model in projected basis 16

2.2.3 Semi classical limit 19

2.2.4 Projected shell model 22

2.2.5 Choice of the Hamiltonian 25

2.3 Results and discussion for even-even $^{230\text{-}240}$U and $^{236\text{-}242}$Pu isotopes 30

2.3.1 Deformation systematics of $^{230\text{-}240}$U 30

2.3.2 Deformation systematics of $^{236\text{-}242}$Pu 31

2.3.3 Yrast bands of $^{230\text{-}240}$U 32

2.3.4 Yrast bands of $^{236\text{-}242}$Pu..... 32

2.3.5 Structure of yrast bands of $^{230\text{-}240}$U 33

2.3.6 Structure of yrast bands of $^{236\text{-}242}$Pu 35

2.3.7 Electromagnetic quantities 36

2.3.7.1 B(E2) transitions probabilities of $^{230\text{-}240}$U…36

2.3.7.2 B(E2) transitions probabilities of $^{236\text{-}242}$Pu…37

2.3.7.3 g-factors of $^{230\text{-}240}$U 37

2.3.7.4 g-factors of $^{236\text{-}242}$Pu 38

2.4 Summary 39

Chapter 3 Projected Shell Model study of Curium isotopes

3.1 Introduction 63

3.2 Theoretical Framework 65

3.3 Results and discussion for even-even $^{242\text{-}248}$Cm isotopes ... 65

3.3.1 Yrast Spectra 65

3.3.2 Structure of yrast states of even-even $^{242\text{-}248}$Cm 66

3.3.3 Electromagnetic quantities 68

3.3.3.1 B(E2) transition probabilities 68

3.3.3.2 g-factors 68

3.4 Results and discussion for odd-A $^{243\text{-}247}$Cm isotopes 69

3.4.1 ^{243}Cm 69

3.4.2 ^{245}Cm 69

3.4.3 ^{247}Cm 70

3.5 Summary 70

Chapter 4 Summary of the work done 90

Bibliography 93

LIST OF TABLES

Table 2.1 Quadrupole and hexadecapole deformation parameters used in the present calculations for $^{230\text{-}240}$U isotopes 41

Table 2.2 Comparison of experimental (Exp.) and calculated (Th.) excitation energies (in units of MeV) of $2_1^+(E_2^+)$, $4_1^+(E_4^+)$ and E_4^+/E_2^+ ratios for $^{230\text{-}240}$U isotopes 41

Table 2.3 The BCS sub-shell occupation numbers of protons in the ground state of $^{230\text{-}240}$U isotopes 42

Table 2.4 The BCS sub-shell occupation numbers of neutrons in the ground state of $^{230\text{-}240}$U isotopes 43

Table 2.5 Quadrupole and hexadecapole deformation parameters used in the present calculations for $^{236\text{-}242}$Pu isotopes 44

Table 2.6 Comparison of experimental (Exp.) and calculated (Th.) excitation energies (in units of MeV) of $2_1^+(E_2^+)$, $4_1^+(E_4^+)$ and E_4^+/E_2^+ ratios for $^{236\text{-}242}$Pu isotopes 44

Table 2.7 The BCS sub-shell occupation numbers of protons in the ground state of $^{236\text{-}242}$Pu isotopes 45

Table 2.8 The BCS sub-shell occupation numbers of neutrons in the ground state of $^{236\text{-}242}$Pu isotopes 46

Table 2.9 Comparison of calculated (Th.) and experimental (Exp.) *B(E2)* reduced transition probabilities (in units of e^2b^2) for $^{230\text{-}240}$U isotopes 47

Table 2.10 Comparison of calculated (Th.) and experimental (Exp.) *B(E2)* reduced transition probabilities (in units of e^2b^2) for $^{236\text{-}242}$Pu isotopes 48

Table 3.1 Quadrupole and hexadecapole deformation parameters used in the present calculations of $^{242-248}$Cm isotopes 72

Table 3.2 Comparison of calculated (Th.) and experimental (Exp.) *B(E2)* reduced transition probabilities (in units of e^2b^2) for $^{242-248}$Cm isotopes 72

LIST OF FIGURES

Figure 2.1 Comparison of calculated (Th.) and experimental (Exp.) positive-parity yrast bands of even-even $^{230\text{-}240}$U isotopes ... 49

Figure 2.2 Comparison of calculated (Th.) and experimental (Exp.) positive-parity yrast bands of even-even $^{236\text{-}242}$Pu isotopes..... 50

Figure 2.3 Band diagrams (bands before configuration mixing) for (a) ^{230}U, (b) ^{232}U, (c) ^{234}U, (d) ^{236}U, (e) ^{238}U, (f) ^{240}U isotopes. Only the important lowest lying bands in each configuration are shown 51-56

Figure 2.4 Band diagrams (bands before configuration mixing) for (a) ^{236}Pu, (b) ^{238}Pu, (c) ^{240}Pu and (d) ^{242}Pu. Only the important lowest lying bands in each configuration are shown 57-60

Figure 2.5 Theoretical *g*-factors as a function of angular momentum for $^{230\text{-}240}$U isotopes. Comparison between calculated (Th.) and Experimental (Exp.) g-factors for ^{238}U is also presented 61

Figure 2.6 Theoretical *g*-factors as a function of angular momentum for $^{236\text{-}242}$Pu isotopes..... 62

Figure 3.1 Comparison of calculated (Th.) and experimental (Exp.) positive-parity yrast bands of $^{242\text{-}248}$Cm isotopes 73

Figure 3.2 Comparison of calculated (Th.) and experimental (Exp) transition energies [E(I)-E(I-2)] versus spin for even-even $^{242\text{-}248}$Cm isotopes 74

Figure 3.3 Band diagrams for (a) ^{242}Cm, (b) ^{244}Cm, (c) ^{246}Cm, (d) ^{248}Cm isotopes 75-78

Figure 3.4 Theoretical g-factors as a function of angular momentum for $^{242-248}$Cm isotopes 79-80

Figure 3.5 Comparison of calculated (Th.) and experimental (Exp.) energy levels for ground state band (A) and excited band (C) of positive-parity of ^{243}Cm 81

Figure 3.6 Band diagram of ^{243}Cm 82

Figure 3.7 Comparison of calculated (Th.) and experimental (Exp) transition energies [E(I)- E(I-1)] versus spin for ^{243}Cm 83

Figure 3.8 Comparison of calculated (Th.) and experimental (Exp.) energy levels for ground state band (A) and excited bands (C) of positive-parity band of ^{245}Cm 84

Figure 3.9 Band diagram of ^{245}Cm 85

Figure 3.10 Comparison of calculated (Th.) and experimental (Exp) transition energies [E(I)-E(I-1)] versus spin for ^{245}Cm 86

Figure 3.11 Comparison of calculated (Th.) and experimental (Exp.) energy levels for ground state negative parity band of ^{247}Cm 87

Figure 3.12 Band diagram of ^{247}Cm 88

Figure 3.13 Comparison of calculated (Th.) and experimental (Exp) transition energies [E(I)-E(I-2)] versus spin for ^{247}Cm 89

Chapter 1
Introduction

1.1 Introduction

The atomic nucleus is the core of the atom having dimensions of the order of fermi and contains protons and neutrons which are the charged states of nucleons. A nucleus can be thought of as a unique quantum many body system that exhibits three modes of excitations namely rotational, vibrational and single-particle excitation modes. In spherical nuclei, the vibrational modes can be excited and are studied by using the harmonic phonon model [1, 2]. In deformed nuclei, vibrational motion is possible around equilibrium of a deformed shape configuration. The deformed intrinsic shape is usually parameterized in terms of β and γ deformation variables. These parameters are related to the axial and non-axial shapes of a deformed nucleus. The one-phonon vibrational mode in deformed nuclei with no component of angular momentum along the symmetry axis (K=0) is called β-vibration and the vibrational mode with component of angular component along the symmetry axis (K=2) is referred to as γ-vibration. The rotational bands based on the γ-vibrational state are known as γ-bands [3-6].

The interest in nuclear physics became a passion with the availability of energetic heavy ion beams that opened up an enormous possibility of investigating various macroscopic as well as microscopic features of collision processes involving complex nuclei far away from the line of β-stability. In low energy heavy ion collisions, it has been found that, apart from direct reactions on the one hand, and highly complex compound nucleus reactions on the other, there are also a host of processes which are intermediate between the two extremes and have become possible to study. The study of these intermediate processes, broadly categorised as damping nuclear reactions play a crucial role in understanding the relaxation mechanisms of various collective nuclear degrees of freedom vis-à-vis the reaction mechanisms between complex nuclei from a more fundamental, microscopic point of view.

With the development of sophisticated, high precision measuring devices, it became possible to investigate the properties of nuclei far away from the line of β-stability. In the early 1980's fusion evaporation reactions became the standard tool to populate very high spin states in nuclei that were not previously accessible to investigation [7-17]. In this technique, two stable nuclei are brought together at energy above the Coulomb barrier; the resulting compound system subsequently evaporates nucleons before decaying by γ-ray emission. However, such a process produces nuclei on the neutron-deficient side of the valley of stability. This is because stable light nuclei such as the target and projectile have a lower N/Z ratio compared to the heavy stable nuclei. In addition, the compound system preferentially emits neutrons, leaving a more neutron-deficient nucleus. The γ- and proton-emission channels are less probable for heavy compound nuclei near stability. In order to produce nuclei that are more neutron-rich with this technique, radioactive beams can be used.

The study of decay schemes from fusion evaporation reactions has greatly enhanced our understanding of nuclear structure. It has led to the discovery of collective rotational bands in regions far away from the line of β-stability. Apart from this, for more than a decade in the past, deep inelastic heavy ion reactions have been employed for spectroscopic studies of nuclei located at the neutron rich edge of the β-stability valley and beyond [18-24]. The high quality gamma coincidence data obtained in thick target experiments performed with the available large arrays of germanium detectors allow to achieve selectivity which is satisfactory to identify structures of many unknown nuclei.

Nuclear structure is also investigated by in beam spectroscopy. In in-beam spectroscopy the beam is incident on the product target which is surrounded by a spectrometer to detect the prompt radiation, typically a ball of germanium detectors for γ-ray spectroscopy such as GAMMASPHERE, JUROGAM, or a conversion-electron spectrometer such as SACRED [25,26]. In addition, nuclear structure is also investigated by various experimental techniques that include γγ, e-γ, e-e coincidence measurements, coulomb excitation, discrete γ-ray spectroscopy with heavy ions, and advance time delayed βγγ (t) method [27-31].

The study of heavy elements has been approached through decay spectroscopy and limited particle number transfer reaction experiments. It gives information on the limited number of nuclear states, and is subjected to the selective nature of the decay processes and reaction mechanisms. The field of decay spectroscopy has developed in recent years from technological development of multi-detector systems. The application of in-beam techniques to heavy nuclei can give access to a range of experimental observables which compliment the information from decay spectroscopy. It is now possible to study rotational bands which in-turn give the information about deformation, collectivity, and pairing. At high spins, rotational alignment properties and blocking arguments can give insight into particles active at the Fermi surface.

The heaviest doubly magic nucleus found in nature is ^{208}Pb, which has 82 protons and 126 neutrons. This nuclide also marks as border line of nuclear stability. It was a challenge for the theorists to investigate whether magic proton or neutron numbers would exist beyond Z =82 and N =126, respectively, and what would be the properties of nuclei in that region, since locally enhanced nuclear stability could be expected.

The first prediction of the next spherical closed proton and neutron shell at Z =114 and N =184 was presented by Meldner at the Lyrekil Conference [32]. This initiated a long series of experiments designed not only to synthesize such nuclei in the laboratory but also to search for them in nature, which seemed reasonable considering the long half lives predicted. New predictions of nuclear stability resulted in modifying nuclear life by several orders. But the location of the nuclear shells has not changed essentially. The maximum shell corrections are still obtained at Z =114 [33, 34] and corresponding neutron numbers slightly differs resulting in N= 182 or N =178 [33, 34]. Nuclei in that region however are not spherical but strongly deformed, having substantial quadrupole deformation (β_2) and hexadecapole deformation (β_4) [33, 34]. To understand the properties of nuclei in this region, it is very important to study the properties of nuclei in the actinide mass region as they are the heaviest known quasi-stable nuclei that have been synthesized and observed.

The most common practical significance of the actinides arises from the fissionability, or potential for splitting certain of their isotopes. When an atomic nucleus

breaks apart, or undergoes fission, enormous amounts of energy and several neutrons are liberated. This energy can be used to generate an atomic explosion, or it can be controlled and used as a fuel to generate heat for the production of electrical power. There is a potential for an enormous electrical energy production inherent in nuclear energy-generating technologies, and since the actinide elements are the only known fissionable materials, the practical impact of their availability is great. Other fissionable isotopes of great importance are ^{233}U, ^{239}Pu and ^{241}Pu. Fissionable Plutonium isotopes are formed as by-products of fission in reactors using Uranium; when neutrons are added to ^{238}U, which is not itself fissionable, and it is converted to the fissionable isotope ^{239}Pu. The heavier actinides, those beyond Plutonium in the periodic table are of interest principally to research scientists, though they have some potential practical uses as sources of thermoelectric heat and neutrons.

A brief overview of the experimental and theoretical studies of Uranium, Plutonium and Curium mass chains are presented in the following paragraphs.

Multiple coulomb excitation of ^{234,236}U by 5.3 MeV/u ^{208}Pb ions by using gamma ray spectroscopy has been studied by Ower *et al*. [35]. They have observed the excitation of levels of the ground state band of ^{234,236}U up to spins I=26$^+$ and 28$^+$, respectively. Transition energies between ground state band levels of these nuclei have also been studied by them, suggesting that at $I\approx28^+$ several units of angular momentum are carried by single particles aligned with the rotational axis. They have discussed their experimental results by using the concept of rotational alignment and compared them with predictions of the rotation-vibration and Interacting Boson Model. The gamma ray spectroscopy of states populated in multiple coulomb excitation has been performed by Ward *et al*. [36]. They have obtained the ground state band of ^{238}U up to spin 30$^+$ and compared their experimental data with cranked random phase approximation calculations. These calculations described well the low spin properties of the positive parity bands but the high spin states could not be explained satisfactorily. The transuranium nuclei on the neutron rich side on the β-stability line have scarcely been studied because of experimental difficulty. Ishii et al. [37-39] have measured in beam γ-rays in the neutron rich ^{240}U, ^{246}Pu and ^{250}Cm produced by the (^{18}O,^{16}O) two neutron

transfer reaction by selecting the reaction channel completely, using high resolution Si detectors. They have obtained the level energy of the ground state band up to spin I=12^+. The g-factors of the high spin yrast states in ^{238}U have been measured by Hausser *et al.* [40]. They have found the first evidence for the onset of proton alignment of $i_{13/2}$ protons at spin *I*= (18-24). The existence of ground state rotational bands with identical transition energies up to spin *I*= 8ħ in ^{244}Cm and ^{246}Cm have been observed by Ahmad *et al.* [41]. They have found that the importance of these bands is that the single particle states are well characterized at normal deformation and hence there is a better chance of understanding the underlying physics in these identical bands. They provide an ideal first test for calculations which attempt to explain identical bands. States with higher spin than 8ħ have not been observed in the nuclei ^{240}Pu, ^{244}Cm and ^{246}Cm because these nuclei are difficult to produce by fusion reactions and available structure information comes from radioactive decay studies. However, high spin states in ^{232}Th [35, 42] $^{234\text{-}238}$U [35, 43], ^{242,244}Pu [44] and ^{248}Cm [45] have been identified in coulomb excitation studies. The *E2* transition matrix elements of ^{248}Cm nucleus involving the ground band states up to spin 24^+ by coulomb excitation using 641 MeV ^{136}Xe and 260 MeV ^{58}Ni projectiles have been extracted by Czosnyka *et al*. [45]. They have also measured static electric quadrupole moments up to spin 20^+. Piercey *et al*. [46] have studied ground state band of ^{248}Cm up to spin 28^+ by observing γ-rays following multiple coulomb excitation with use of ^{208}Pb ions at 5.3 MeV/u. These authors have found that a smooth, gradual increase in the effective moment of inertia is seen at lower spin with an anomalous forward bend above spin 22^+.

Spectroscopy of the heavy nuclei up to high spin states is challenging. Most of the studies have been focused on collective structure of even-even nuclei [47, 48]. They are easier to investigate but the information on odd-A nuclei allows for more sensitive tests of theoretical predictions of single particle energies, moment of inertia, electromagnetic quantities. There are few predictions on high spin properties of odd-A nuclei [49]. Tandel *et al.* [50] have identified rotational bands in the odd-A nuclei ^{247,249}Cm and ^{249}Cf up to high spins. They have provided detailed information on high spin collective structure in ^{247}Cm and have found that υ[734]9/2 is the highest-lying neutron configuration investigated up to high spin. Braid *et al*. [51] have determined the

properties of states in ^{243}Cm, ^{245}Cm, ^{247}Cm by (d,p) and (d,t) reactions on targets of ^{244}Cm, ^{246}Cm and ^{248}Cm. They have made assignments of 1-qp states. Single-particle level schemes are extracted from the data by use of a pairing calculation. The extracted single particle level scheme is compared with the single particle calculations, which include β_4 and β_6 deformations. They have also estimated the equilibrium values of β_2, β_4 and β_6 for the odd mass Cm isotopes. Hota *et al.* [52] have studied ^{247}Cm through inelastic excitation and transfer reactions with radioactive targets. They have observed that the ground state band in ^{247}Cm is built on a $\nu j_{15/2}[734]9/2^-$ Nilsson configuration. Ahmed *et al*. [53] have measured α particle, conversion-electron and γ-ray spectra of ^{251}Cf with high resolution semiconductor detectors. They have measured α-γ coincident and level half-life measurements. On the basis of these measurements the following single-particle states have been identified in ^{247}Cm: $9/2^-[734]$, 0 KeV; $5/2^+[622]$, 277.4 KeV; $7/2^+[624]$, 285.4 KeV; $1/2^+[620]$, 404.9 KeV; $1/2^+[631]$, 518.6 KeV. Abharam *et al*. [54] have employed electron paramagnetic resonance (EPR) spectroscopy in making the first direct measurements of the nuclear spins of ^{243}Cm and ^{247}Cm (I=5/2 and I =9/2), respectively. They have obtained nuclear moments for ^{243}Cm as $\left|0.4\mu_N\right|$ and $\left|0.36\ \mu_N\right|$ for ^{247}Cm. Yates *et al*. [55] have measured life times of the *E2* transition from the $1/2^+[631]$ state to the $5/2^+[622]$ state in several actinide nuclei using pulse beam and delayed coincidence techniques. The $1/2^+[631]$ level was excited in ^{239}U and ^{243}Pu by the (d, p) reaction and in ^{241}Pu by (d, t) reaction and the subsequent γ decay to the $5/2^+[622]$ level was observed between beam pulse. They have observed corresponding *E2* transitions in ^{243}Cm and ^{245}Cm from the radioactive decay of ^{243}Bk and ^{245}Bk, respectively and also determined life time from electron-proton delay coincidence experiments. From these measurements, the half-lives obtained are ^{239}U (0.78±0.04μs), ^{241}Pu (0.88±0.05μs), ^{243}Pu (0.33±0.03μs) and ^{245}Cm (0.29±0.02μs).

On the theoretical side the ground state energies, first excited states, and deformation parameters of a wide range of heavy to the super heavy nuclei were calculated in a macroscopic-microscopic approach by Sobieweski *et al*. [56]. The Yukawa-plus-exponential model is taken for the macroscopic part of energy and the Strutinsky shell correction is used for the microscopic part. Detailed predictions for the even mass isotopic chains $^{226\text{-}236}$Th and $^{226\text{-}242}$U are given with the minimum of excitation

energy of the first excited 2^+ state and a maximum of deformation energy at N=144, 146. A macroscopic-microscopic model based on the Lublin-Strasbourg, the Strutinsky shell-correction method, and the Bardeen-Cooper Schrieffer approach for pairing correlations was used with the cranking model by Nerlo-Pomorska *et al*. [57]. They have taken into account a dynamical coupling of rotation with the pairing field. The results describe the rotational bands in even-even Radium to Copernicium isotopes. Vretenar *et al*. [58] have obtained results on sequence of heavy nuclei from Thorium to Nobelium within self consistent relativistic Hartree Bogolyubov mean-field calculations. From these calculations they have provided a unified description of particle hole and particle-particle correlations. They have also predicted the ground state axial quadrupole and hexadecapole moments along the isotopic chains of various actinide nuclei. Kumar *et al.* [59] have calculated the ground, first intrinsic excited states and density distribution of neutron rich Thorium and Uranium isotopes within framework of relativistic mean field approach. They have analysed possible modes of decay like α-decay and β-decay and found that neutron rich isotopes are stable against α-decay and unstable against β-decay. They have also predicted the lifetime of the nuclei to be tens of second against β-decay.

The ground state band and the low-lying alternative parity bands in the heaviest nuclei are calculated within a cluster model by Shneidman *et al.* [60]. The model is based on assumption that reflection asymmetric shapes are produced by the motion of nuclear system in the mass asymmetric coordinates. They have obtained detailed results on the levels of the ground-state rotational bands and low-lying alternative parity bands in the heaviest nuclei. Calculations of moments of inertia have been performed for actinide nuclei by Brack *et al* [61] using quasiparticle formalism. These calculations reproduce the observed moments of inertia within 10% only. For example, the ratios of theoretical moments of inertia to experimental values are 1.11 (^{236}U), 1.00 (^{238}U), 0.96 (^{240}Pu), 1.00 (^{244}Cm), 1.10(^{246}Cm) and 0.89(^{250}Cf) have been reported. In these calculations the moments of inertia were shown to be very sensitive to the pairing interaction, which was not adjusted to reproduce the moments of inertia. The calculation indicates that it is difficult to reproduce the moments of inertia to the experimental accuracy for the ground-state bands. Afanasjev *et al.* [62, 63] have employed cranked relativistic Hartree Bogoliubov calculations for a systematic study of pairing and normally deformed

rotational bands of even-even and odd-mass actinides. The calculations have been performed with the NL1 and NL3 parameterization of the relativistic mean-field Lagrangian. Pairing correlations are taken into account by Brink-Booker part of the finite-range Gogny DIS force. The stabilization of the octupole deformation at high spin is suggested by an analysis of discrepancies between theory and existing experimental information in the band crossing region of A ≈ 240 nuclei. Muntian *et al*. [64] have studied rotational structure in very heavy nuclei by employing cranking approximation based on a macroscopic-microscopic approach.

The first microscopic calculations in the framework of the Hartree-Fock-Bogoliubov approximation was carried out by Egido and Robledo [49], in which properties of the ground state rotational band in ^{254}No were discussed. Khudair *et al*. [65] have performed Projected Shell Model (PSM) with deformed single particle states generated by the standard Nilsson potential. They have studied systematical behaviour of rotational-alignment and associated band crossing phenomena in Cf, Fm and No isotopes. They have found that neutrons and protons from high *j* orbits are found to compete strongly in rotational-alignment. They suggested that the observation of these effects will provide direct information on the single-particle states in the heaviest nuclear mass region. The microscopic study of yrast line in well deformed actinide nuclei have been performed by Egido and Ring [66]. They have discussed several versions of the cranking model and applied it to reproduce the alignment and band crossing pattern at the yrast line. The energy spectra and *B(E2)s* of $^{232\text{-}238}$U have been calculated by Chiang *et al.* [67] in the interacting boson plus fermion model. They have found that in order to reproduce the identical energy bands, weak boson pairing, a weak angular momentum interaction and a strong quadrupole interaction are needed in these nuclei. Zhang *et al*. [68] have investigated rotational bands in nuclei with $Z = 96$ by using cranked shell model (CSM) with the pairing correlations treated by particle-number conserving (PNC) method. A new set of Nilsson parameters and deformation are proposed by fitting experimental single particle spectra in nuclei with $Z= 96$. They have also calculated bandhead energies of the 1-qp bands in odd-A nuclei by PNC-CSM (cranked shell model) method. Zhang *et al.* [69] have also investigated odd-A ^{247}Cm nucleus by using CSM with pairing correlations treated by PNC method. They have found that the experimental moments of inertia,

alignments and their variations with rotational frequency ω are reproduced well by PNC-CSM calculations. Neutron one-quasi-particle states of $^{243-247}$Cm nuclei have been calculated by Parkhomenko and Sobiczewski [70] by using macroscopic-microscopic approach. They have considered even *Z* and odd *N* nuclei with *Z*=96. They have found that the characteristics of the experimental known ground states are well reproduced. The rotational properties of actinide nuclei in the cranked HFB model with pairing and quadrupole interaction have been studied by Ploszajczale and Faessler [71]. They have found that the $i_{13/2}$ protons are mainly responsible for causing the gradual increase of moment of inertia in ^{236}U. Shirikov *et al*. [72] have performed the calculations of the excitation energies and the wave functions of the low-lying states of the nuclei with *Z* =96 by using quasi-particle phonon model and have found that the excitation of the phonons and quasi-particle phonon interaction play an important role in the description of the properties of the excited states of these nuclei with *Z* = 96

Single particle states in odd-*A* actinide nuclei using the reflection asymmetric mean field approach with an average Woods Saxon potential and monopole residual interaction have been calculated by Cwiok and Nazarewicz [73]. They have found that the deformed Woods Saxon model gives over all agreement to single particle band heads in reflection symmetric actinide nuclei and also found that the calculated symmetry energies in the odd-*A* nuclei are generally larger than those calculated for the neighbouring even-even cores.

In this thesis, the Projected Shell Model has been employed to study the nuclear structure properties of even-even Uranium, Plutonium and Curium nuclei and also some odd-*A* Curium isotopes.

The organisation of the present thesis is as follows:

Chapter 2 is devoted to the study of some Uranium and Plutonium isotopes. The results have been obtained for yrast energy levels, *B(E2)* transition probabilities and *g*-factors. The results of BCS subshell occupation numbers indicate that deformation systematics in Uranium and Plutonium isotopes depend on the occupation of low *k* components of high "*j*" orbitals in the valence space and polarization of ($1h_{11/2}$) proton orbit. The calculation

reproduced the observed positive parity yrast bands. The low lying states of yrast spectra have been found to arise from 0-qp intrinsic states whereas the high spin states arise from multi-quasiparticle bands. The calculated $B(E2; 2_1^+ \longrightarrow 0_1^+)$ values are in good agreement with experimental data for all Uranium and Plutonium isotopes. The present calculations has predicted the B(E2) values for higher transitions for $^{232\text{-}234}$U, $^{238\text{-}240}$U and $^{236\text{-}242}$Pu isotopes. The theoretical results for *g*-factors show a decrease at a certain spin in ^{230,232}U isotopes, thereafter the theoretical *g*-factors show an increasing trend. In case of $^{234\text{-}240}$U the *g*-factor shows a reverse trend. The experimental *g*-factors for ^{238}U has been found to be in good agreement with the theoretical values qualitatively. The theoretical results of *g*-factors of $^{236\text{-}242}$Pu isotopes predict an increase in *g*-factors at higher spins. The present calculation predicts an increase in g-factors at higher spins in U and Pu isotopes due to alignment of protons in $1i_{13/2}$ orbit.

Chapter 3 presents the microscopic study of some even-even and odd-*A* Curium isotopes. The yrast bands, *B(E2)* transition probabilities and *g*-factors have been calculated and compared with the available experimental data. The structure of the yrast bands has been investigated from the band diagrams. The calculated $B(E2; 2_1^+ \longrightarrow 0_1^+)$ values are in good agreement with experimental data for $^{244\text{-}248}$Cm isotopes. In case of ^{248}Cm, the experimental data is available up to spin 24^+ which is reproduced by the present calculation. The *g*-factors are also calculated for $^{242\text{-}248}$Cm isotopes which shows an increasing trend with spin. The experimental level energies of ground state bands of $^{243\text{-}247}$Cm and lowest excited state bands in ^{243,245}Cm have been reproduced qualitatively by the present calculation. The transition energies of ground state bands of odd $^{243\text{-}247}$Cm have been also reproduced qualitatively by the present calculation.

Lastly, **Chapter 4** summarizes the overall work of the thesis.

Chapter 2

Projected Shell Model study of even-even Uranium and Plutonium nuclei

2.1 Introduction

In the past few years, researchers have made significant progress in synthesis of new elements [74-77]. Presently, little is known about their structure. The heaviest nuclei for which the detailed spectroscopy measurements can be performed lie in the actinide region [78-80]. These nuclei are not super heavy elements but at the gateway of super heavy element region. These nuclei are well deformed and their study may provide an indirect way to access the single particle states of the closed spherical shells, which are of direct relevance to the location of the predicted island. In the actinide region the energy spectra of many nuclei have been measured now with high precision up to higher spins (~30^+). The moments of inertia of the actinide nuclei are nearly twice than those of the rare-earth nuclei. Because of this, the two quasi-particle s-band does not compete with ground state band up to high spin [81]. The yrast levels with even spin and parity in the actinide nuclei usually belong to the ground state bands up to higher spins. The available experimental data on the positive parity rotational bands of these nuclei, therefore, provides an ideal opportunity to test the applicability of various models.

Ower *et al.* [35] have studied the multiple coulomb excitation of ^{234,236}U by 5.3 MeV/u ^{208}Pb ions by using gamma ray spectroscopy and observed the excitation of ground-band levels of ^{234,236}U up to spins I=26^+ and 28^+, respectively. Transition energies between ground-band levels of these nuclei have also been studied by them, suggesting that at spin (I) ≈ 28^+ several units of angular momentum are carried by single particles aligned with the rotational axis. They have discussed their experimental results by using the concept of rotational alignment and compared them with predictions of the rotation-vibration and Interacting boson model. Ward *et al.* [36] performed the gamma ray spectroscopy of states populated in multiple coulomb excitation and obtained the ground state band of ^{238}U up to spin 30^+. They compared their experimental data with cranked

random phase approximation calculations. These calculations described well the low spin properties of the positive parity bands but the high spin states could not be explained satisfactorily. Ishii *et al.* [39] have measured the de-excitation of gamma rays of the heaviest neutron rich ^{240}U and obtained the level energy of the ground state band up to spin I=12^{+}. Hausser *et al.* [40] measured the g-factors of the high spin yrast states in ^{238}U and found the first evidence for the onset of proton alignment of $i_{13/2}$ protons at spin I=(18-24). Nadirbekov *et al*. [82] have studied excited collective states of even–even nuclei by employing quadrupole and octupole deformations within a nonadiabatic collective model. They have demonstrated the importance of asymmetric degrees of freedom of the quadrupole–octupole motion of the system, which determine not only low-lying levels in the yrast band but also higher lying levels in the first and second nonyrast bands. Nadirbekov *et al*. [83] have described the structure of the lowest positive and negative-parity levels in the spectra of heavy even–even nuclei. They have reproduced the overall structure of the lowest alternating-parity energy sequences in several actinide nuclei. Govor *et al*. [84] have investigated the structure of excited levels and gamma transitions in ^{238}U by using gamma radiation associated with the respective (n, n′γ) reaction and with fission fragments. They have proposed level scheme and gamma transitions in ^{238}U. They have also proposed new levels (including those of spin–parity J^{π} = 0^{+}) at excitation energies below 2 MeV. Levon *et al.* [85] have studied excitation spectra of ^{232}U by means of the (p, t) transfer reaction. They have found 13 excited 0^{+} states in ^{232}U up to energy of 3.2 MeV. They have also derived moments of inertia and found that most of the values of moments of inertia are not much higher than the value of ground state band. Shneidman *et al*. [86] have suggested the cluster interpretation of the properties of multiple negative parity bands and positive parity rotational bands in ^{240}Pu. They have also explained the observed excitation spectrum and the angular momentum dependences of the parity splitting and of the electric E1 and E2 transition moments. Diebel and Mosel [87] have performed cranked Hartree-Fock-Bogoliubov (HFB) calculations of the yrast line for the nuclei $^{234\text{-}238}$U. Their HFB calculations could not explain the observed proton alignment in these nuclei. Ploszajczale and Faessler [71] have studied the rotational properties of actinide nuclei in the cranked HFB model with pairing and quadrupole interaction and found that the $i_{13/2}$ protons are

mainly responsible for causing the gradual increase of moment of inertia in ^{236}U. Egido and Ring [66] have performed microscopic study of the yrast line in the well deformed actinide nuclei. They have discussed several versions of the cranking model and found that the mean-field approach, in the form of cranking model in the simplified version of the rotating shell model is able to reproduce the alignment and band crossing pattern at the yrast line. Chiang et al [67] have calculated the energy spectra and *B(E2)* values of $^{232\text{-}238}$U in the interacting boson plus fermion model and found that in order to reproduce the identical energy bands, weak boson pairing, a weak angular momentum interaction and a strong quadrupole interaction are needed in these nuclei.

In order to investigate the properties of U and Pu nuclei, projected shell model (PSM) is employed as a theoretical tool in the present work. I was prompted to use this model of calculation as it produces satisfactory results in rare earth mass region [88-97]. For example, Bian *et al.* [89] have studied the systematics of *g*-factors of the first 2^+ states in even-even nuclei from Gd to Pt by using the same approach. Their calculations reproduced the energy bands and *B(E2)*s for low-lying states for all the nuclei. Besides, the down-sloping trend of $g(2_1^+)$ factor in the Gd, Dy and Er isotopes, the up-sloping trend in W isotopes and the flat behaviour of Yb and Hf isotopes have been very well reproduced in their calculations. Sometime back, the PSM was used by Wei *et al.* [90] to investigate the ground bands and β-bands of ^{230,232}Th and ^{232,234}U. The energy schemes and E2 transition rates calculated by them agree well with the experimental data. In the present work, the positive parity yrast bands of isotopic mass chains of U and Pu are investigated by employing quadrupole-quadrupole plus monopole and quadrupole-pairing force in the Hamiltonian within the framework of Projected Shell Model approach. The results have been obtained for yrast levels, BCS subshell occupation numbers, *B(E2)* transition probabilities and *g*-factors.

2.2 Calculational Details

In this section an attempt is made to present briefly the formal aspects of Projected Shell Model (PSM) [88]. The Hamiltonian used in the present work is specified and for this, the HFB procedure leads essentially to the Nilsson + BCS scheme.

Obviously, this is the main reason why the present model can describe various types of nuclei over a wide range of isotope or isotone chains quite accurately.

To understand the major features of PSM, it is important to introduce certain elementary concepts of projection operators and their properties. Accordingly, the general discussion of the model is presented under the following sub headings:

2.2.1 Projection operator

The projection operator associated with a compact Lie Group is a well-known concept in the theory of group representations [98]. To begin with, an attempt is made to summarize the important properties of the projection operator. In the present context, one is primarily interested in the Rotation or SU(2) Group whose elements are specified by the group parameter Ω, which represents a set of Euler angles (α, γ = [0, 2π] and β = [0, π]). The explicit form of the group element is

$$\hat{R}(\Omega) = e^{-i\alpha\hat{J}_x} e^{-i\beta\hat{J}_y} e^{-i\gamma\hat{J}_z}, \tag{2.1}$$

where, $\hat{J}$s are the angular momentum operators. Its (unitary) representation is

$$\left\langle \mu IM \middle| \hat{R}(\Omega) \middle| \nu JK \right\rangle = \delta_{\mu\nu}\delta_{IJ} D^{I*}_{MK}(\Omega), \tag{2.2}$$

where the symbol * means the complex conjugation and $D^{I}_{MK}(\Omega)$ is the *D*-function [99]. The *D*-functions form a complete set of functions in the parameter space of Ω. For a state $|\mu IM\rangle$ belonging to the angular momentum IM, μ designates a set of quantum numbers that specify the quantum state uniquely, so that the following closure holds:

$$\sum_{\mu IM} |\mu IM\rangle\langle\mu IM| = 1. \tag{2.3}$$

One needs not to specify details of the state $|\mu IM\rangle$, except for the fact that it belongs to a complete set of orthonormal vectors in a Hilbert space in which the operator (2.1) acts. From eqs. (2.2) and (2.3), it follows that

$$\hat{R}(\Omega)\,|\,\nu I K\rangle = \sum_{M} |\,\nu I M\rangle D^{I*}_{MK}(\Omega), \tag{2.4}$$

which is the multiplet relation between the states belonging to a representation (angular momentum) I. Using equation (2.4) and the orthogonality of the *D*-functions

$$\int d\Omega D^{I*}_{MK}(\Omega) D^{I'}_{M'K'}(\Omega) = \frac{8\pi^2}{2I+1}\delta_{II'}\delta_{MM'}\delta_{KK'} \tag{2.5}$$

one obtains the relation

$$\hat{P}^{I}_{MK}\,|\,\nu I' K'\rangle = \delta_{II'}\delta_{KK'}\,|\,\nu I M\rangle, \tag{2.6}$$

where the operator $\hat{P}^{I}_{MK}$ is defined by

$$\hat{P}^{I}_{MK} = \frac{2I+1}{8\pi^2}\int d\Omega D^{I}_{MK}(\Omega)\hat{R}(\Omega) \tag{2.7}$$

and is called angular momentum projection operator. From eqs. (2.3) and (2.6), one obtains its spectral representation and the "sum rule"

$$\hat{P}^{I}_{MK} = \sum_{\nu} |\,\nu I M\rangle\langle \nu I K\,|, \;\; \sum_{IM}\hat{P}^{I}_{MM} = 1. \tag{2.8}$$

Using the spectral representation, one can easily derive the properties

$$\hat{P}^{I\dagger}_{MK} = \hat{P}^{I}_{KM} \qquad and \qquad \hat{P}^{I}_{KM}\hat{P}^{I'}_{M'K'} = \delta_{II'}\delta_{MM'}\hat{P}^{I}_{KK'} \tag{2.9}$$

In general, a set of projection operators must satisfy the relations $P_i^{\dagger} = P_i,\;\; P_i P_j = \delta_{ij} P_i,$ $\sum_i P_i = 1,$ so that $\hat{P}^{I}_{MK}$ is a projection operator in the usual sense only if $K \equiv M.$

In an analogous way, the particle number projection operator is introduced in terms of a gauge group [element= $\exp(-i\phi\hat{N})$ and representation = $\exp(i\phi N)$] by

$$\hat{P}^{\mathrm{N}} = \frac{1}{2\pi}\int_{0}^{2\pi} d\phi e^{-i\phi(\hat{\mathrm{N}}-\mathrm{N})}, \tag{2.10}$$

where $\hat{\mathrm{N}}$ is the particle number operator. The group parameter ϕ is called the gauge angle. The operator $\hat{P}^{\mathrm{N}}$ is a projection operator in the usual sense.

When projecting the angular momentum and particle number simultaneously, one can combine two projectors (2.7) and (2.10)

$$\hat{P}^{I\mathrm{N}}_{MK} \equiv \hat{P}^{I}_{M\mathrm{K}}\hat{P}^{\mathrm{N}} = \frac{2I+1}{16\pi^3}\int d\Omega d\phi D^{\mathrm{I}}_{M\mathrm{K}}(\Omega)\hat{R}(\Omega)e^{-i\phi(\hat{\mathrm{N}}-\mathrm{N})}. \qquad (2.11)$$

It should be noted that $\hat{P}^{I}_{M\mathrm{K}}$ and $\hat{P}^{\mathrm{N}}$ commute with each other. What is shown above is only a formal definition. It is therefore, supplemented with a discussion which demonstrates how such an operator comes into play in a physical problem taking the angular momentum projection operator as an example.

2.2.2 Shell model in projected basis

Suppose that $|\Phi\rangle$ is a "deformed" state, which means that it is not an eigen-state of the angular momentum. Because of the rotational invariance of the Hamiltonian

$$\hat{R}^{\dagger}(\Omega)\hat{H}\hat{R}(\Omega) = \hat{H}, \qquad (2.12)$$

the energy expectation value

$$\frac{\langle\Phi|\hat{H}|\Phi\rangle}{\langle\Phi|\Phi\rangle} \qquad (2.13)$$

remains the same even if one rotates the state $|\Phi\rangle$. In other words, all states $\hat{R}(\Omega)|\Phi\rangle$ having different orientation Ω are mutually degenerate. It is noted that $\hat{R}(\Omega)|\Phi\rangle$ can be linearly independent of $|\Phi\rangle$ since deformed states do not satisfy a linear relation such as eq. (2.4). A wider class of states can be constructed by forming a superposition

$$|\Psi\rangle = \int d\Omega F(\Omega)\hat{R}(\Omega)|\Phi\rangle, \qquad (2.14)$$

where $F(\Omega)$ is a function to be determined by minimizing the energy expectation value

$$\mathrm{E} = \frac{\langle \Psi \mid \hat{H} \mid \Psi \rangle}{\langle \Psi \mid \Psi \rangle} \tag{2.15}$$

This procedure should and does give an energy lower than that given by eq. (2.13) because the space spanned by $\hat{R}(\Omega)\mid \Phi\rangle$ is larger than that consisting of just a single state $\mid \Phi\rangle$ which corresponds to $\Omega = 0$. The variational procedure can be simplified greatly by making use of the completeness of the *D*-functions. The trial function $F(\Omega)$ can be expanded as

$$F(\Omega) = \sum_{IMK} \frac{2I+1}{8\pi^2} F^I_{MK} D^I_{MK}(\Omega) \tag{2.16}$$

Substituting eq. (2.16) into eq. (2.14) one gets,

$$\mid \Psi\rangle = \sum_{IMK} F^I_{MK} \hat{P}^I_{MK} \mid \Phi\rangle, \tag{2.17}$$

where, P^I_{MK} is the angular momentum projection operator defined by eq. (2.7). The coefficients F^I_{MK} now play the role of the variational parameters in place of the variational function $F(\Omega)$. If the variational procedure is carried out with eq. (2.17), the summation over I and M actually drops away (i.e., a sharp I and M) due to eqs. (2.9) and (2.12). Note, in particular, that (2.12) implies that the Hamiltonian commutes with the projection operator. Thus, it is sufficient to carry out the variational calculation with

$$\mid \Psi\rangle = \sum_{K} F^I_{K} \hat{P}^I_{MK} \mid \Phi\rangle \tag{2.18}$$

by omitting the summation over I and M. This means that $\mid \Psi\rangle$ becomes an eigenstate of the angular momentum. The rotational symmetry violated in the original state $\mid \Phi\rangle$ is thus recovered in the new state $\mid \Psi\rangle$. The resulting variational equation takes the form of an eigenvalue equation (and a normalization condition) independent of M:

$$\sum_{K'} \left\{ H^I_{KK'} - E N^I_{KK'} \right\} F^I_{K'} = 0, \quad \sum_{KK'} F^I_K N^I_{KK'} F^I_{K'} = 1, \tag{2.19}$$

where the Hamiltonian and norm matrix, are respectively defined by

$$H^I_{KK'} = \langle \Phi | \hat{H} \hat{P}^I_{KK'} | \Phi \rangle \text{ and } N^I_{KK'} = \langle \Phi | \hat{P}^I_{KK'} | \Phi \rangle \qquad (2.20)$$

If the state $|\Phi\rangle$ is triaxial, a given spin I appears, in general, more than once in the whole spectrum, $I = 0$ being a trivial exception. On the other hand, if it is axially symmetric for which the relation $\hat{J}_z |\Phi\rangle = K_0 |\Phi\rangle$ holds where K_0 is the conserved K-quantum number, the problem is simple. The solution of eq. (2.19) then becomes

$$E = \frac{H^I_{K_0 K_0}}{N^I_{K_0 K_0}} \text{ with } F^I_{K_0} = \frac{1}{\sqrt{N^I_{K_0 K_0}}} \qquad (2.21)$$

since only term with $K = K_0$ remains in the summation over K. This represents the most primitive form of the angular momentum projection theory. It does not allow admixture of excited bands and thus can describe one "rotational band" whose "rotational energy" is obtained by evaluating E as a function of spin I. In contrast to the triaxial case, a given spin I appears only once in the spectrum. It is noted that, for an axially symmetric case, the projection operator $\hat{P}^I_{MK}$ reduces effectively to

$$\left(I + \frac{1}{2} \right) \int_0^\pi d\beta \sin \beta d^I_{MK}(\beta) e^{-i\beta \hat{J}_y} \qquad (2.22)$$

since α and γ can be integrated explicitly when evaluating the matrix elements. The state $|\Phi\rangle$ used in the above argument can be generated, in practice, in various ways. One may construct such a symmetry violating state using the Nilsson (or Hartree-Fock) single-particle basis or, if the pairing correlations are strong, the Nilsson + BCS (or Hartree-Fock-Bogoluibov) quasiparticle basis. The state $|\Phi\rangle$ may violate various symmetries of the Hamiltonian because it represents an "intrinsic" state. It is seen from above that such a symmetry violating state is highly degenerate and a better state $|\Psi\rangle$ can be constructed by using this degeneracy. Moreover, it is shown that the violated symmetry is recovered in the new state. This implies that one can accept $|\Psi\rangle$ as a

possible approximate solution of the Hamiltonian. Here $|\Psi\rangle(|\Phi\rangle)$ is referred to as a state in the "space-fixed" ("body-fixed") system. This is the conventional terminology, whose origin can be traced back to the mathematical nature of the *D*-function appearing in the projection operator eq. (2.7). As is well-known there exist two sets of (mutually commuting) differential operators both representing the angular momentum, which are called, respectively, the space-fixed and body-fixed type, the latter being characterized by "wrong" signs in the angular momentum commutation relations. The quantum number M (K) of $D^I_{MK}(\Omega)$ originates from the former (latter). It is natural to associate M and K of the operators $\hat{P}^I_{MK}$ with the same physical interpretation as those of $D^I_{MK}(\Omega)$ and, as eq. (2.18) shows, the quantum number M belongs to $|\Psi\rangle$ and K to $|\Phi\rangle$. One refers to the former (latter) as the "space-fixed" ("body-fixed") state in this sense. Thus, the projection operator transforms a "body-fixed" state into a "space-fixed" state. The contents of the projection theory are rather abstract. However, it is possible to use many concepts developed in the semiclassical theory, such as the rotor model, [1] also in the projection theory as one translates them using an analogy. For example, it should be clear from the structure of the wave functions that the rotational motion of the "body" as a whole is described phenomenologically by the *D*-function D^I_{MK} in the former and microscopically by the projection operator $\hat{P}^I_{MK}$ in the latter.

2.2.3 Semi classical limit

In the previous subsection, a simple example of projecting just one "configuration" $|\Phi\rangle$ onto a good angular momentum is given. In the early days of the theory, the formula (2.21) represented, in fact, the whole contents of the angular momentum projection method [100]. A pioneering calculation [101, 102] was carried out using the Nilsson + BCS quasiparticle vacuum state $|0\rangle$ for $|\Phi\rangle$ (with $K_0 = 0$) which represents the ground state band or g-band of a doubly-even nucleus. The outcome of the theory is as follows:

After the α- and $\gamma-$ integration, the matrix element $\left\langle 0 \left| \hat{O} \hat{P}^I_{00} \right| 0 \right\rangle \left(\hat{O} = 1, \hat{H} \right)$ becomes

$$(2I+1)\int_0^{\frac{\pi}{2}} d\beta \sin\beta P_I(\cos\beta) \left\langle 0 \left| \hat{O} e^{-i\beta \hat{J}_y} \right| 0 \right\rangle \text{ for } I = \text{even} \qquad (2.23)$$

and 0 for $I =$ odd. Here, $d^I_{00}(\beta) = (-)^I d^I_{00}(\pi - \beta) = P_I(\cos\beta)$ is used and the symmetry of the integrand with respect to $\beta = \frac{\pi}{2}$ due to $e^{-i\pi \hat{J}_y} |0\rangle = e^{-i\pi \hat{J}_z} |0\rangle = |0\rangle$ has been used.

The above integral is estimated in the large deformation limit, which is referred to as the "semiclassical" limit. Since the fluctuation of the angular momentum is a good measure for the deformation, the result may be written as a power series in $1/\Delta J_y^2$.

First, the overlap of $\left\langle 0 \left| e^{-i\beta \hat{J}_y} \right| 0 \right\rangle$, is examined which may be written in the form

$$\left\langle 0 \left| e^{-i\beta \hat{J}_y} \right| 0 \right\rangle = exp\left\{ -i\int_0^{\beta} d\beta' \left\langle 0 \left| \hat{J}_y[\beta'] \right| 0 \right\rangle \right\}, , [\beta] \equiv \frac{e^{-i\beta \hat{J}_y}}{\left\langle 0 \left| e^{-i\beta \hat{J}_y} \right| 0 \right\rangle}, \quad (2.24)$$

as can be verified by differentiating both sides with respect to β. The left-hand side of eq. (2.24) corresponds to the characteristic function and the exponent of the right-hand side to the cumulant function known in statistical physics. The required expansion in terms of moments is given by what is known as the cumulant expansion, which is a power series expansion of the cumulant function. In the present case, it is obtained easily from the power series expansion of the operator [β] for small β ,

$$[\beta] = 1 - i\beta\left(\hat{J}_y - J_y\right) - \frac{1}{2}\beta^2\left(\hat{J}_y^2 - \Delta J_y^2\right) + \ldots \qquad (2.25)$$

The first order moment $J_y = \left\langle 0 \left| \hat{J}_y \right| 0 \right\rangle$ is zero due to the time reversal symmetry of $|0\rangle$ (generally, all odd moments vanish). It is better to stop at the second order moment

$\Delta J_y^2 = \left\langle 0 \middle| \left(\hat{J}_y - J_y\right)^2 \middle| 0 \right\rangle = \left\langle 0 \middle| \hat{J}_y^2 \middle| 0 \right\rangle$, which represents the fluctuation of the angular momentum. The following approximate relations are thus obtained:

$$\begin{cases} \langle 0 | e^{-i\beta \hat{J}_y} | 0 \rangle \approx e^{-\frac{1}{2}\Delta J_y^2 \beta^2} \\ \left[\beta\right] \approx 1 - i\beta \hat{J}_y - \frac{1}{2}\beta^2 : \hat{J}_y^2 : \end{cases} \tag{2.26}$$

where $: \hat{J}_y^2 : \equiv \hat{J}_y^2 - \Delta J_y^2$. The overlap is strongly peaked at $\beta = 0$ if ΔJ_y^2 is large. The integral in eq. (2.23) can be obtained in a closed form by using the approximation given by eq. (2.26) as well as an asymptotic form $P_I(\cos\beta) \approx J_0\left(\sqrt{I(I+1)}\beta\right)$ valid for small β, where $J_0(x)$ is the Bessel function of order zero, and by extending the integration range to infinity

$$\int_0^\infty d\beta \beta J_0\left(\sqrt{I(I+1)}\beta\right) e^{-\frac{1}{2}\Delta J_y^2 \beta^2} \left\{ \left\langle 0 \mid \hat{O} \mid 0 \right\rangle - \frac{1}{2} \left\langle 0 \mid \hat{O} \hat{J}_y^2 : \mid 0 \right\rangle \beta^2 \right\} \tag{2.27}$$

Also one has,

$$\int_0^\infty dx x^{2n+1} J_0(bx) exp\left\{ -\frac{1}{2} a^2 x^2 \right\} = \frac{2^n n!}{a^{2n+2}} L_n\left(\frac{b^2}{2a^2} \right) exp\left\{ -\frac{b^2}{2a^2} \right\}, \tag{2.28}$$

where, $L_n(x)$ is the Laguerre Polynomial of the order *n*. The energy $E_I = H_{00}^I / N_{00}^I$ and the norm N_{00}^I (for $I =$ even only) are obtained approximately as

$$E_I \approx E_0 + \frac{I(I+1)}{2\Im} \text{ and } N_{00}^I \approx Q_I \equiv \frac{2I+1}{\Delta J_y^2} exp\left\{ -\frac{I(I+1)}{2\Delta J_y^2} \right\}, \tag{2.29}$$

respectively, where the above quantities are defined as

$$\Im = \frac{\left(\Delta J_y^2\right)^2}{\left\langle 0 \mid \hat{H} : \hat{J}_y^2 : \mid 0 \right\rangle} \text{ and } E_0 = \frac{H_{00}^0}{N_{00}^0} \approx \left\langle 0 \mid \hat{H} \mid 0 \right\rangle - \frac{\Delta J_y^2}{\Im}. \tag{2.30}$$

Note that $\Im$ is nothing other than the Peierls-Yoccoz moment of inertia and also that the projected ground state energy E_0 is lower that the unprojected one, $\langle 0 | \hat{H} | 0 \rangle$, by an amount $\Delta J_y^2 / \Im$. This energy gain is due to the fluctuation of the angular momentum, which causes a "zero-point rotation". In fact, since $\Delta J_x^2 = \Delta J_y^2$, it may be written as $\frac{1}{2\Im}\left(\Delta J_x^2 + \Delta J_y^2\right)$, which represents the fluctuation of the rotational energy.

The norm N_{00}^I represents the probability distribution of the angular momentum in the ground state $|0\rangle$ as can be seen by using the spectral representation of eq. (2.8), $N_{00}^I = \langle 0 | \hat{P}_{00}^I | 0 \rangle = \sum_\nu \left| \langle 0 | \nu I 0 \rangle \right|^2$. Its approximation Q_I is normalized to 1 under the replacement $\sum_{I=even} \to \int_0^\infty \frac{dI}{2}$. The metric $\frac{1}{2}$ corresponds to the summation only over $I = even$. It is pointed out that the formulas depend only on two quantities, $E_I - E_0$ on $\Im$ and N_{00}^I on ΔJ_y^2, namely eq. (2.29) is the same for any Hamiltonian, which yields the same $\Im$ and ΔJ_y^2. It means that the result does not depend on details of the Hamiltonian.

2.2.4 Projected Shell Model (PSM)

Here, an attempt is made to formulate the PSM by generalizing the single-band theory discussed above and derive its basic equations. If one selects a set of multi-quasiparticle (multi-qp) states $\{|\Phi_\kappa\rangle\}$ which one wants to take into account in the shell model configuration space by projecting them onto good angular momentum I and particle number N, whose concrete specification will be given later for doubly-even, doubly-odd, and odd-mass nuclei.

Once the quasiparticle basis is prepared, the Hamiltonian is diagonalized in the shell model space spanned by $\left\{\hat{P}_{MK}^{IN} | \Phi_\kappa \rangle\right\}$. This leads to the eigenvalue equation

$$\sum_{\kappa' K'} \left\{ H^I_{\kappa K \kappa' K'} - E N^I_{\kappa K \kappa' K'} \right\} F^I_{\kappa' K'} = 0, \qquad (2.31)$$

with the normalization condition

$$\sum_{\kappa K \kappa' K'} F^I_{\kappa K} N^I_{\kappa K \kappa' K'} F^I_{\kappa' K'} = 1. \qquad (2.32)$$

Note that the eqs. (2.31) and (2.32) are the straightforward generalization of eq. (2.19) to a multi configuration space. The Hamiltonian and norm elements are defined, respectively, by

$$H^I_{\kappa K \kappa' K'} = \left\langle \Phi_\kappa \middle| \hat{H} \hat{P}^{IN}_{KK'} \middle| \Phi_{\kappa'} \right\rangle \text{ and } N^I_{\kappa K \kappa' K'} = \left\langle \Phi_\kappa \middle| \hat{P}^{IN}_{KK'} \middle| \Phi_{\kappa'} \right\rangle, \qquad (2.33)$$

which is the generalization of eq. (2.20)

The normalized eigenstate is given by

$$\left| \Psi_{IM} \right\rangle = \sum_{\kappa K} F^I_{\kappa K} \hat{P}^{IN}_{MK} \left| \Phi_\kappa \right\rangle, \qquad (2.34)$$

which is the generalization of eq. (2.18). It is noted that $\left|\Phi_\kappa\right\rangle$ and its time reversal $\left|\Phi_{\bar{\kappa}}\right\rangle$ yield the same projected state. This reduces the dimension of the configuration space by a factor of $1/2$.

To compute the matrix element of a tensor operator of rank λ with respect to the projected states, the matrix element of the operator $\hat{P}^{I'N'}_{K'M'} \hat{T}_{\lambda\mu} \hat{P}^{IN}_{MK}$ has to be evaluated. This is obtained as follows. On the one hand, one has the relation

$$\hat{P}^{I'}_{K'M'} \hat{T}_{\lambda\mu} \hat{P}^{I}_{MK} = (IM, \lambda\mu \mid I'M') \sum_{\nu} (IK'-\nu, \lambda\nu \mid I'K') \hat{T}_{\lambda\nu} \hat{P}^{I}_{K'-\nu K}, \qquad (2.35)$$

which follows from the transformation property of a tensor operator of rank λ under the rotation as well as the reduction theorem of a product of two *D*-functions. On the other hand, one has

$$\hat{P}^{N'} \hat{T}_{\lambda\mu} \hat{P}^{N} = \delta_{N'N+\Delta N} \hat{T}_{\lambda\mu} \hat{P}^{N} \text{ with } [\hat{N}, \hat{T}_{\lambda\mu}] = \Delta N \hat{T}_{\lambda\mu} \qquad (2.36)$$

Here, ΔN is an integer, which represents the difference between the number of single-particle creation and annihilation operators that constitute the operator $\hat{T}_{\lambda\mu}$. Namely, it is given by $\Delta N = 0(\pm 2)$ for the electromagnetic (pairing type) multipole operator. Combining the above two results, one obtains the relation $\left(\hat{P}^{IN}_{MK} \equiv \hat{P}^{I}_{MK}\hat{P}^{N}\right)$

$$\hat{P}^{I'N'}_{K'M'}\hat{T}_{\lambda\mu}\hat{P}^{IN}_{MK} = \delta_{N'N+\Delta N}\left(IM,\lambda\mu|I'M'\right)\sum_{\nu}\left(IK-\nu,\lambda\nu|I'K'\right)\hat{T}_{\lambda\nu}\hat{P}^{IN}_{K-\nu K}, \qquad (2.37)$$

So far, the mathematical framework of the projected shell model is given in full generality. It is formulated in quite a general manner allowing for triaxiality of the quasiparticle basis and taking into account the simultaneous angular momentum and particle number projection. In practice, some simplifications can be made, for example, by omitting the particle number projection. Although the particle number projection may improve the result, the essential physics of the yrast spectroscopy can be described even without taking it into consideration. Therefore, most of the present calculations have been done by replacing $\hat{P}^{IN}_{MK}$ with $\hat{P}^{I}_{MK}\left(\hat{P}^{N} \to 1\right)$.

The presence of axial symmetry and/or the omission of the particle number projection will simplify the equations and their numerical treatment. In particular, axial symmetry implies that the set of quantum numbers κ contains, amongst other things, the total intrinsic magnetic quantum number K implicitly. One can, therefore, omit writing K in the amplitude $F^{I}_{\kappa K}$ for such a system. Moreover, the summations over K may also be omitted since only one specific K contributes to the sum for a given κ. This leads to the set of equations on which (most of) the present numerical calculations are based:

$$\sum_{\kappa'}\left\{H^{I}_{\kappa\kappa'} - EN^{I}_{\kappa\kappa'}\right\}F^{I}_{\kappa'} = 0, \qquad \sum_{\kappa\kappa'}F^{I}_{\kappa}N^{I}_{\kappa\kappa'}F^{I}_{\kappa'} = 1,$$

$$H^{I}_{\kappa\kappa'} = \left\langle \Phi_{\kappa}\middle|\hat{H}\hat{P}^{I}_{KK'}\middle|\Phi_{\kappa'}\right\rangle, \qquad N^{I}_{\kappa\kappa'} = \left\langle \Phi_{\kappa}\middle|\hat{P}^{I}_{KK'}\middle|\Phi_{\kappa'}\right\rangle. \qquad (2.38)$$

Then, the matrix element of a tensor operator of rank λ can be evaluated by

$$\left\langle \Psi_{I'M'} \middle| \hat{T}_{\lambda\mu} \middle| \Psi_{IM} \right\rangle = (IM, \lambda\mu | I'M') \left\langle \Psi_{I'} \middle\| \hat{T}_{\lambda} \middle\| \Psi_{I} \right\rangle,$$

$$\left\langle \Psi_{I'} \middle\| \hat{T}_{\lambda} \middle\| \Psi_{I} \right\rangle = \sum_{\nu\kappa\kappa'} (IK'-\nu, \lambda\nu | I'K') \left\langle \Phi_{\kappa'} \middle| \hat{T}_{\lambda\mu} \hat{P}^{I}_{K'-\nu K} \middle| \Phi_{\kappa} \right\rangle F^{I'}_{\kappa'} F^{I}_{\kappa}, \qquad (2.39)$$

which follows from the operator identity (2.35) and is, therefore, also valid for the triaxial case with an obvious extension of the formula for the triaxial basis.

2.2.5 Choice of the Hamiltonian

The Hamiltonian which has been used throughout the present work, is described as follows. The interaction consists of a sum of schematic (i.e. $Q.Q+$ Monopole Pairing $+$ Quadrupole pairing) forces which represent different kinds of characteristic correlations between active nucleons. The total Hamiltonian of the present model assumes the form

$$\hat{H} = \hat{H}_0 - \frac{\chi}{2} \sum_{\mu} \hat{Q}^{\dagger}_{\mu} \hat{Q}_{\mu} - G_{\mathrm{M}} \hat{P}^{\dagger} \hat{P} - G_{Q} \sum_{\mu} \hat{P}^{\dagger}_{\mu} \hat{P}_{\mu}. \qquad (2.40)$$

The first term represents the harmonic oscillator single-particle Hamiltonian

$$\hat{H}_0 = \sum_{\alpha} c^{\dagger}_{\alpha} \varepsilon_{\alpha} c_{\alpha} \left(\varepsilon_{\alpha} \equiv \hbar\omega \left\{ N - \kappa \left[2 j.s + \mu \left(l^2 - \left\langle l^2 \right\rangle \right) \right]_{N_j} \right\} \right), \qquad (2.41)$$

where $c^{\dagger}_{\alpha}$ and c_{α} are, respectively, the single-particle creation and annihilation operator labeled by a set of the spherical harmonic oscillator quantum numbers $\alpha = \{N, j, m\}$. Note that l is known when N and j are specified. The Fermi energy will be included in the single-particle energy $(\varepsilon_{\alpha} \to \varepsilon_{\alpha} - \lambda)$ for convenience and obvious dependence on the isospin degrees of freedom will be omitted for simplicity. Here in the present work, three major shells N = 4, 5, 6 (5, 6, 7) for protons (neutrons) for the valence single-particle space, have been taken. The Nilsson parameters used in the present calculation are taken from Ref. [103]. The multiparticle configurations are constructed from the Nilsson SP

states near the Fermi levels. The one-body operators in eq. (2.40) are defined (for each kind of nucleons) by

$$\hat{Q}_\mu = \sum_{\alpha\beta} c_\alpha^\dagger Q_{\mu\alpha\beta} c_\beta, \qquad \hat{P}^\dagger = \frac{1}{2}\sum_\alpha c_\alpha^\dagger c_{\bar{\alpha}}^\dagger, \qquad \hat{P}_\mu^\dagger = \frac{1}{2}\sum_{\alpha\beta} c_\alpha^\dagger Q_{\mu\alpha\beta} c_{\bar{\beta}}^\dagger, \quad (2.42)$$

where $\bar{\alpha}$ represents the time reversal of $\alpha\left(c_{\bar{\alpha}} = \hat{T} c_\alpha \hat{T}^\dagger = (-)^{j-m} c_{N_{j-m}}\right)$ while

$$Q_{\mu\alpha\alpha'} = \delta_{NN'} \left\langle Njm \middle| Q_\mu \middle| N' j' m' \right\rangle \quad (2.43)$$

is the matrix element of the SU(3) quadrupole generator, whose matrix elements are equal to those of the dimensionless mass quadrupole operator

$$\sqrt{\frac{4\pi}{5}} \left(\frac{r}{b}\right)^2 Y_{2\mu}$$

for $N = N'$, but vanish for $N \neq N'$ where b is the harmonic oscillator length

$$b^2 = \frac{\hbar}{m\omega}$$

Note the symmetry properties of the matrix element

$$Q_{\bar{\mu}\alpha\beta} \equiv Q_{\mu\bar{\alpha}\bar{\beta}} = Q_{\mu\beta\alpha} = (-)^\mu Q_{-\mu\alpha\beta} \quad (2.44)$$

which ensure the relations $\hat{Q}_{\bar{\mu}} = \hat{T}\hat{Q}_\mu\hat{T}^\dagger = \hat{Q}_\mu^\dagger = (-)^\mu \hat{Q}_{-\mu}$.

The HFB single-particle Hamiltonian resulting from eq. (2.40) is

$$\hat{H}_{HFB} = \hat{H}_0 - \chi \sum_\mu \left\langle \hat{Q}_\mu \right\rangle \hat{Q}_\mu - G_M \left\langle \hat{P} \right\rangle \left(\hat{P} + \hat{P}^\dagger\right) - G_Q \sum_\mu \left\langle \hat{P}_\mu \right\rangle \left(\hat{P}_\mu + \hat{P}_\mu^\dagger\right). \quad (2.45)$$

Here, $\langle \ldots \rangle$ means the expectation value with respect to the HFB vacuum state $|0\rangle$. Note that $\left\langle \hat{Q}_\mu \right\rangle$ vanishes for $\mu = odd$ while $\left\langle \hat{Q}_\mu \right\rangle = \left\langle \hat{Q}_{\bar{\mu}} \right\rangle$ if $\mu = even$, due to the time reversal

symmetry. For axially symmetric nuclei, all vanish except for $\mu = 0$. The same applies to $\left\langle \hat{P}_\mu \right\rangle$.

Before going into the isospin dependence of the above forces, nuclear size is adjusted by using the conventional harmonic oscillator parameters.

$$\omega_\tau = \omega_0 a_\tau, \qquad b_\tau^2 = \frac{b_0^2}{a_\tau}, \qquad b_0^2 = \frac{\hbar}{m\omega_0}, \qquad a_\tau \equiv \left\{1 \pm \frac{N-Z}{A}\right\}^{\frac{1}{3}}, \tag{2.46}$$

with + (–) for τ = neutron(proton). If one uses the value $\hbar\omega_0 = 41.4678 A^{-\frac{1}{3}} MeV$, for example, one finds $b_0^2 = A^{\frac{1}{3}} fm^2$ which is not only easy to remember but also practical. The monopole pairing force constants G_M are adjusted to give the known energy gaps.

The monopole-pairing strength is taken to be

$$G_M = \left[G_1 \mp G_2 \frac{N-Z}{A}\right] A^{-1} \tag{2.47}$$

with '-' for neutrons and '+' for protons. Here, G_1 and G_2 are taken as 20.12 and 13.13 MeV, respectively. These strengths are taken from [96]. The strength of quadrupole-quadrupole pairing force G_Q is proportional to G_M. In the present calculation, the ratio of G_Q/G_M is fixed as 0.240 for ^{230,232}U, 0.220 for ^{234}U, 0.200 for ^{236}U, 0.160 for ^{238,240}U and 0.160 for $^{236\text{-}242}$Pu.

For $Q.Q$ force, the second term of (2.45) can be identified as the (stretched) Nilsson potential $\frac{2}{3}\varepsilon\hbar\omega\hat{Q}_0$. Introducing $x_\tau \equiv \hbar\omega_\tau \left\langle \hat{Q}_0 \right\rangle_\tau$ and $C_{\tau\tau'} \equiv \chi_{\tau\tau'} (\hbar\omega_\tau \hbar\omega_{\tau'})^{-1}$, one obtains the self consistent condition

$$\begin{aligned} C_{nn} x_n(\varepsilon_n, \varepsilon_p) + C_{np} x_p(\varepsilon_n, \varepsilon_p) &= \frac{2}{3}\varepsilon_n, \\ C_{pn} x_n(\varepsilon_n, \varepsilon_p) + C_{pp} x_p(\varepsilon_n, \varepsilon_p) &= \frac{2}{3}\varepsilon_p, \end{aligned} \tag{2.48}$$

whose solutions ε_n and ε_p are, in general, different from each other [104]. Here, it is assumed that the neutron and proton deformation parameters are equal to each other, $\varepsilon_n = \varepsilon_p = \varepsilon_2$. The necessary and sufficient condition for this is that two equations of (2.48) reduce to a single equation, namely, they have to be linearly dependent:

$$C_{nn}C_{pp} - C_{np}^2 = 0, \left(C_{pn} = C_{np}\right), \tag{2.49}$$

which is the condition for the determinant of eq. (2.48) to vanish, so that eqs. (2.48) and (2.49) lead to the isoscalar coupling $C_{nn} = C_{pp} = C_{np}$. Thus, the following relation is obtained

$$\chi_{\tau\tau'} = \frac{\frac{2}{3}\varepsilon_2 \hbar\omega_\tau \hbar\omega_{\tau'}}{\hbar\omega_n \left\langle \hat{Q}_0 \right\rangle_n + \hbar\omega_p \left\langle \hat{Q}_0 \right\rangle_p} \tag{2.50}$$

This is a very useful relation since the nuclear deformation is a well-studied quantity [105]. The $Q.Q$ force coupling constant corresponding to a given deformation parameter ε_2 is obtained by eq. (2.50). This strategy is adopted to ensure that the $Q.Q$ force generates the correct nuclear deformation. Note, however, that $\chi_{\tau\tau'}$ remains undetermined for $\varepsilon_2 = 0$ (a spherical nucleus) since both $\left\langle \hat{Q}_0 \right\rangle_n$ and $\left\langle \hat{Q}_0 \right\rangle_p$ vanish.

The present force model works surprisingly well despite its simplicity. Nevertheless, it has obvious shortcomings. In the first place, the nuclear deformation is restricted to the quadrupole type only. Secondly, the neutron-proton interaction is present only in the (particle-hole type) $Q.Q$ force. Depending on the problem, all this might be too restrictive and one will have to introduce (schematic) forces of a more general type.

The logical structure of the theory is summarized as follows:

The calculation proceeds in the following sequence. For each nucleon, first Nilsson Hamiltonian

$$\hat{H}_0 - \frac{2}{3}\varepsilon_2 \hbar\omega \hat{Q}_0 \qquad (2.51)$$

is diagonalized for the known deformation parameter ε_2 and the usual BCS procedure is carried to take the (static) Monopole Pairing force into account. This defines the Nilsson + BCS quasiparticle basis. In principle, one should use the HFB basis to take also the (static) Quadrupole Pairing force into account. In practice, however, this does not make much difference to the Nilsson + BCS basis after the final shell model diagonalization, so that the simpler procedure may be used to a good approximation. Now, the strengths of the *Q.Q* force can be evaluated by the relation (2.50). This fixes the Hamiltonian (2.40), which is then diagonalized within the shell model space spanned by a selected set of projected multi-*qp* states. The quasiparticle configurations are listed below for different types of nuclei.

Doubly-even nucleus: $|0\rangle, a^\dagger_{\nu 1} a^\dagger_{\nu 2}|0\rangle, a^\dagger_{\pi 1} a^\dagger_{\pi 2}|0\rangle, a^\dagger_{\nu 1} a^\dagger_{\nu 2} a^\dagger_{\pi 1} a^\dagger_{\pi 2}|0\rangle,$

Doubly-odd nucleus: $a^\dagger_\nu a^\dagger_\pi |0\rangle,$

Odd-neutron nucleus: $a^\dagger_\nu |0\rangle, a^\dagger_\nu a^\dagger_{\pi 1} a^\dagger_{\pi 2}|0\rangle,$

Odd-proton nucleus: $a^\dagger_\pi |0\rangle, a^\dagger_\pi a^\dagger_{\nu 1} a^\dagger_{\nu 2}|0\rangle,$

where, $\nu' s (\pi' s)$ denote the neutron(proton) Nilsson quantum numbers which run over properly selected (low-lying) quasi-particle states. Those configurations has been discarded that contain three or more like-nucleon quasi-particles because they have higher excitation energies due to mutual blocking of levels and thus affect the results little in the energy (and the spin) ranges of interest. This restriction can be easily released if necessary.

2.3 Results and discussion for even-even $^{230\text{-}240}$U and $^{236\text{-}242}$Pu isotopes

2.3.1 *Deformation systematics of $^{230\text{-}240}$U*

The quadrupole and hexadecapole deformation parameters used in the present calculations are listed in Table 2.1. The quadrupole deformation parameters (ε_2) used in the present calculation are near to the values suggested by Bengtsson [106]. In Table 2.2, the systematics of E_2^+, E_4^+/E_2^+ are presented for $^{230\text{-}240}$U isotopes. It is known that the ratio of energies of the first 4^+ and 2^+ states gives a good criterion for assessing the shape deformation of a nucleus [107]. The value of this ratio has the limiting value 2 for a quadrupole vibrator, 2.5 for a nonaxial gamma soft rotor and 3.33 for an ideal symmetric rotor. From Table 2.2, it is observed that the experimental E_4^+/E_2^+ ratio of all $^{230\text{-}240}$U isotopes is greater than 3.0. Consequently, these isotopes lie in the rotational limit**.** From the systematics of experimental E_2^+ energies, it is seen that its value for ^{230}U is 0.052 MeV and thereafter it shows a gradual decrease up to ^{234}U. The value of E_2^+ for ^{234}U is 0.044 MeV, thereafter the E_2^+ values show a slight increase and remains constant as one moves from $^{236\text{-}240}$U .The E_4^+/E_2^+ ratio shows a slight increase in their values as one moves from ^{230}U to ^{232}U, ^{234}U to ^{236}U and ^{238}U to ^{240}U due to an increase in the E_4^+ values. The calculated values of $E_2^+$and E_4^+/E_2^+ ratio of U isotopes follow nearly the same trend as exhibited by the experimental ones. For example, the experimental value of E_2^+ decreases from 0.052 MeV for ^{230}U to 0.044 MeV for ^{234}U whereas the theoretical value decreases from 0.051 MeV for ^{230}U to 0.043 MeV for ^{234}U.

In order to understand the deformation systematics in U isotopes, the BCS subshell occupation numbers are presented for protons and neutrons in Tables 2.3 and 2.4, respectively. The proton shells below $Z\cong 82$ i.e $3s_{1/2,}$ $2d_{3/2,}$ $2d_{5/2,}$ $1g_{7/2}$ *and* $1g_{9/2}$ orbits for protons and neutron shells below $N\cong 126$ i.e $3p_{1/2}$, $3p_{3/2}$, $2f_{5/2}$, $2f_{7/2}$, $1h_{9/2}$ and $1h_{11/2}$ orbits for neutrons are nearly full, thus the occupation numbers for these shells are not presented in Tables 2.3 and 2.4. From Table 2.3, it is seen that occupation probability of protons is spread over $3p_{1/2}$, $3p_{3/2}$, $2f_{5/2}$, $2f_{7/2}$, $1h_{9/2}$, $1h_{11/2}$, $2g_{9/2}$, $1i_{11/2}$ and $1i_{13/2}$ proton orbits. The occupation probability of $1h_{11/2}$ proton orbit decreases slowly as one moves from ^{230}U to ^{240}U. The decrease in the occupation of $(1h_{11/2})_\pi$ orbit can be responsible for

the observed trend of deformation as one moves from ^{230}U to ^{240}U. Besides this, the $1h_{9/2}$, $2f_{7/2}$, $2f_{5/2}$ and $3p_{1/2}$ proton orbits are also having sizable occupation probability. The $1i_{13/2}$ proton orbit has occupation number greater than 4.0. Thus, the occupation of $1i_{13/2}$ and $1h_{9/2}$, $2f_{7/2}$, $2f_{5/2}$, $3p_{1/2}$ proton orbits also contributes to the collectivity of $^{230\text{-}240}$U.

From Table 2.4, it is seen that the occupation of neutrons is spread over the $4s_{1/2}$, $3d_{3/2}$, $3d_{5/2}$, $2g_{7/2}$, $2g_{9/2,}$ $1i_{11/2}$, $1i_{13/2}$, $2h_{11/2}$ and $1j_{15/2}$ orbits. It is observed that the occupation probability of $2g_{7/2}$, $2g_{9/2}$, $1i_{11/2}$, $1i_{13/2}$ and $1j_{15/2}$ neutron orbits increases with neutron number, thereby bringing more and more collectivity for the U isotopes. Thus, the observed deformation trend of low-lying states in $^{230\text{-}240}$U isotopes could be linked with the occupation of down-sloping components of high *j* orbits in the valence space.

2.3.2 *Deformation systematics of $^{236\text{-}242}$Pu*

The quadrupole and hexadecapole deformation parameters used for the calculation of $^{236\text{-}242}$Pu are listed in Table 2.5. In Table 2.6, the systematics of E_2^+, E_4^+/E_2^+ are presented for $^{236\text{-}242}$Pu. From Table 2.6, it is observed that the experimental E_4^+/E_2^+ ratio of $^{236\text{-}242}$Pu isotopes is greater than 3.0. Consequently, these isotopes lie in the rotational limit**.** From the systematics of experimental E_2^+ energies, it is seen that its value for ^{236}Pu is 0.045 MeV and thereafter it shows a gradual decrease up to ^{240}Pu. The value of E_2^+ for ^{240}Pu is 0.043 MeV, thereafter the E_2^+ value shows a slight increase for ^{242}Pu. The experimental E_4^+/E_2^+ ratio shows a slight increase in their values as one moves from ^{236}Pu to ^{238}Pu and from ^{240}Pu to ^{242}Pu due to an increase in the E_4^+ values. The calculated values of $E_2^+$and E_4^+/E_2^+ ratio of Pu isotopes follow nearly the same trend as exhibited by the experimental ones. For example, the experimental value of E_2^+ decreases from 0.045 MeV for ^{236}Pu to 0.043 MeV for ^{240}Pu whereas the theoretical value decreases from 0.045 MeV for ^{236}Pu to 0.043 MeV for ^{240}Pu.

In order to understand the deformation systematics in Pu isotopes, the BCS subshell occupation numbers are presented for protons and neutrons in Tables 2.7 and 2.8, respectively. From Table 2.7, it is seen that occupation probability of protons is spread over $3p_{1/2}$, $3p_{3/2}$, $2f_{5/2}$, $2f_{7/2}$, $1h_{9/2}$, $1h_{11/2}$, $2g_{9/2}$, $1i_{11/2}$ and $1i_{13/2}$ proton orbits. The occupation probability of $1h_{11/2}$ proton orbit decreases slowly as one moves from ^{236}Pu to

^{242}Pu. The decrease in the occupation of $(1h_{11/2})_\pi$ orbit can be responsible for the observed trend of deformation as one moves from ^{236}Pu to ^{242}Pu. Besides this, the $1h_{9/2}$, $2f_{7/2}$, $2f_{5/2}$ and $3p_{1/2}$ proton orbits are also having sizable occupation probabilities. The $1i_{13/2}$ proton orbit has occupation number greater than 4.0. Thus, the occupation of $1i_{13/2}$ and $1h_{9/2}$, $2f_{7/2}$, $2f_{5/2}$, $3p_{1/2}$ proton orbits also contributes to the collectivity of $^{236\text{-}242}$Pu.

From Table 2.8, it is seen that the occupation of neutrons is spread over the $4s_{1/2}$, $3d_{3/2}$, $3d_{5/2}$, $2g_{7/2}$, $2g_{9/2}$, $1i_{11/2}$, $1i_{13/2}$, $2h_{11/2}$ and $1j_{15/2}$ orbits. It is observed that the occupation probability of $2g_{7/2}$, $2g_{9/2}$, $1i_{11/2}$ and $1j_{15/2}$ neutron orbits increases with neutron number, thereby bringing more and more collectivity for the Pu isotopes. Thus, the observed deformation trends of low-lying states in Pu isotopes could be linked with the occupation of down-sloping components of high *j* orbits in the valence space.

2.3.3 *Yrast Spectra of $^{230\text{-}240}$U*

In Fig. 2.1, a comparison of calculated and experimental yrast energies of $^{230\text{-}240}$U isotopes are presented. The experimental level scheme of positive parity yrast bands for $^{230\text{-}240}$U [108-113] isotopes are available up to spins 22^+, 20^+, 30^+, 30^+, 30^+, 12^+ respectively. The yrast spectra have been obtained for prolate deformation as these nuclei are observed to be prolate in their ground state. It is seen from Fig. 2.1 that the PSM calculation reproduces the available yrast energy levels up to known spins qualitatively. The maximum absolute energy difference (in MeV) between theory and experiment for highest known spins is 0.032, 0.210, 0.144, 0.019, 0.255, 0.067 MeV for $^{230\text{-}240}$U, respectively. It is seen that energy levels of these nuclei are reproduced well by present calculation by taking set of Nilsson parameters suggested by Rozmej [103].

2.3.4 *Yrast Spectra of $^{236\text{-}242}$Pu*

In Fig. 2.2, a comparison of calculated and experimental yrast energies of $^{236\text{-}242}$Pu isotopes are presented. The experimental level scheme of positive parity yrast bands for $^{236\text{-}242}$Pu [111-114] isotopes are available up to spins 16^+, 26^+, 30^+, 26^+, respectively. It is seen from Fig. 2.2 that the PSM calculation reproduces the available yrast energy levels up to known spins qualitatively. The maximum absolute energy difference between

theory and experiment for highest known spins is 0.14, 0.019, 0.073, 0.286 MeV for $^{236-242}$Pu, respectively.

2.3.5 *Structure of yrast bands of $^{230-240}$U*

Fig. 2.3(a) represents the band diagram of ^{230}U. In this nucleus, the yrast states up to spin I=18^+ are seen to arise from the 0-qp intrinsic state. Between spins 18^+ and 20^+, the ground state band is crossed by one 2-qp neutron band having configuration $2\nu j_{15/2}$(-3/2, 5/2) K=1. Between spins 18^+ to 22^+, the ground state band is crossed by five 2-qp neutron and one 2-qp proton bands having configurations $2\nu j_{15/2}$(-3/2,5/2) K=1, $2\nu j_{15/2}$(5/2,-7/2) K=-1, $2\nu j_{15/2}$(-3/2,-3/2) K=0, $2\nu j_{15/2}$(-3/2,-7/2) K= 2, $2\nu j_{15/2}$(5/2,5/2) K=0 and $2\pi i_{13/2}$(-3/2,5/2) K=1. Thus, the yrast band from spin I=0^+ to 18^+ arise from 0-qp state and above spin 18^+ to 24^+ arise from 2-qp bands. Above spin 26^+ multiple 2-qp bands contribute to the yrast band.

Fig 2.3(b) represents band diagram of ^{232}U, wherein, the yrast states up to spin I=18^+ are seen to arise from the 0-qp intrinsic state. At spin 20^+, the ground state band is crossed by two 2-qp neutron bands having configurations $2\nu j_{15/2}$(-3/2, 5/2) K=1 and $2\nu j_{15/2}$(5/2, -7/2) K=-1. At spin 22^+, the ground state band is crossed by three 2-qp neutron bands having configurations $2\nu j_{15/2}$(-3/2, -3/2) K=0, $2\nu j_{15/2}$(-3/2, -7/2) K=2 and $2\nu j_{15/2}$(5/2, 5/2) K=0. Thus, the yrast states of yrast band in ^{232}U arise from 0-qp state up to spin 18^+ and between spins 20^+ to 24^+, the yrast states arise from the superposition of two-2qp neutron bands. Above spin 24^+, the yrast states of yrast band arise from multiple 2qp bands.

Fig 2.3(c) represents the band diagram of ^{234}U. In case of ^{234}U, the yrast states up to spin I=16^+ are seen to arise from the 0-qp intrinsic state. Between spins 18^+ and 20^+, the ground state band is crossed by one 2-qp neutron band having configuration $2\nu j_{15/2}$(5/2, -7/2) K=-1. Between spins 22^+ and 24^+, the ground state band is crossed by one 2qp proton band having configuration $2\pi i_{13/2}$(-3/2, 5/2) K=1. Between spins 24^+ to 26^+ ground state band is crossed by two 2qp proton bands having configurations $2\pi i_{13/2}$(1/2,-3/2) K=-1 and $2\pi i_{13/2}$(-3/2,-3/2) K=0. Thus the yrast band in ^{234}U arise from 0-qp intrinsic state up to spin 18^+ and between spins 20^+ to 26^+, the yrast band arise from

2qp neutron band. Above spin 26^+, the yrast band is seen to arise from the one 2qp neutron and one 2qp proton bands.

Fig 2.3(d) represents the band diagram of ^{236}U. In case of ^{236}U, the yrast states up to spin I=18^+ are seen to arise from the 0-qp intrinsic state. At spin 20^+, the ground state band is crossed by one 2-qp neutron band having configuration $2\nu j_{15/2}(5/2, -7/2)$ K=-1. At spin 22^+, the ground state band is crossed by two 2qp neutron and one 2qp proton bands having configurations $2\nu j_{15/2}(-7/2, 9/2)$ K=1, $2\nu j_{15/2}(-7/2, -7/2)$ K=0 and $2\pi i_{13/2}(-3/2, 5/2)$ K=1. Thus the yrast states of yrast band in ^{236}U are seen to arise from 0-qp intrinsic state up to spin 18^+ and between spins 20^+ to 26^+, the yrast states arise from one 2qp neutron band. However, the yrast state at higher spins $I \geq 26^+$ are seen to arise from multiple 2qp proton and neutron bands.

Fig 2.3(e) represents the band diagram of ^{238}U. In of case ^{238}U, the yrast states up to spin I=18^+ are seen to arise from the 0-qp intrinsic state. At spin 20^+, one 2-qp neutron band having configuration $2\nu j_{15/2}(-7/2, 9/2)$ K=1 crosses the ground state band and becomes lowest in energy. At spin 22^+, the 2qp neutron band is crossed by one 2qp proton band having configuration $2\pi i_{13/2}(-3/2, 5/2)$ K=1. Thus the yrast states of yrast band in ^{238}U, arise from pure 0-qp band up to spin 18^+. Above spin 18^+, the yrast states arise from 2qp neutron band. However at higher spins $I \geq 24^+$, the yrast states are seen to arise from the two 2qp proton bands.

Fig 2.3(f) represents the band diagram of ^{240}U. In of case ^{240}U, the yrast states up to spin I=16^+ are seen to arise from the 0-qp intrinsic state. At spin 18^+, the ground state band is crossed by one 2-qp neutron band having configuration $2\nu j_{15/2}(-7/2, 9/2)$ K=1. At spin 26^+, the 2qp neutron band is crossed by two 2qp proton bands having configurations $2\pi i_{13/2}(-3/2, 5/2)$ K=-1, $2\pi i_{13/2}(1/2, 5/2)$ K=-2. Thus the yrast states of yrast band in ^{240}U arise from pure 0-qp band up to spin 16^+. Between spins 20^+ to 24^+ the yrast states are seen to arise from 2qp neutron bands. However at higher spin $I \geq 26^+$, the yrast state are seen to arise from 2qp proton bands.

2.3.6 *Structure of yrast bands of $^{236\text{-}242}$Pu*

Fig 2.4(a) represents the band diagram of ^{236}Pu, which indicates that the yrast states up to spin I=18^+ are seen to arise from 0-qp intrinsic state. At spin 20^+, the ground state band is crossed by one 2-qp neutron band having configuration $2\nu j_{15/2}(5/2,-7/2)$ K=-1. Between spins 22^+ and 24^+ one 2qp proton band having configuration $2\pi i_{13/2}(5/2, -7/2)$ K=-1 crosses the ground state band and contribute to the yrast states in addition to 2qp neutron band. However, at higher spin one 4qp band having configuration $2\nu j_{15/2}(5/2,-7/2) + 2\pi i_{13/2}(5/2,-7/2)$ K=-2 contribute to the yrast band.

Fig 2.4(b) represents the band diagram of ^{238}Pu. In of case ^{238}Pu, the yrast states up to spin I=20^+ are seen to arise from the 0-qp intrinsic state. From spins 20^+ to 24^+, the ground state band is crossed by three 2qp neutron and two 2qp proton bands having configurations $2\nu j_{15/2}(5/2,-7/2)$ K=-1, $2\nu j_{15/2}(-7/2,9/2)$ K=1, $2\nu j_{15/2}(-7/2,-7/2)$ K=0, $2\pi i_{13/2}(-3/2,5/2)$ K=1 and $2\pi i_{13/2}(5/2,-7/2)$ K=-1 However at the higher spin I $\geq 26^+$, one 4qp band having configuration $2\nu j_{15/2}(5/2,-7/2) + 2\pi i_{13/2}(-5/2,-7/2)$ K=-2 also contribute to the yrast states in addition to 2qp bands.

Fig 2.4(c) represents the band diagram of ^{240}Pu, the yrast states up to spin I=18^+ are seen to arise from the 0-qp intrinsic state. At spin 20^+, the ground state band is crossed by one 2-qp neutron band having configuration $2\nu j_{15/2}(-7/2, 9/2)$ K=1. Between spins 22^+ to 26^+ the ground state band is crossed by two 2qp neutron and three 2qp proton bands having configurations $2\nu j_{15/2}(5/2, -7/2)$ K=-1, $2\nu j_{15/2}(-7/2, -7/2)$ K=0, $2\pi i_{13/2}(-3/2,5/2)$ K=1, $2\pi i_{13/2}(5/2,-7/2)$ K=-1 and $2\pi i_{13/2}(1/2,-5/2)$ K=-2. Thus, the yrast states of yrast band upto 18^+ arise from 0-qp band and above spin 18^+ the yrast states are seen to arise from superposition of multiple 2qp proton and neutron bands.

Fig 2.4(d) represents the band diagram of ^{242}Pu, the yrast states up to spin I= 16^+ are seen to arise from the 0-qp intrinsic state. At spin 18^+, the ground state band is crossed by one 2qp neutron band having configuration $2\nu j_{15/2}(-7/2, 9/2)$ K=1. Between spins 20^+ to 26^+, the ground state is crossed by two 2qp neutron and six 2qp proton bands having configurations $2\nu j_{15/2}(5/2, -7/2)$ K=-1, $2\nu j_{15/2}(5/2, 5/2)$ K=0, $2\pi i_{13/2}(-7/2, -7/2)$ K=0, $2\pi i_{13/2}(-3/2, 5/2)$ K=1, $2\pi i_{13/2}(5/2, -7/2)$ K=-1 , $2\pi i_{13/2}(1/2, 5/2)$ K=-2 , $2\pi i_{13/2}(-3/2, -$

3/2) K=0 and $2\pi i_{13/2}$(-3/2, -7/2) K=2. However, at higher spin I > 28^+, one 4qp band also contribute to the yrast states.

2.3.7 Electromagnetic quantities

2.3.7.1 *B(E2) transition probabilities of $^{230\text{-}240}U$*

B(E2) transition probabilities can disseminate strategic information on the nuclear structure and provide stringent test of a particular model. The reduced transition probabilities *B(E2)s* from the initial state $I_i = I$ to the final state $I_f = I\text{-}2$ are given by [97]

$$B(E2; I \to I-2) = \frac{1}{2I+I}\left|\langle\psi^{I-2}||\hat{Q}_2||\psi^{I}\rangle\right|^2 \qquad (2.52)$$

in which the wave functions $|\psi^I\rangle$ are those of eq. (2.34). The operator Q_2 is related to the quadrupole operators by

$$Q_{2\upsilon} = e_{\upsilon}^{eff}\sqrt{\frac{5}{16\pi}}Q_{\upsilon}^2$$

$$Q_{2\pi} = e_{\pi}^{eff}\sqrt{\frac{5}{16\pi}}Q_{\pi}^2,$$

where π and ν are for protons and neutrons, respectively. In the calculation, we have used the effective charge for neutrons $e_{\nu}^{eff} = 0.5e$ and for protons $e_{\pi}^{eff} = 1.5e$

The transition probability *B(E2)* values obtained from the PSM wave function for $^{230\text{-}240}$U isotopes are presented in Table 2.9. The experimental data for *B(E2)* values of $^{230\text{-}234}$U, ^{238}U are available for $2_1^+ \to 0_1^+$ transition [108-113] only. In case of ^{236}U the experimental data is available up to spin 20^+ [111]. The calculated B(E2; $2_1^+ \to 0_1^+$) values are in good agreement with experimental data for all the U isotopes. Experimentally, the dip in the *B(E2)* values of ^{236}U is observed at spin 16^+ but the theoretical values show a dip at spin 20^+. The dip in the *B(E2)* values could be due to change in the structure of yrast band due to crossing of g-band by 2qp bands. The experimental data of *B(E2)* values for higher spins in $^{230\text{-}234}$U, ^{238,240}U are not available, so one cannot make any comment.

2.3.7.2 *B(E2) transition probabilities of $^{236\text{-}242}$Pu*

The transition probability *B(E2)* values obtained from the PSM wave function for $^{236\text{-}242}$Pu isotopes are presented in Table 2.10. The experimental data for *B(E2)* values of $^{238\text{-}242}$Pu nuclei are available for $2_1^+ \rightarrow 0_1^+$ transition [111-114] only. The calculated B(E2; $2_1^+ \rightarrow 0_1^+$) values are in good agreement with experimental data for all the Pu isotopes. The experimental data of *B(E2)* values for higher spins are not available, so one cannot make any comment.

2.3.7.3 *g-factors of $^{230\text{-}240}$U*

A gyromagnetic factor (*g*-factor) is a quantity very sensitive to single particle components in wave functions as well as to their interplay with collective degrees of freedom. By studying *g*-factors one can gain information of specific neutron and proton orbitals in the structure. In the PSM, *g*-factors [97] can be directly computed by

$$g(I) = \frac{\mu(I)}{\mu_N I} = \frac{1}{\mu_N I}\left[\mu_\pi(I) + \mu_\nu(I)_\nu\right] \tag{2.53}$$

with $\mu_\tau(I)$ being the magnetic moment of a state $|\psi^I\rangle$, expressed as

$$\mu_\tau(I) = \left\langle \psi_I^I \middle| \hat{\mu}_z^\tau \middle| \psi_I^I \right\rangle$$

$$= \frac{I}{\sqrt{(I(I+1)}} \left\langle \psi^I \middle| \middle| \hat{\mu}^\tau \middle| \middle| \psi^I \right\rangle$$

$$= \frac{I}{\sqrt{(I(I+1)}} \left[g_l^\tau \left\langle \psi^I \middle| \middle| \hat{j}^\tau \middle| \middle| \psi^I \right\rangle + (g_s^\tau - g_l^\tau) \left\langle \psi^I \middle| \middle| \hat{s}^\tau \middle| \middle| \psi^I \right\rangle \right],$$

where, $\tau = \pi$ and υ for protons and neutrons, respectively. The following standard values for g_l and g_s are taken:

$$g_l^\pi = 1, \qquad g_s^\pi = 5.586 \times 0.75,$$

$$g_l^{\upsilon} = 0, \qquad g_s^{\upsilon} = -3.826 \times 0.75,$$

where g_l^{π} and g_s^{υ} are damped by a usual factor 0.75 from the free-nucleon values to account for the core-polarization and meson-exchange current corrections [99,115,116].

In Fig. 2.5 the results of *g*-factors obtained theoretically for $^{230\text{-}240}$U are presented. The experimental values for *g* factors are only available for ^{238}U. For this nucleus, a comparison of calculated and observed values is also presented in the same figure. The predicted values of *g*-factors in all U isotopes show a meager variation with spin upto 18^+. From the analysis of band diagrams, it is seen that the energy states upto spin 18^+ of all these isotopes arise from nearly only one zero quasi-particle configuration in which all nucleons are paired. Therefore, g-factors of these isotopes upto spin 18^+ are not showing much variation. In the same figure, the theoretical value of *g*-factors show a decrease at certain spin in ^{230,232}U isotopes thereafter, the theoretical *g*-factors show an increasing trend. For example, in case of ^{230}U, the theoretical *g*-factor has a value 0.2515 at spin 18^+ whereas its value at spin 20^+ decreases to 0.0329, thereafter it starts increasing with spin. Similar trend is obtained for g-factors of ^{232}U. These results can be understood from the band diagrams presented in Fig 2.3 (a) for ^{230}U, the ground state band is crossed by 2qp neutron bands arising from $1j_{15/2}$ orbit. The decrease in the g-factors around the crossing region could be due to the alignment of neutrons in the $1j_{15/2}$ orbit. In case of $^{234\text{-}240}$U, the *g*-factors shows a reverse trend. In these isotopes *g*-factor values, show an increase after the band crossing. For example in case of ^{234}U the value of *g*-factor at spin 22^+ is 0.1521 whereas at spin 24^+ the value shows an increase to 0.2018. In case of ^{238}U the experimental values of *g*-factor are known up to spin 24^+ and there is experimental evidence [40] that an increase in g-factors at spin (18-24) is attributed to rotational alignment of protons in $1i_{13/2}$ orbit. From the band diagram (Fig. 2.3(e) for ^{238}U), it is seen that at spin 22^+, the *g*-band is crossed by 2qp proton bands arising from $1i_{13/2}$ orbit.

2.3.7.4 *g-factors of $^{236\text{-}242}$Pu*

In Fig. 2.6 the results of *g*-factors obtained theoretically for $^{236\text{-}242}$Pu isotopes are presented. In $^{236\text{-}242}$Pu isotopes, all these isotopes show an increase in the value of g-factors above spin 18^+. For example in case of ^{236}Pu, the *g*-factor value increases from

0.388 at spin 24^+ to 0.4632 at spin 26^+. The increase in the *g*-factors at higher spins in all these isotopes is due to crossing of *g*-band by 2qp proton bands from $1i_{13/2}$ orbit. The present calculation predicts an increase in g-factors at higher spin in Pu isotopes due to alignment of protons in $1i_{13/2}$ orbit. The experimental values of *g*-factors of $^{236\text{-}242}$Pu are not known, so one cannot make any comment regarding the level of agreement.

2.4 Summary

i. The PSM calculations performed with the quadrupole-quadrupole plus monopole and quadrupole pairing force reproduce the observed deformation systematics in $^{230\text{-}240}$U and $^{236\text{-}242}$Pu isotopes.

ii. The deformation systematics in these nuclei depend on the pattern of occupation probabilities of $(1h_{11/2})_\pi$ orbit. The observed deformation trend of low-lying states in $^{230\text{-}240}$U and $^{236\text{-}242}$Pu isotopes could also be linked with the occupation of down-sloping components of high *j* orbits in the valence space.

iii. The calculated yrast positive parity bands in $^{230\text{-}240}$U and $^{236\text{-}242}$Pu show good agreement with the experimental data. The experimental level scheme of positive parity yrast bands for $^{230\text{-}240}$U and $^{236\text{-}242}$Pu isotopes are available up to spins 22^+, 20^+, 30^+, 30^+, 30^+, 12^+ and 16^+, 26^+, 30^+, 26^+, respectively which are reproduced by the PSM calculations.

iv. The results on band diagrams predict that in all $^{230\text{-}240}$U and $^{236\text{-}242}$Pu isotopes, the yrast states upto spin $I \approx 18^+$ arise from 0-qp band (ground state). At higher spins the ground state band is crossed by 2-qp neutron and proton bands and contributes to the yrast states.

v. The calculated values of B(E2; $2_1^+ \rightarrow 0_1^+$) transition probability are in agreement with the available experimental data for all the $^{230\text{-}240}$U and $^{236\text{-}242}$Pu isotopes . In case of ^{236}U the experimental B(E2) values for higher transition are available upto spin 20^+ which are reproduced by the present calculation. The present calculation has predicted the B(E2) values for higher transitions for $^{230\text{-}234}$U, $^{238\text{-}240}$U and $^{236\text{-}242}$Pu isotopes.

vi. The calculated values of *g*-factors in all $^{230\text{-}240}$U and $^{236\text{-}242}$Pu isotopes show a slight variation with spin upto 18^+ because the energy states upto spin 18^+ arise from almost single zero qp configuration in which all the nucleons are paired. The theoretical *g*-factors, in case of ^{230,232}U, show a decrease above spin 18^+ due to crossing of *g*-band by 2qp neutron bands. However, in case of $^{234\text{-}240}$U, the *g*-factors shows a reverse trend. In these isotopes the *g*-factors show an increase after the band crossing region due to the crossing of *g*-band by 2qp proton bands. In case of ^{238}U, the theoretical values of *g*-factors follow the same trend as followed by the measured values and confirm the observed proton alignment in ^{238}U at higher spin.

vii. The theoretical results of *g*-factors of $^{236\text{-}242}$Pu isotopes predict an increase in *g*-factors at higher spins arising theoretically due to alignment of protons in $1i_{13/2}$ orbit. However, this feature in these isotopes remains to be verified experimentally.

Table 2.1 Quadrupole and hexadecapole deformation parameters used in the present calculations for $^{230\text{-}240}$U isotopes.

Nucleus	^{230}**U**	^{232}**U**	^{234}**U**	^{236}**U**	^{238}**U**	^{240}**U**
ε_2	0.240	0.240	0.250	0.250	0.255	0.250
ε_4	-0.025	-0.025	-0.035	-0.035	-0.025	0.020

Table 2.2 Comparison of experimental (Exp.) and calculated (Th.) excitation energies (in units of MeV) of $2_1^+(E_2^+)$, $4_1^+(E_4^+)$ *and* E_4^+/E_2^+ ratios for $^{230\text{-}240}$U isotopes.

Nucleus	**Exp.**			**Th.**		
	E_2^+	E_4^+	E_4^+/E_2^+	E_2^+	E_4^+	E_4^+/E_2^+
^{230}U	0.052	0.169	3.250	0.051	0.167	3.27
^{232}U	0.048	0.157	3.270	0.047	0.156	3.319
^{234}U	0.044	0.143	3.320	0.043	0.141	3.279
^{236}U	0.045	0.150	3.330	0.043	0.142	3.302
^{238}U	0.045	0.148	3.289	0.045	0.148	3.288
^{240}U	0.045	0.151	3.356	0.045	0.150	3.333

Table 2.3 The BCS sub-shell occupation numbers of protons in the ground state of $^{230\text{-}240}$U isotopes.

Nucleus	**^{230}U**	**^{232}U**	**^{234}U**	**^{236}U**	**^{238}U**	**^{240}U**
$3p_{1/2}$	0.128	0.129	0.143	0.144	0.143	0.112
$3p_{3/2}$	0.513	0.514	0.541	0.542	0.558	0.546
$2f_{5/2}$	0.658	0.659	0.687	0.688	0.707	0.710
$2f_{7/2}$	1.826	1.827	1.803	1.804	1.854	2.058
$1h_{9/2}$	3.733	3.742	3.662	3.670	3.757	4.155
$1h_{11/2}$	11.166	11.162	11.116	11.111	10.998	10.783
$4s_{1/2}$	0.004	0.004	0.005	0.005	0.005	0.004
$3d_{3/2}$	0.007	0.007	0.008	0.008	0.008	0.008
$3d_{5/2}$	0.042	0.042	0.052	0.052	0.049	0.029
$2g_{7/2}$	0.025	0.026	0.028	0.028	0.029	0.029
$2g_{9/2}$	0.430	0.430	0.483	0.483	0.486	0.403
$1i_{11/2}$	0.099	0.100	0.102	0.103	0.108	0.118
$1i_{13/2}$	4.209	4.199	4.238	4.229	4.286	4.290

Table 2.4 The BCS sub-shell occupation numbers of neutrons in the ground state of $^{230\text{-}240}$U isotopes.

Nucleus	^{230}**U**	^{232}**U**	^{234}**U**	^{236}**U**	^{238}**U**	^{240}**U**
$4s_{1/2}$	0.187	0.194	0.230	0.289	0.348	0.386
$3d_{3/2}$	0.317	0.334	0.418	0.572	0.715	0.751
$3d_{5/2}$	1.117	1.150	1.192	1.226	1.307	1.472
$2g_{7/2}$	1.148	1.194	1.282	1.362	1.452	1.549
$2g_{9/2}$	3.156	3.320	3.422	3.800	4.325	4.893
$1i_{11/2}$	3.857	4.143	4.414	4.750	5.107	5.923
$1i_{13/2}$	12.738	13.094	13.375	13.546	13.590	13.500
$4p_{1/2}$	0.003	0.003	0.003	0.003	0.003	0.001
$4p_{3/2}$	0.014	0.014	0.019	0.020	0.018	0.005
$3f_{5/2}$	0.009	0.009	0.010	0.011	0.009	0.004
$3f_{7/2}$	0.111	0.114	0.146	0.151	0.144	0.072
$2h_{9/2}$	0.025	0.023	0.026	0.028	0.027	0.015
$2h_{11/2}$	0.811	0.860	0.992	1.035	1.094	1.016
$1j_{13/2}$	0.062	0.058	0.060	0.066	0.068	0.049
$1j_{15/2}$	4.345	4.700	5.010	5.445	6.038	6.694

Table 2.5 Quadrupole and hexadecapole deformation parameters used in the present calculations for $^{236\text{-}242}$Pu isotopes.

Nucleus	**^{236}Pu**	**^{238}Pu**	**^{240}Pu**	**^{242}Pu**
ε_2	0.275	0.265	0.260	0.250
ε_4	-0.045	-0.050	-0.020	0.020

Table 2.6 Comparison of experimental (Exp.) and calculated (Th.) excitation energies (in units of MeV) of $2_1^+(E_2^+)$, $4_1^+(E_4^+)$ and E_4^+/E_2^+ ratios for $^{236\text{-}242}$Pu isotopes.

Nucleus	**Exp.**			**Th.**		
	$\boldsymbol{E_2^+}$	$\boldsymbol{E_4^+}$	$\boldsymbol{E_4^+/E_2^+}$	$\boldsymbol{E_2^+}$	$\boldsymbol{E_4^+}$	$\boldsymbol{E_4^+/E_2^+}$
^{236}Pu	0.045	0.147	3.267	0.045	0.147	3.267
^{238}Pu	0.044	0.146	3.318	0.043	0.143	3.326
^{240}Pu	0.043	0.142	3.302	0.043	0.141	3.279
^{242}Pu	0.045	0.147	3.326	0.044	0.146	3.318

Table 2.7 The BCS sub-shell occupation numbers of protons in the ground state of $^{236\text{-}242}$Pu isotopes.

Nucleus	**^{236}Pu**	**^{238}Pu**	**^{240}Pu**	**^{242}Pu**
$3p_{1/2}$	0.172	0.162	0.150	0.118
$3p_{3/2}$	0.634	0.615	0.615	0.605
$2f_{5/2}$	0.773	0.745	0.751	0.745
$2f_{7/2}$	1.941	1.954	2.061	2.283
$1h_{9/2}$	3.983	4.084	4.216	4.540
$1h_{11/2}$	11.272	11.25	11.228	11.061
$4s_{1/2}$	0.007	0.007	0.005	0.004
$3d_{3/2}$	0.010	0.009	0.008	0.007
$3d_{5/2}$	0.075	0.072	0.050	0.029
$2g_{7/2}$	0.035	0.032	0.028	0.027
$2g_{9/2}$	0.636	0.605	0.539	0.445
$1i_{11/2}$	0.118	0.111	0.109	0.114
$1i_{13/2}$	4.907	4.90	4.893	4.891

.

Table 2.8 The BCS sub-shell occupation numbers of neutrons in the ground state of $^{236\text{-}242}$Pu isotopes.

Nucleus	**^{236}Pu**	**^{238}Pu**	**^{240}Pu**	**^{242}Pu**
$4s_{1/2}$	0.286	0.317	0.358	0.390
$3d_{3/2}$	0.554	0.649	0.732	0.755
$3d_{5/2}$	1.255	1.234	1.341	1.477
$2g_{7/2}$	1.398	1.416	1.479	1.555
$2g_{9/2}$	3.415	3.656	4.337	4.900
$1i_{11/2}$	4.478	4.723	5.106	5.913
$1i_{13/2}$	13.053	13.512	13.524	13.492
$4p_{1/2}$	0.008	0.008	0.003	0.001
$4p_{3/2}$	0.038	0.036	0.017	0.005
$3f_{5/2}$	0.024	0.022	0.010	0.004
$3f_{7/2}$	0.219	0.212	0.145	0.073
$2h_{9/2}$	0.052	0.047	0.028	0.015
$2h_{11/2}$	1.173	1.156	1.122	1.021
$1j_{13/2}$	0.096	0.089	0.070	0.050
$1j_{15/2}$	4.974	5.248	6.036	6.674

Table 2.9 Comparison of calculated (Th.) and experimental (Exp.) *B(E2)* reduced transition probabilities (in units of e^2b^2) for $^{230\text{-}240}$U isotopes. Experimental data are taken from Refs. [108-113].

Transition	^{230}U		^{232}U		^{234}U		^{236}U		^{238}U		^{240}U	
$(I_i^+ \longrightarrow I_f^+)$	Exp.	Th.	Exp.	Th.	Exp.	Th.	Exp.	Th.	Exp.	Th.	Exp.	Th.
$2 \longrightarrow 0$	$1.92^{+0.23}_{-0.23}$	1.982	$2.11^{+0.18}_{-0.18}$	2.008	$2.09^{+0.08}_{-0.08}$	2.207	$2.25^{+0.08}_{-0.08}$	2.284	$2.55^{+0.36}_{-0.36}$	2.452	-	2.473
$4 \longrightarrow 2$	-	2.843	-	2.878	-	3.158	$3.21^{+0.20}_{-0.20}$	3.269	-	3.508	-	3.539
$6 \longrightarrow 4$	-	3.154	-	3.188	-	3.488	$3.46^{+0.19}_{-0.19}$	3.611	-	3.874	-	3.909
$8 \longrightarrow 6$	-	3.334	-	3.365	-	3.664	$3.50^{+0.35}_{-0.35}$	3.796	-	4.071	-	4.109
$10 \longrightarrow 8$	-	3.466	-	3.489	-	3.778	$3.23^{+0.35}_{-0.35}$	3.918	-	4.201	-	4.240
$12 \longrightarrow 10$	-	3.574	-	3.588	-	3.856	$3.68^{+0.62}_{-0.62}$	4.010	-	4.300	-	4.337
$14 \longrightarrow 12$	-	3.666	-	3.669	-	3.904	$4.04^{+0.04}_{-0.04}$	4.081	-	4.377	-	4.411
$16 \longrightarrow 14$	-	3.744	-	3.719	-	3.918	$3.41^{+0.35}_{-0.35}$	4.130	-	4.440	-	4.458
$18 \longrightarrow 16$	-	3.787	-	3.605	-	3.903	$4.40^{+0.04}_{-0.04}$	4.121	-	4.476	-	4.455
$20 \longrightarrow 18$	-	0.052	-	2.581	-	3.911	$4.58^{+0.07}_{-0.07}$	3.858	-	4.441	-	4.329

Table 2.10 Comparison of calculated (Th.) and experimental (Exp.) *B(E2)* reduced transition probabilities (in units of e^2b^2) for $^{236\text{-}242}$Pu isotopes. Experimental data are taken from Refs. [111-114].

Transition	**^{236}Pu**		**^{238}Pu**		**^{240}Pu**		**^{242}Pu**	
$(I_i^+ \longrightarrow I_f^+)$	**Exp.**	**Th.**	**Exp.**	**Th.**	**Exp.**	**Th.**	**Exp.**	**Th.**
$2 \longrightarrow 0$	-	2.767	$2.522^{+0.034}_{-0.034}$	2.663	$2.60^{+0.06}_{-0.06}$	2.677	$2.68^{+0.032}_{-0.032}$	2.595
$4 \longrightarrow 2$	-	3.957	-	3.808	-	3.829	-	3.713
$6 \longrightarrow 4$	-	4.365	-	4.200	-	4.226	-	4.100
$8 \longrightarrow 6$	-	4.578	-	4.406	-	4.435	-	4.306
$10 \longrightarrow 8$	-	4.712	-	4.537	-	4.571	-	4.440
$12 \longrightarrow 10$	-	4.805	-	4.631	-	4.670	-	4.538
$14 \longrightarrow 12$	-	4.869	-	4.702	-	4.747	-	4.613
$16 \longrightarrow 14$	-	4.907	-	4.756	-	4.808	-	4.665
$18 \longrightarrow 16$	-	4.908	-	4.796	-	4.851	-	4.677
$20 \longrightarrow 18$	-	4.869	-	4.791	-	4.857	-	4.587

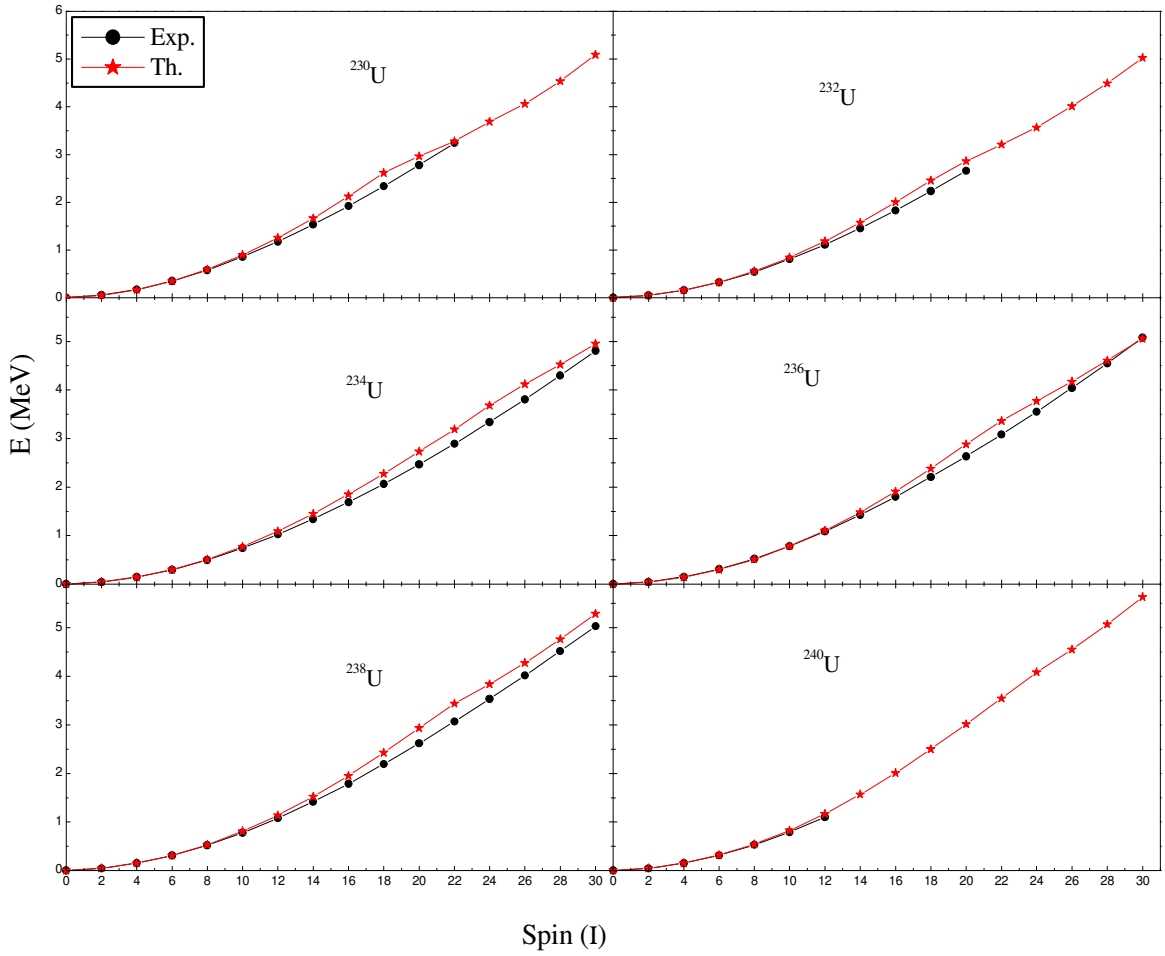

Fig. 2.1 Comparison of calculated (Th.) and experimental (Exp.) positive-parity yrast bands of even-even $^{230\text{-}240}$U isotopes. The experimental data are taken from Refs. [108-113].

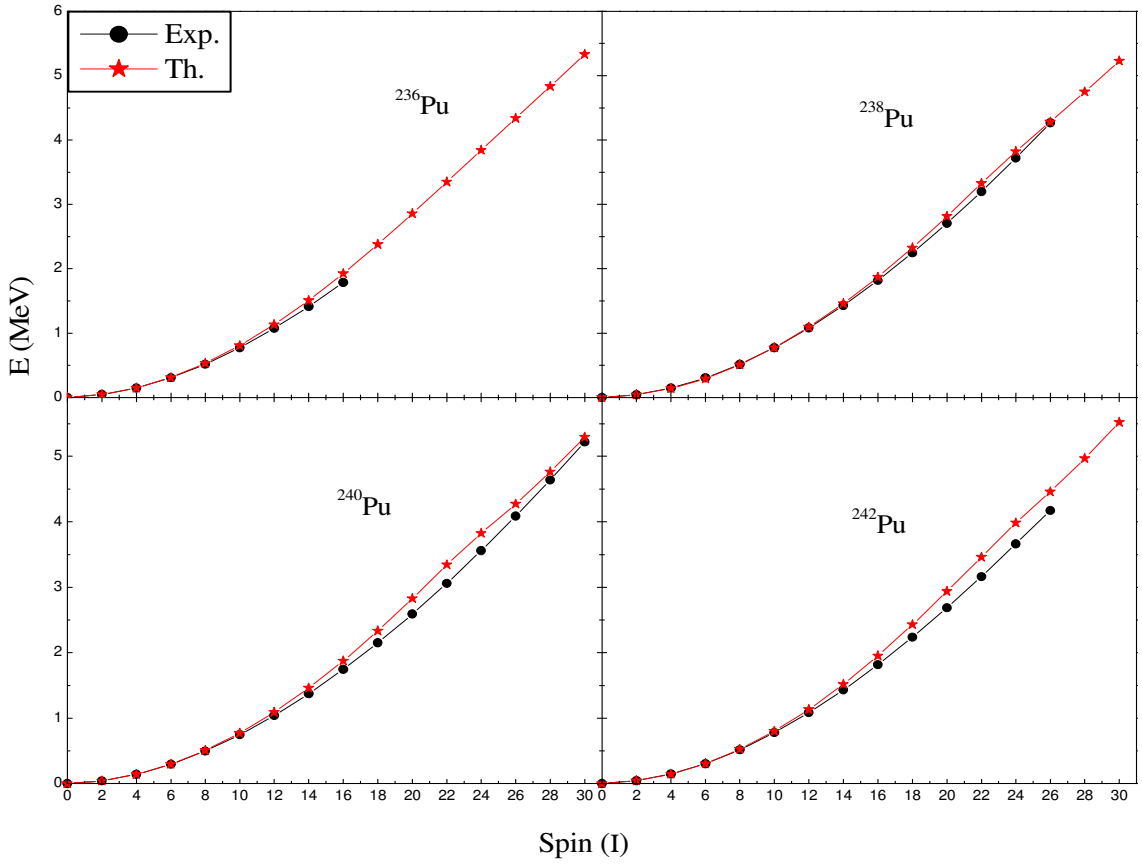

Fig. 2.2 Comparison of calculated (Th.) and experimental (Exp.) positive-parity yrast bands of even-even $^{236\text{-}242}$Pu isotopes. The experimental data are taken from Refs. [111-114].

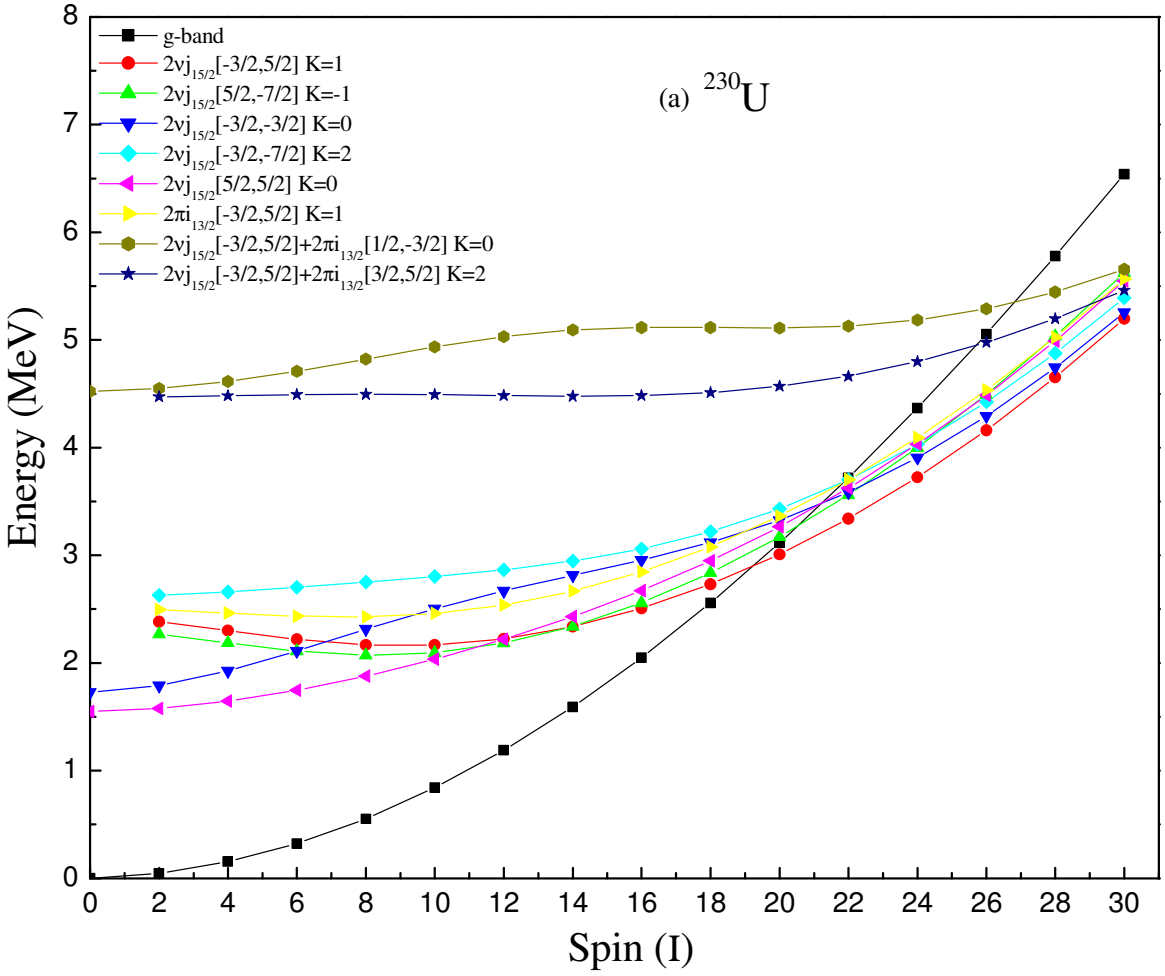

Fig. 2.3 Band diagrams (bands before configuration mixing) for (a) ^{230}U, (b) ^{232}U, (c) ^{234}U, (d) ^{236}U, (e) ^{238}U, (f) ^{240}U isotopes. Only the important lowest lying bands in each configuration are shown.

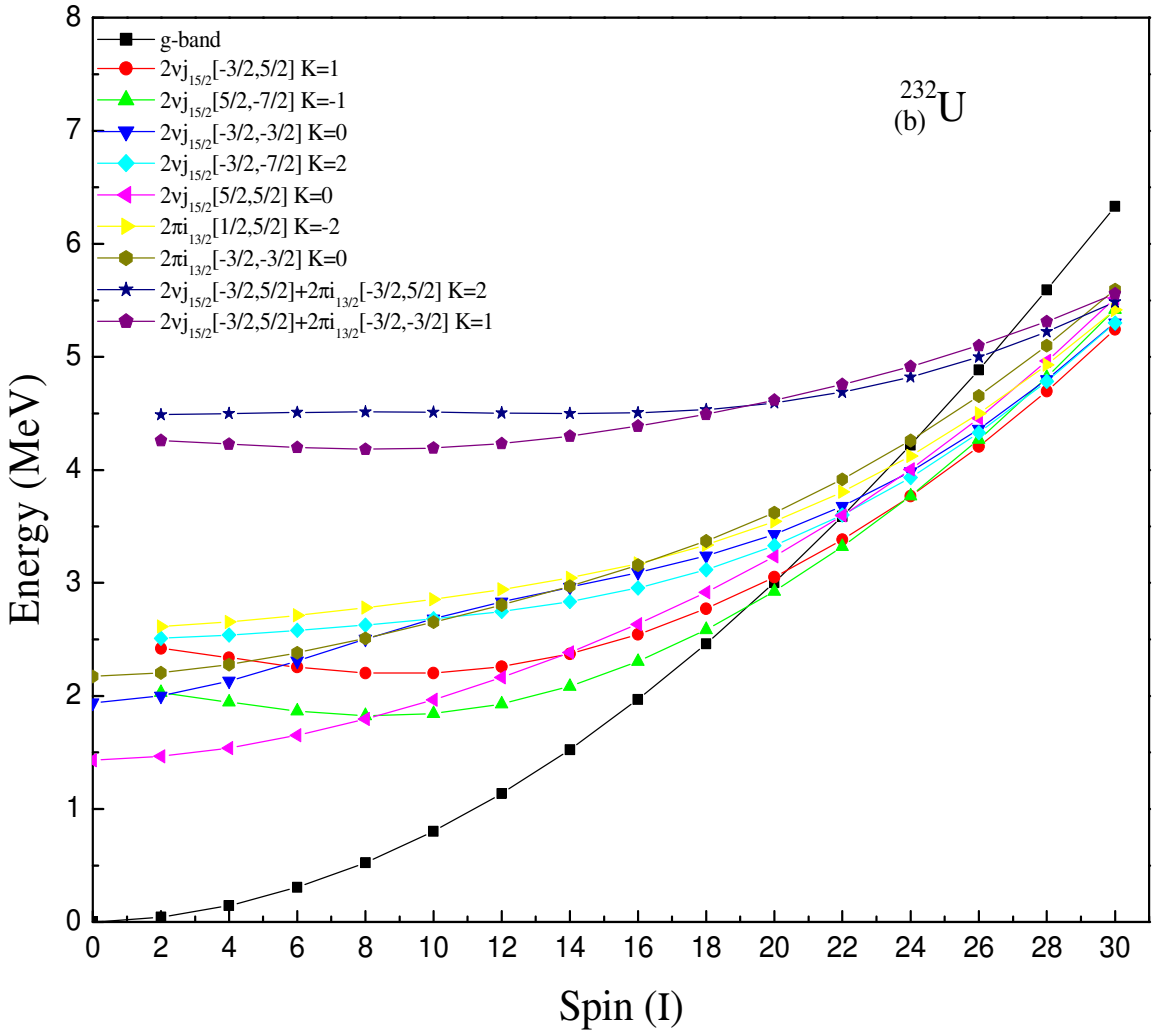

Fig. 2.3 (continued)

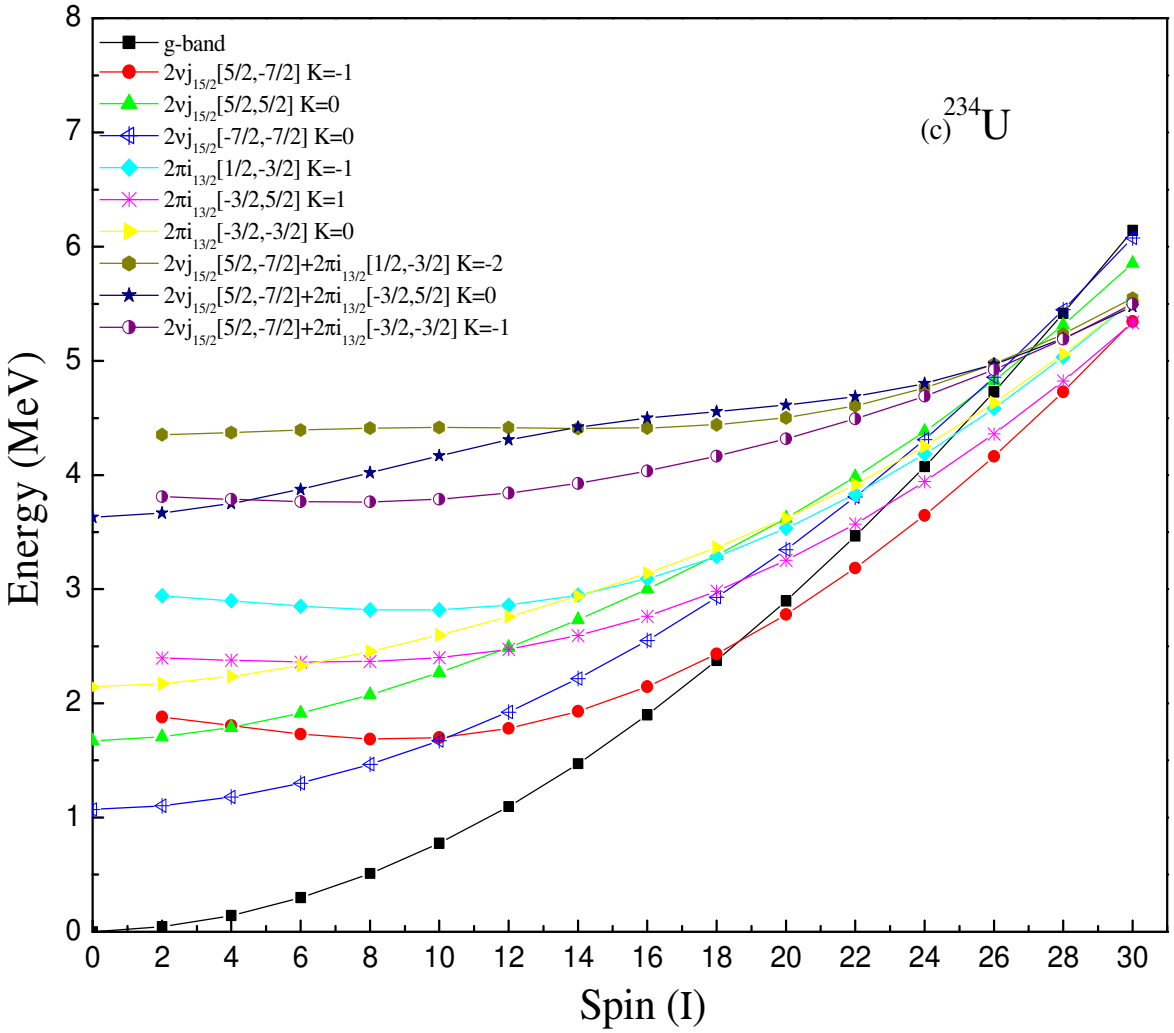

Fig. 2.3 (continued)

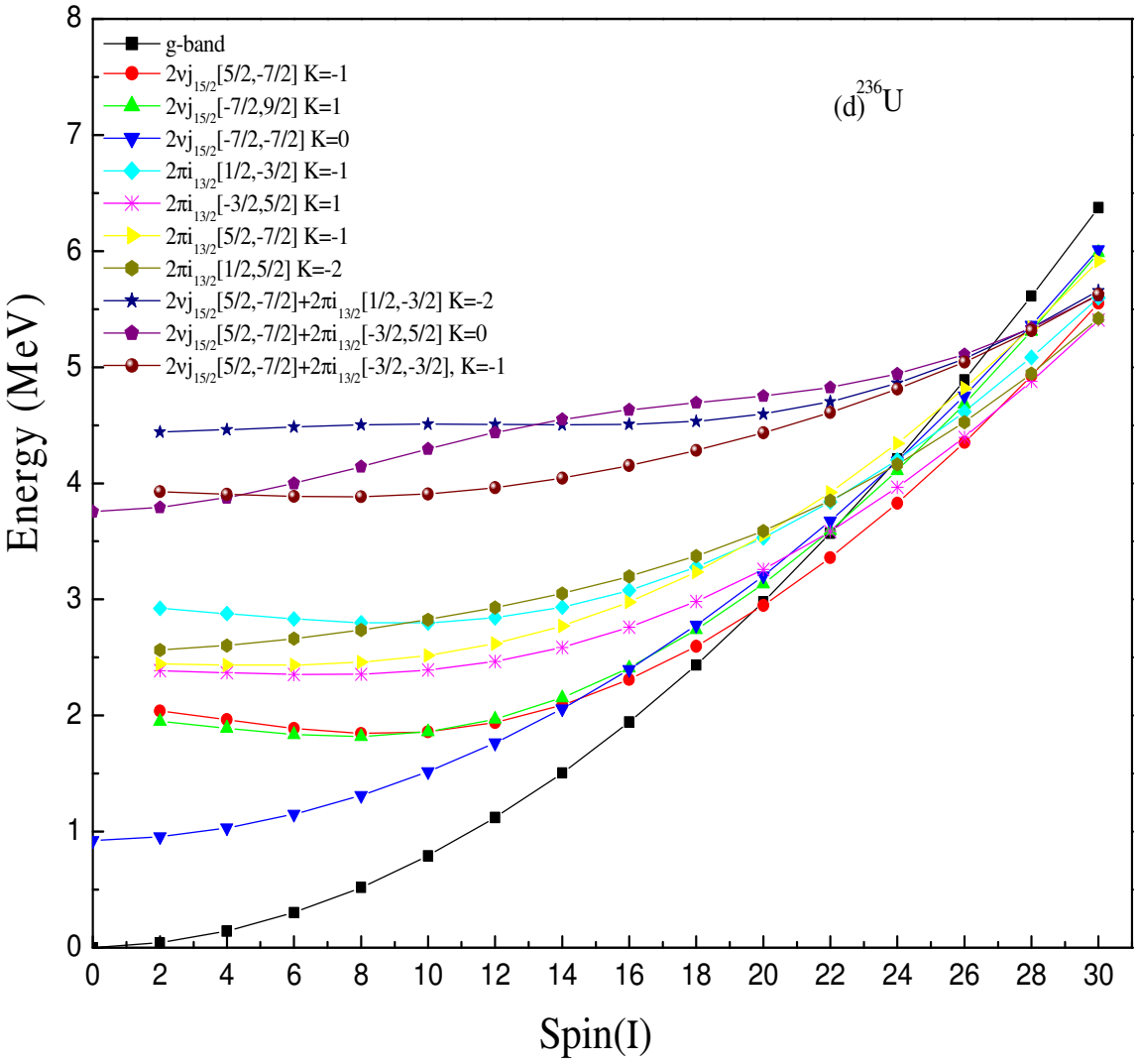

Fig. 2.3 (continued)

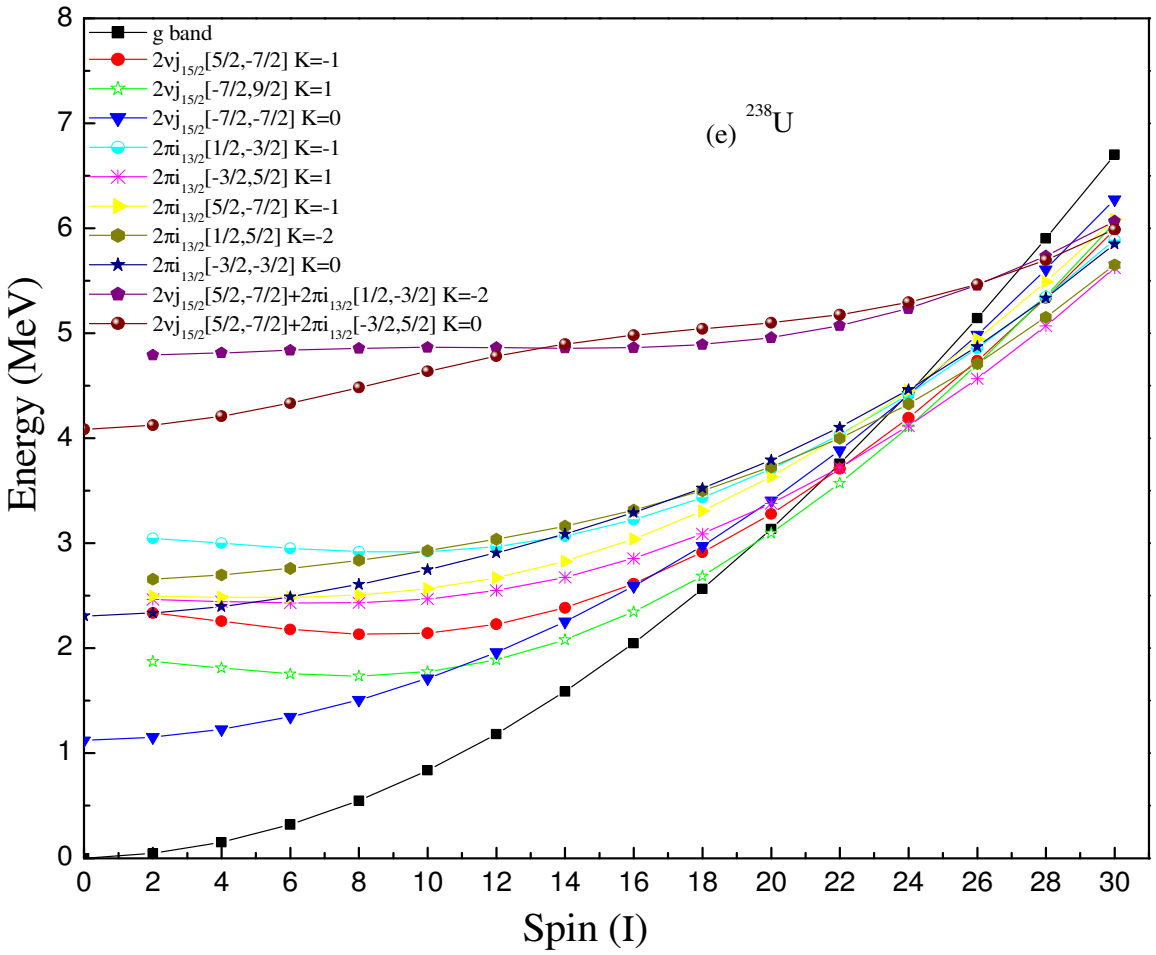

Fig. 2.3 (continued)

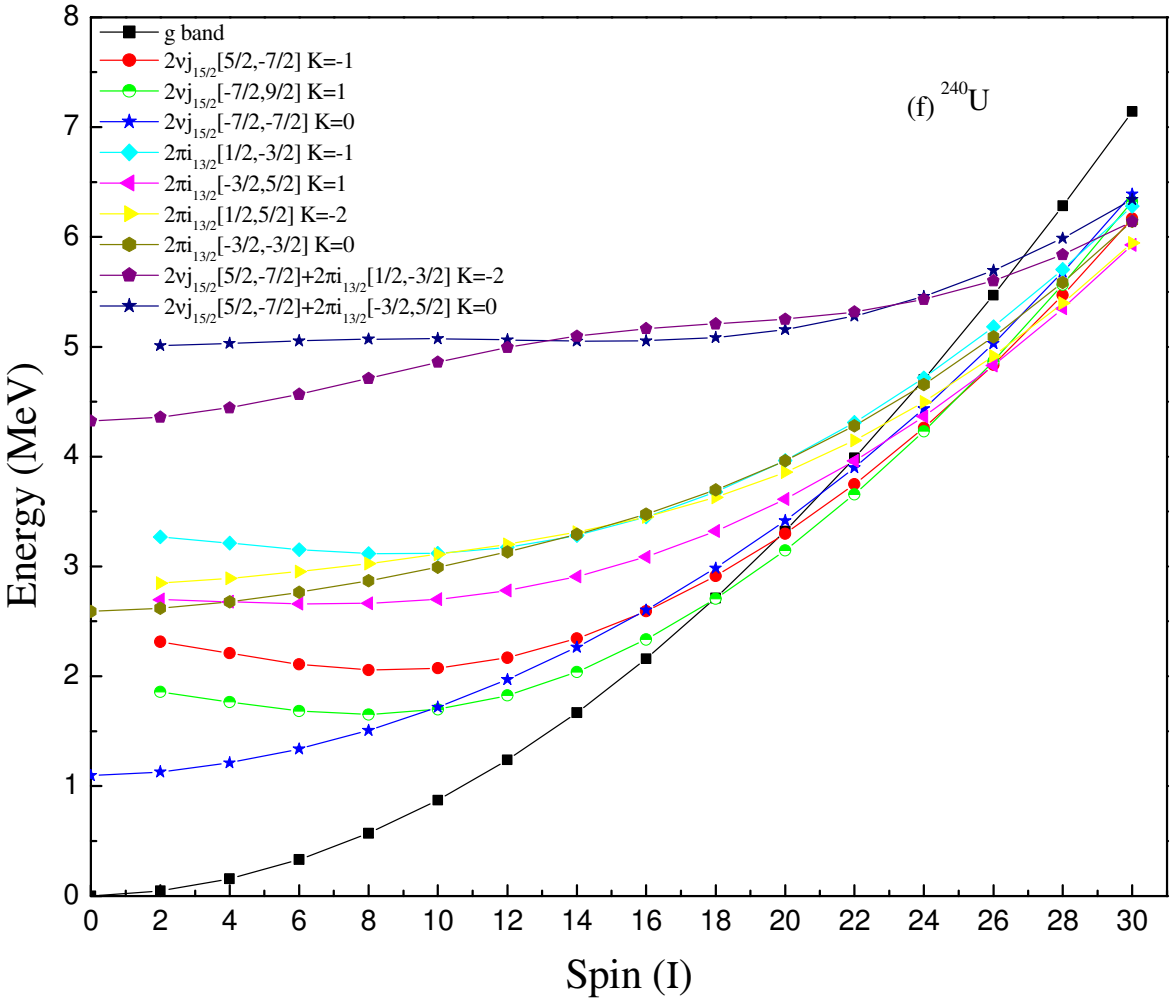

Fig. 2.3 (continued)

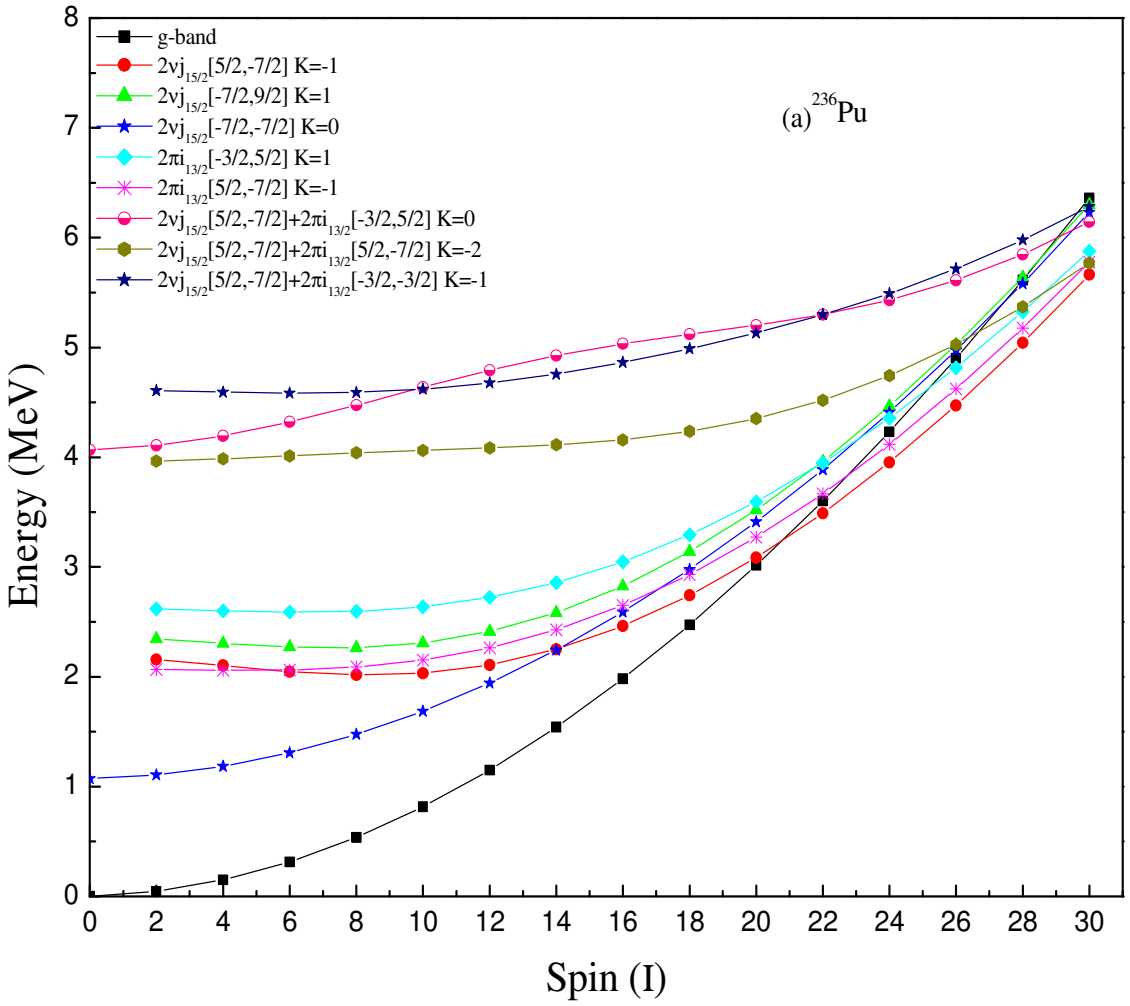

Fig. 2.4 Band diagrams (bands before configuration mixing) for (a) ^{236}Pu, (b) ^{238}Pu, (c) ^{240}Pu and (d) ^{242}Pu. Only the important lowest lying bands in each configuration are shown.

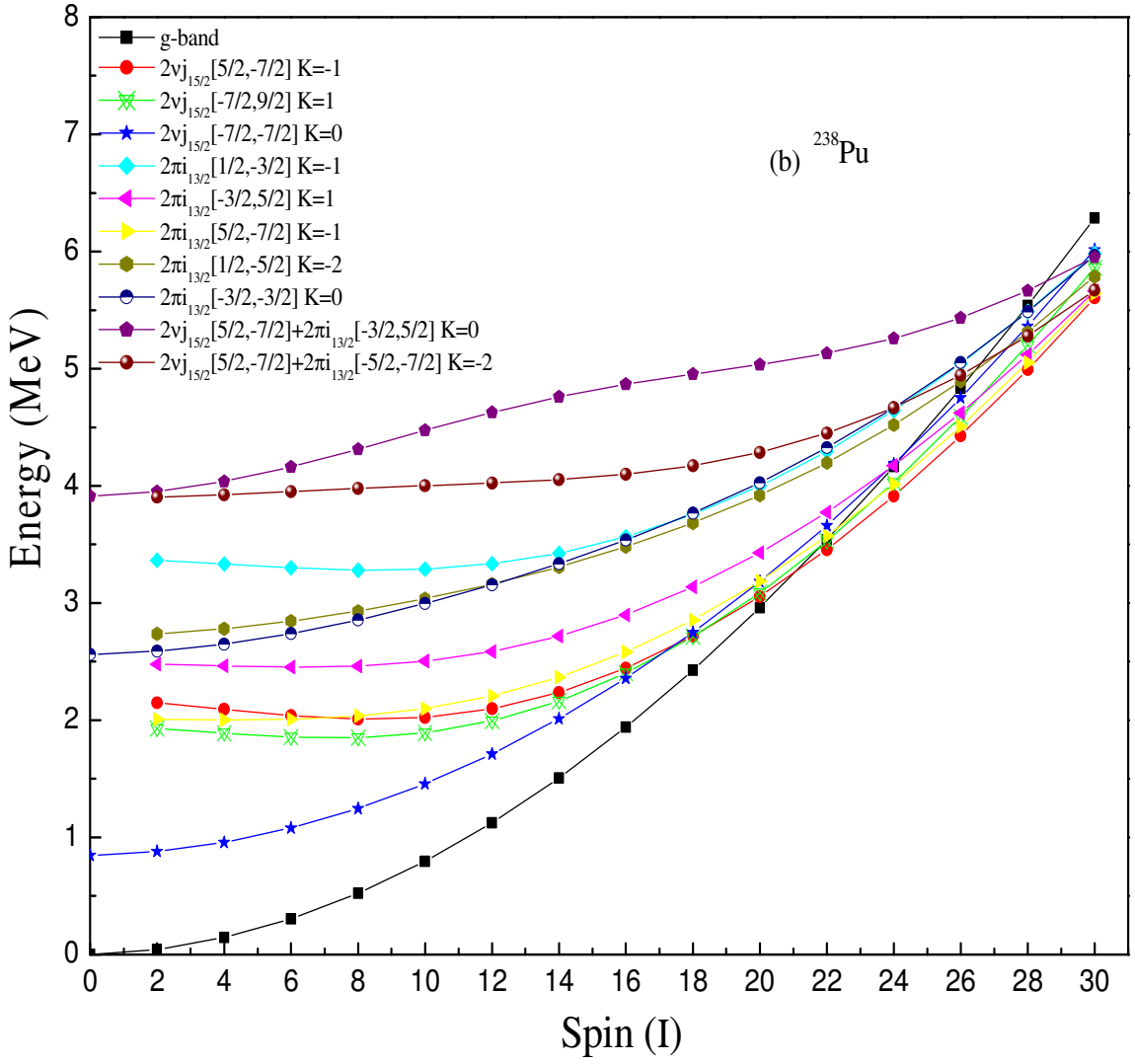

Fig. 2.4 (continued)

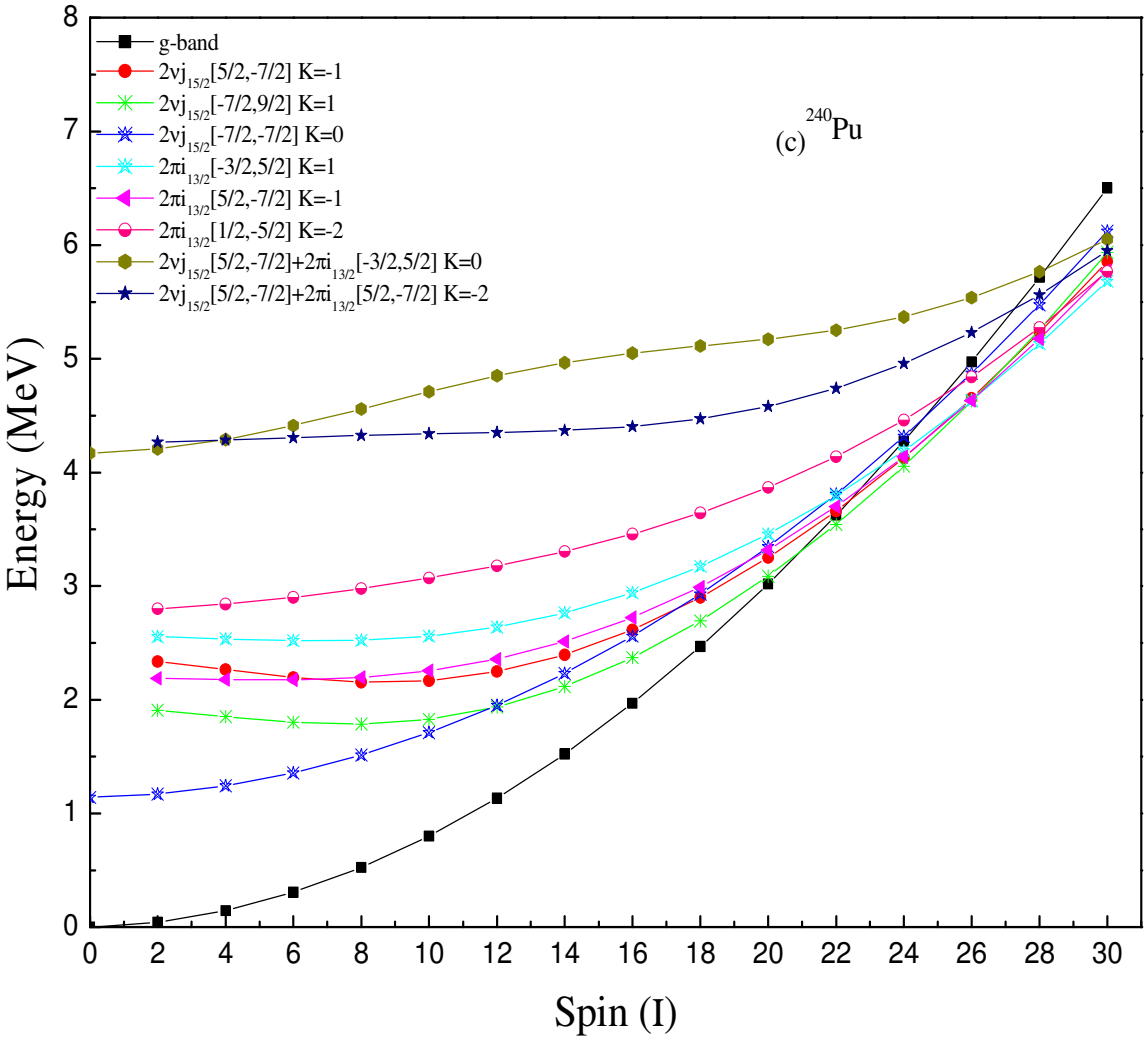

Fig. 2.4 (continued)

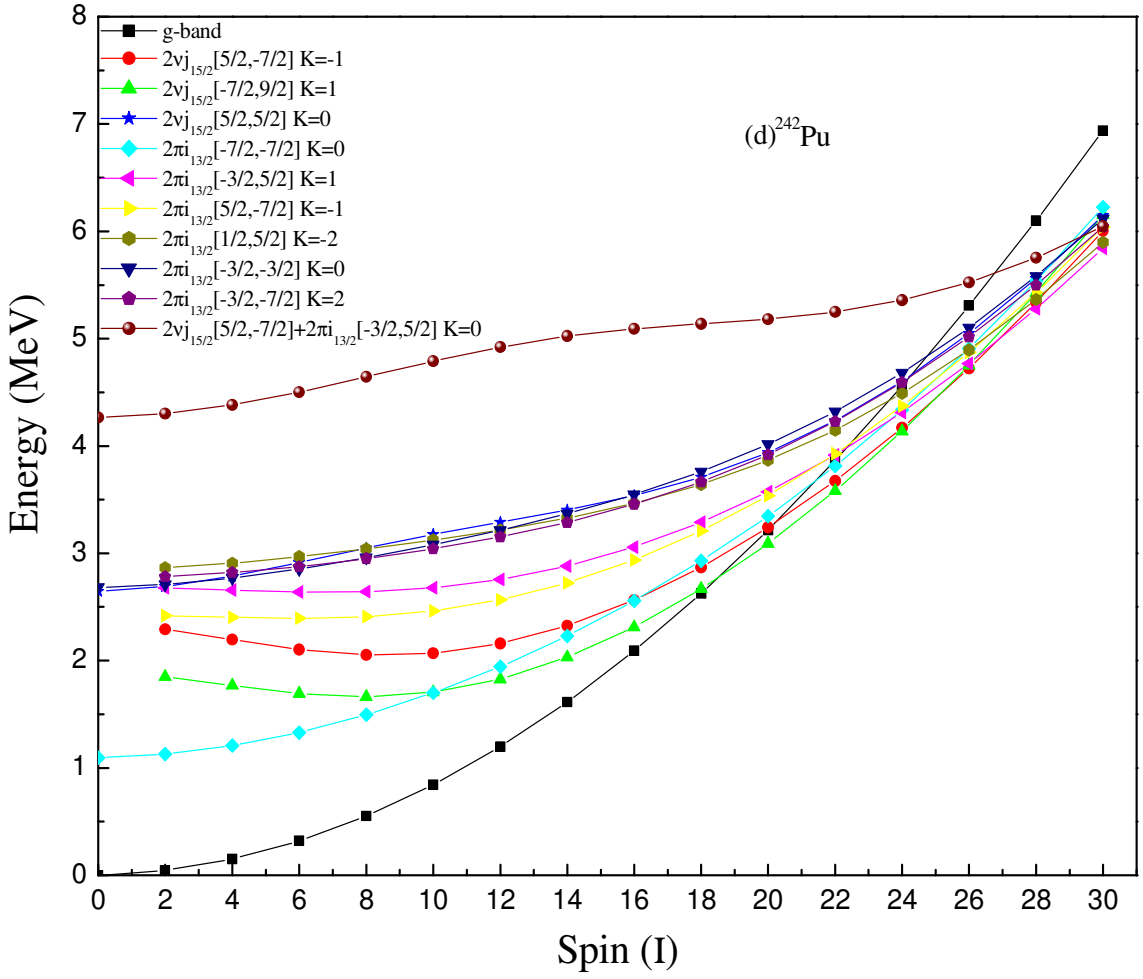

Fig. 2.4 (continued)

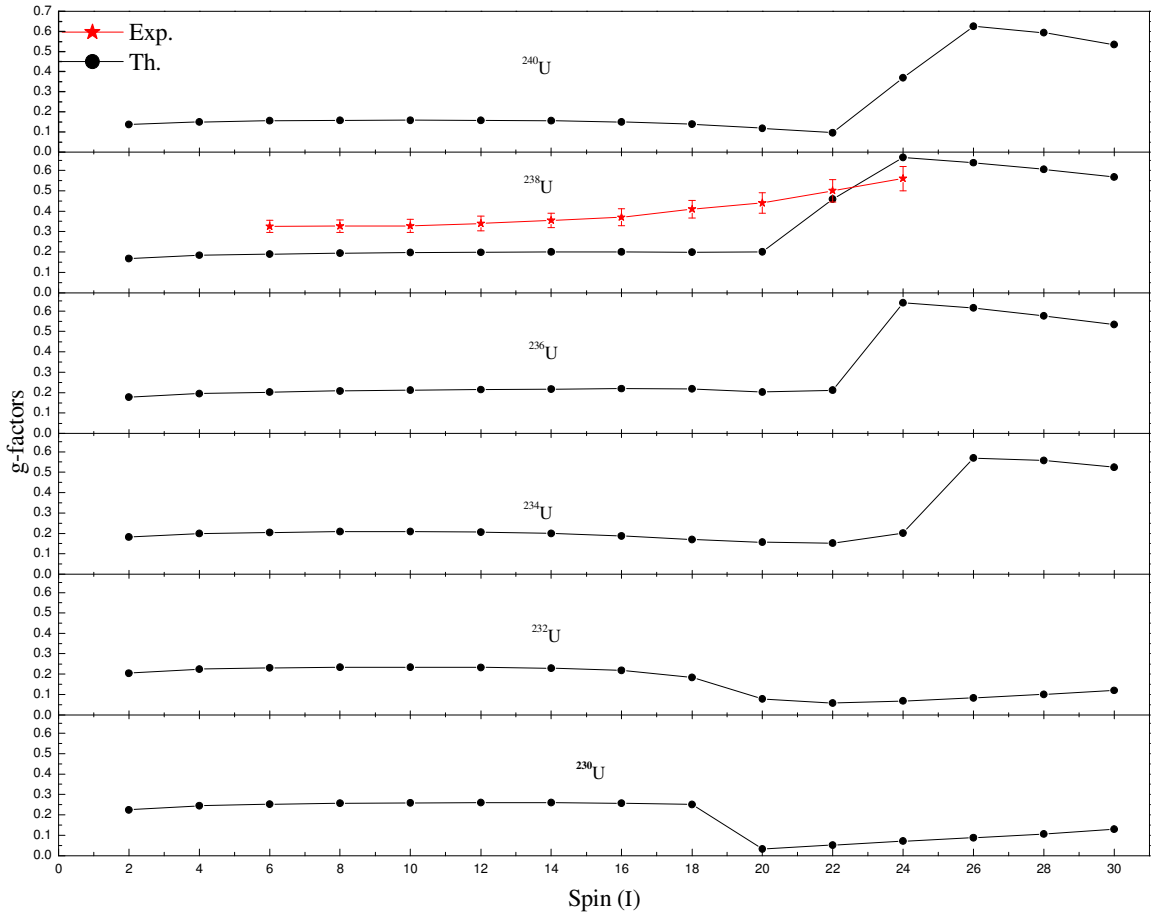

Fig. 2.5 Theoretical g-factors as a function of angular momentum for $^{230\text{-}240}$U isotopes. Comparison between calculated (Th.) and experimental (Exp.) g-factors [40] for ^{238}U is also presented.

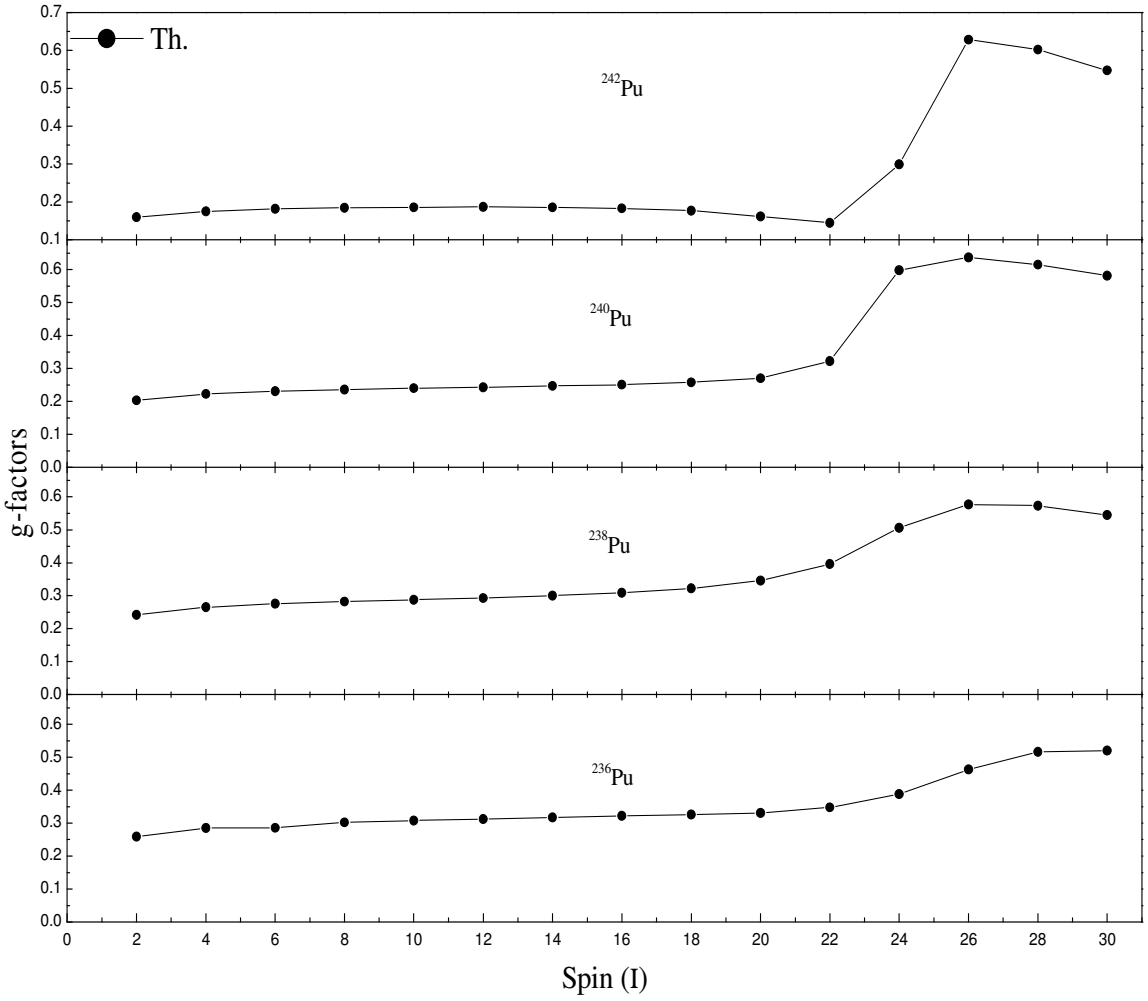

Fig. 2.6 Theoretical *g*-factors as a function of angular momentum for $^{236\text{-}242}$Pu isotopes.

Chapter 3

Projected Shell Model study of Curium isotopes

3.1 Introduction

Spectroscopic studies of low-lying states in heavy nuclei have been carried out with the objective of understanding the properties of new super heavy nuclei [30,117-125]. In this regard, spectroscopic data on nuclei with atomic number in the neighbourhood of $Z\approx96$ gives one an opportunity of carrying out systematic studies on some new features of nuclear structure [30,78]. Most of the studies have focused on collective structures in even-even nuclei [47, 48] since these are relatively easier to investigate. Information on odd-A nuclei allows for more sensitive tests of theoretical predictions of single particle energies and moments of inertia. High spin collective properties has become available on some even-even and odd-A Cm isotopes wherein, it has become possible to map energy spectra up to high spins [45,46,51,52].

Ahmad *et al*. [41] have observed the existence of the ground state rotational bands with identical transition energies up to spin $I= 8\hbar$ in ^{244}Cm and ^{246}Cm and have found that the importance of these bands is that the single particle states are well characterized at normal deformation and hence there is a better chance of understanding the underlying physics in these identical bands. Czosnyka *et al*. [45] have extracted *E2* transition matrix elements of ^{248}Cm nucleus involving the ground state band up to spin 24^+ by coulomb excitation using 641 MeV ^{136}Xe and 260 MeV ^{58}Ni projectiles. They have also measured static electric quadrupole moments up to spin 20^+. Piercey *et al*. [46] have studied ground state band of ^{248}Cm up to spin 28^+ by observing γ-rays following multiple coulomb excitation with use of ^{208}Pb ions at 5.3 MeV/u. These authors have found that a smooth, gradual increase in the effective moment of inertia is seen at lower spin with an anomalous forward bend above spin 22^+. Hota *et al*. [52] have studied ^{247}Cm through inelastic excitation and transfer reactions with radioactive targets. They have observed that the ground state band in ^{247}Cm is built on a $\nu j_{15/2}[734]9/2^-$ Nilsson configuration. Tandel *et al*. [50] have studied odd-A nuclei ^{247,249}Cm and ^{249}Cf through inelastic

excitation and transfer reactions. They have provided detailed information on high spin collective structure in ^{247}Cm and have found that ν[734]9/2$^-$ is the highest-lying neutron configuration investigated up to high spin.

Zhang *et al*. [68] have investigated rotational bands in nuclei with Z = 96 by using Cranked Shell Model (CSM) with the pairing correlations treated by particle-number conserving (PNC) method. A new set of Nilsson parameters are proposed by fitting experimental single particle spectra in nuclei with Z= 96. They have also calculated bandhead energies of the 1-qp bands in odd-A nuclei by PNC-CSM (Cranked Shell Model) method. Zhang *et al*. [69] have also investigated odd-A ^{247}Cm nucleus by using CSM with pairing correlations treated by PNC method. They have found that the experimental moments of inertia, alignments and their variations with rotational frequency ω are reproduced well by PNC-CSM calculations. Pomorski *et al*. [126] have investigated the properties of fission isomers, like moment of inertia, pairing energy and collective gyromagnetic ratios. They have also discussed the effect of some changes in the pairing interaction. Ibrahim *et al*. [127] have obtained a core cluster potential by combining the best features of a microscopic and phenomenological core cluster potential and have used it to analyze the spectra and exotic decays of heavy even-even nuclei. Adamain *et al*. [128] have studied the low-lying one quasi-particle states in the isotonic chains with N =147, 149, 151, 153 and 155 within the microscopic-macroscopic and self consistent approaches. They have also suggested alpha-decay schemes of several nuclei. Parkhomenko and Sobiczewski [70] have calculated neutron one-quasiparticle states of $^{243-247}$Cm nuclei by using macroscopic-microscopic approach. They have considered even Z and odd N nuclei with Z=96 and N=147-151. All of them are well deformed. They have found that the characteristics of the experimentally known ground states are well reproduced. Egido and Ring [66] have performed microscopic study of the yrast line in $^{242-248}$Cm. Several versions of Cranking Model have been discussed by these authors. They have found that the mean–field approach, in the form of Cranking Model in the simplified version of the Rotating Shell Model, is able to reproduce the alignment and band crossing pattern at the yrast line. Shirikova *et al*. [72] have investigated low-lying states of the nuclei with Z = 96. They have calculated excitation energies and wave functions of low lying states of the nuclei with Z = 96 by using quasi-particle phonon

model and have found that the excitation of the phonons and the quasi-particle-phonon interaction play an important role in the description of the properties of the excited states of these nuclei with $Z = 96$.

In this chapter, even-even Curium and some odd-A Curium isotopes have been studied by employing Projected Shell Model approach. The results have been obtained for yrast levels, *B(E2)* transition probabilities and *g*-factors for even-even $^{242\text{-}248}$Cm. The calculation of transition energies of yrast and excited bands of odd mass ^{243,245,247}Cm is also performed and structures of these bands are analyzed.

3.2 Theoretical Framework

The detailed description of PSM has been presented in Chapter 2 of the present thesis. The present calculations are performed by considering three major harmonic-oscillator shells with N=4, 5, 6 and N =5, 6, 7 for protons and neutrons, respectively. For all the calculations, the monopole pairing strengths G_M used in the calculation are $G_M = \left[G_1 \mp G_2 \frac{N-Z}{A}\right] A^{-1}$ with '-' for neutrons and' +' for protons. Here G_1 and G_2 values were varied to reproduce pairing gaps in even-even and even-odd Cm isotopes on an average basis. The values that reproduce the pairing gaps are taken as 20.12 and 13.13 MeV respectively for even-even $^{242\text{-}248}$Cm, and 18.52 and 13.13 MeV for odd-N $^{243\text{-}247}$Cm isotopes. These strengths are nearly the same as used in Refs. [129,130]. The quadrupole-pairing strength G_Q is assumed to be proportional to G_M, with the proportionality constant being fixed to be 0.18 for ^{242}Cm, 0.16 for $^{244\text{-}248}$Cm and 0.14 for $^{243\text{-}247}$Cm.

3.3 Results and discussion for even-even $^{242\text{-}248}$Cm isotopes

3.3.1 *Yrast Spectra*

The theoretical calculations for $^{242\text{-}248}$Cm have been performed by carrying out PSM calculations using the deformation parameters which are presented in Table 3.1. The quadrupole deformation parameter ε_2 was varied around the experimental [106] value to reproduce $E_{2_1}^{+}$ energy values. The quadrupole deformation parameters were adjusted so that the energy gap between the $E_{2_1}^{+}$ and ground state for the $^{242\text{-}248}$Cm

isotopes are reproduced. The experimental level scheme of positive parity yrast bands of $^{242\text{-}248}$Cm [131-134] are available up to spins 26^+, 8^+, 26^+ and 30^+ respectively. In Fig. 3.1, the theoretical yrast spectra are compared with the experimental data for $^{242\text{-}248}$Cm. It is observed from the figure that the yrast spectra for ^{242,246,248}Cm are reasonably well reproduced for spins $\leq 18^+$ and for ^{244}Cm, up to spin 8^+ only. The disagreement between the observed and calculated values occurs as one goes to the higher spins. The maximum difference between the experimental and calculated values of energy for the highest known spins are 0.34, 0.02, 0.57 and 1.04 MeV for $^{242\text{-}248}$Cm, respectively. In Fig. 3.2, transition energies [E(I) - E(I-2)] are compared with the experimental data. It is seen from the figure that the calculated transition energies reproduce the experimental data upto spin 18^+. However, at higher spin the theoretical transition energies are higher than experimental ones. The reason for this discrepancy could be the assumption of fixed pairing used throughout the band spectra for all nuclei.

3.3.2 Structure of yrast bands of even-even $^{242\text{-}248}$Cm

In Figure 3[3 (a) - 3(d)], the band diagrams are presented for $^{242\text{-}248}$Cm. From these figures, it is observed that the yrast states in $^{242\text{-}248}$Cm do not arise from a single intrinsic state. The yrast states up to certain spin arise from zero quasi particle (0-qp) intrinsic state. After that spin, higher angular momentum states are found to arise from different intrinsic states and have a composite structure. They are predicted to arise from two or more than two intrinsic states. The details are described isotope-wise here under:

Fig. 3.3 (a) represents the band diagram of ^{242}Cm, which indicates that the yrast states up to spin I=18^+ are seen to arise from 0-qp intrinsic state. Between spins 20^+ to 24^+, the ground state band (g-band) is crossed by four 2-qp neutron and two 2-qp proton bands having configurations $2\nu j_{15/2}(1/2,-3/2)$ K=-1, $2\nu j_{15/2}(1/2,-3/2)$ K=0, $2\nu j_{15/2}(-3/2,-3/2)$ K=0, $2\nu[j_{15/2}(-3/2)+ j_{13/2}(1/2)]$ K=-2, $2\pi i_{13/2}(1/2,-3/2)$ K=-1 and $2\pi i_{13/2}(1/2,1/2)$ K=0, respectively. Thus, the yrast band from spins I =20^+ to 26^+ arises from the contribution of 2-qp proton and neutron bands. At spin 28^+ one 4-qp band having configuration $2\nu j_{15/2}(1/2,-3/2) + 2\pi i_{13/2}(1/2, 1/2)$ K=-1 crosses the above mentioned 2-qp proton and neutron bands. Thus, the yrast band for spins $I \geq 28^+$ arise from the 4-qp band in addition to 2-qp proton and neutron bands.

Fig. 3.3(b) represents the band diagram of ^{244}Cm. In this nucleus, the yrast states up to spin I=16^{+} are seen to arise from the 0-qp intrinsic state. At spin 18^{+}, the ground state band is crossed by one 2-qp neutron and one 2-qp proton bands having configurations $2\nu j_{15/2}(-3/2,-3/2)$ K=0 and $2\pi i_{13/2}(1/2, 1/2)$ K=0, respectively. Between spins 20^{+} to 26^{+}, the ground state band is crossed by two 2-qp neutron and one 2-qp proton bands having configurations $2\nu j_{15/2}(1/2,-3/2)$ K=-1, $2\nu[j_{15/2}(-3/2)+ j_{13/2}(1/2)]$ K=-2 and $2\pi i_{13/2}(1/2,-3/2)$ K=-1, respectively. Thus, the yrast band from spins I = 20^{+} to 26^{+} arises from the contribution of three 2-qp neutron and two 2-qp proton bands. At higher spins I $\geq$ 28^{+}, in addition to 2-qp neutron and proton bands, one 4-qp band having configuration $2\nu j_{15/2}(1/2,-3/2)+2\pi i_{13/2}(1/2,1/2)$ K=-1 also contributes to the yrast band.

Fig. 3.3(c) represents band diagram of ^{246}Cm, wherein, the yrast states up to spin I=12^{+} are seen to arise from the 0-qp intrinsic state. Between spins 14^{+} to 16^{+}, the ground state band is crossed by one 2-qp neutron and one 2-qp proton bands having configurations $2\nu j_{13/2}(1/2, 1/2)$ K=0 and $2\pi i_{13/2}(1/2, 1/2)$ K=0, respectively. Above spin 18^{+}, the ground state band is crossed by two 2-qp neutron and one 2-qp proton bands having configurations $2\nu[j_{15/2}(-3/2) +j_{13/2}(1/2)]$ K=-1, $2\nu[j_{15/2}(-3/2)+ j_{13/2}(1/2)]$ K=-2 and $2\pi i_{13/2}(1/2,-3/2)$ K=-1, respectively. Thus, the yrast band from spins 16^{+} to 20^{+} arise from the contribution of one 2-qp neutron and one 2-qp proton bands. Above spin 20^{+}, the yrast band arises from the superposition of three 2-qp neutron and two 2-qp protons bands. At spin I $\geq$ 26^{+}, one 4-qp band having configuration $2\nu j_{15/2}(1/2,3/2)+2\pi i_{13/2}(1/2,1/2)$ K=-1 is also seen to contribute to the yrast band in addition to three 2-qp neutron and two 2-qp proton bands.

Fig. 3.3(d) represents the band diagram of ^{248}Cm. In case of ^{248}Cm, the yrast states up to spin I=8^{+} are seen to arise from the 0-qp intrinsic state. At spin 10^{+}, one 2-qp neutron band having configuration $2\nu j_{13/2}(1/2, 1/2)$ K=0 crosses the ground state band and becomes lowest in energy. Thus, the yrast band from spins 10^{+} to 20^{+} arises from the one 2-qp neutron band. However, at higher spins with I $\geq$ 22^{+}, multiple 2-qp neutron and proton bands are seen to contribute to the yrast band.

3.3.3 Electromagnetic quantities

3.3.3.1 *B(E2) transition probabilities*

B(E2) transition probabilities can give important information on the nuclear structure and provide stringent test of a particular model and are defined by eq. (2.52) of chapter 2 of the present thesis. In the calculation, the effective charge for neutrons $e_{\nu}^{eff} = 0.55e$ and for protons $e_{\pi}^{eff} = 1.55e$ has been taken.

In Table 3.2, the comparison of experimental *B(E2)* transition probabilities have been made with the theoretically calculated values. The experimental data for the $2_1^+ \rightarrow 0_1^+$ transitions are taken from Ref. [135]. From this table, it is seen that the PSM calculations reproduce the experimental values of $2_1^+ \rightarrow 0_1^+$ transition for $^{244\text{-}248}$Cm. In case of ^{248}Cm, the experimental data is available up to spin 24^+ [45]. Experimentally, the dip in the *B(E2)* values of ^{248}Cm is observed at spin 10^+. The calculated *B(E2)* values reproduce the increasing trend of the observed *B(E2)* values upto spin 8^+. The calculated values show a small increase with spin for higher transitions upto spin 24^+.

3.3.3.2 *g-factors*

The g-factors are defined by eq. (2.53) of chapter 2 of present thesis. In Fig 3.4 the total g-factors and the contribution of the protons (g_p) and neutrons (g_n) to the total g-factors are plotted as a function of the spin (I). In all Cm isotopes the contribution of neutrons (g_n) decreases and contribution of protons (g_p) increases. From the figure, it is seen that the theoretical total *g*-factors show an increasing trend in all Cm isotopes. The total contribution of g-factors is due to g_p and that may be due to alignment of protons. The *g*-factors can be understood from the analysis of the band diagrams, where it is seen that energy states up to spins 18^+, 16^+, 12^+ and 8^+ in $^{242\text{-}248}$Cm, respectively, arise from zero quasi-particle configuration. Therefore g-factors are not showing much variation. Above spins 18^+, 16^+, 12^+ and 8^+ in $^{242\text{-}248}$Cm isotopes, respectively, the yrast band arises from 2-qp neutron and 2-qp proton bands. The theoretical *g*-factors show an increasing trend in all Curium isotopes. For example, in case of ^{242}Cm, the theoretical *g*-factor has a value 0.2653 at spin 18^+, whereas at 30^+, the value shows an increase to 0.3114. Similar

trend is obtained for $^{244-248}$Cm isotopes. The small increase in the *g*-factors at higher spin in all Cm isotopes is due to crossing of *g*-band by 2-qp proton bands. The experimental values of g-factors in $^{242-248}$Cm isotopes are not available so one cannot make any comment regarding the level of agreement.

3.4 Results and discussion for odd mass $^{243-247}$Cm isotopes

3.4.1 ^{243}Cm

In Fig. 3.5, the experimental and theoretical excitation energy spectra of the two positive parity bands of ^{243}Cm are compared. For ^{243}Cm, the experimental values of energies of the ground state band [136] (g-band) are known up to spin $13/2^+$ and that of excited band [136] up to spin $11/2^+$. The band having configuration $1\nu i_{11/2}(5/2)$ K=5/2 is the ground state band and $1\nu 2g_{9/2}(-7/2)$ K=-7/2 is the lowest excited band. The results obtained indicate that reasonably good agreement is obtained. The difference between the calculated and experimental value of energies for the highest known spin are 0.02 MeV in g-band and 0.04 MeV in the excited band. The band diagram for ^{243}Cm is displayed in Fig. 3.6. From this diagram, it is observed that $1\nu i_{11/2}(5/2)$ K=5/2 band is the lowest in energy and is in agreement with the configuration $\nu 5/2^+$ [622] assigned by the authors of Ref. [51]. In Fig. 3.7, transition energies [E(I) - E(I-1)] are compared with the experimental data. From this figure, it is seen that the theoretical transition energies are in agreement with the available experimental data.

3.4.2 ^{245}Cm

Fig. 3.8 displays the comparison of calculated and experimental excitation energy of the two positive parity bands of ^{245}Cm. The band having configuration $1\nu 2g_{9/2}(-7/2)$ K=-7/2 is the ground state band and $1\nu i_{11/2}(5/2)$ K=5/2 is the lowest excited band. Experimental data is taken from Ref. [137]. From Fig. 3.8, it is seen that the available experimental energy levels are well reproduced. The difference between the calculated and experimental value of energies for the highest known spin are 0.005 MeV in g-band and 0.12MeV in the excited band. The band diagram for ^{245}Cm is displayed in Fig. 3.9. From Fig. 3.9, it is observed that $1\nu 2g_{9/2}(-7/2)$ K=-7/2 band is the lowest in

energy and is in agreement with the configuration $\nu 7/2^+$ [624] assigned by the authors of Ref. [51]. Thus, the yrast band is seen to arise from the 1-qp band having configuration $1\nu 2g_{9/2}(-7/2)$ K=-7/2 up to spin I= $51/2^-$. In Fig. 3.10, transition energies [E(I) - E(I-1)] are compared with the experimental data. From this figure, it is seen that the theoretical transition energies reproduce the available experimental data qualitatively.

3.4.3 ^{247}Cm

The experimental level scheme in Refs. [50, 138] shows that the negative parity band is the g-band in ^{247}Cm having configuration $1\nu j_{15/2}(9/2)$ K=9/2. The comparison of calculated energy levels for this negative parity band with the experimental data is presented in Fig. 3.11. In the same figure we have also presented the lowest excited negative parity band energies having configuration $1\nu 2h_{11/2}(1/2)$ K=1/2. This band has two signature partners $\alpha=\pm 1/2$. The band having signature $\alpha=-1/2$ is the lowest excited band. There is no experimental data available so, we cannot compare their energy levels. The experimental energies are known up to spin $51/2^-$ in g-band, which are well reproduced by the present calculations. The difference between the calculated and experimental value of energies for the highest known spin is 0.25 MeV in g-band. The band diagram for ^{247}Cm is displayed in Fig. 3.12. From Fig. 3.12, it is observed that $1\nu j_{15/2}(9/2)$ K=9/2 band is the lowest in energy and is in agreement with the configuration $\nu 9/2^+$ [734] assigned by the authors of Ref. [50]. A careful examination of Fig. 3.12 shows that the yrast states up to spin $51/2^-$ are seen to arise from the 1-qp neutron band with configuration $1\nu j_{15/2}[9/2]$ K=9/2. In Fig. 3.13, transition energies [E(I) - E(I-2)] are compared with the experimental data. From this figure, it is seen that the theoretical energies reproduce the available experimental data on the ground state band qualitatively.

3.5 Summary

From the PSM study of Curium isotopes, the following broad conclusion can be drawn.

i. The PSM calculation reproduces the available experimental data of yrast bands of even-even $^{242\text{-}248}$Cm.

ii. The study of the structure of the yrast bands of $^{242\text{-}248}$Cm from band diagrams reveals that in the low spin region, the yrast states arise from 0-qp configuration. However, at the higher spin, the yrast bands have multi-quasiparticle structure.

iii. The calculated B(E2) values for $2_1^+ \rightarrow 0_1^+$ transition reproduce the available experimental values for $^{244\text{-}248}$Cm.

iv. In case of ^{248}Cm the experimental B(E2) values for higher transitions are available upto spin 24^+ which are reproduced by the present calculation. The present calculation has predicted the B(E2) values for higher transitions for $^{242\text{-}246}$Cm isotopes.

v. The calculated values of g-factors show an increasing trend with spin in all $^{242\text{-}248}$Cm isotopes. The small increase reflected in the g-factors at higher spins in all these isotopes is due to the crossing of g-band by 2qp proton bands. The experimental values of g-factors of these isotopes are not known, so it is not possible to make a comment regarding the level of agreement.

vi. The theoretical values obtained for the level energies of ground state bands in $^{243\text{-}247}$Cm and lowest excited state bands in ^{243,245}Cm reproduces the available experimental data qualitatively. For ^{247}Cm, the lowest excited state negative parity band has been predicted.

vii. The calculated value of transition energies of the ground state bands of odd $^{243\text{-}247}$Cm reproduces the available experimental data qualitatively.

Table 3.1 Quadrupole and hexadecapole deformation parameters used in the present calculations for $^{242\text{-}248}$Cm isotopes.

Nucleus	**^{242}Cm**	**^{243}Cm**	**^{244}Cm**	**^{245}Cm**	**^{246}Cm**	**^{247}Cm**	**^{248}Cm**
ε_2	0.260	0.255	0.260	0.255	0.260	0.255	0.260
ε_4	0.010	0.003	0.018	0.003	0.033	0.003	0.040

Table 3.2 Comparison of calculated (Th.) and experimental (Exp.) *B(E2)* reduced transition probabilities (in units of e^2b^2) for $^{242\text{-}248}$Cm isotopes. Experimental data are taken from Refs. [45,135]

Transition	**^{242}Cm**		**^{244}Cm**		**^{246}Cm**		**^{248}Cm**	
$(I_i^+ \longrightarrow I_f^+)$	**Exp.**	**Th.**	**Exp.**	**Th.**	**Exp.**	**Th.**	**Exp.**	**Th.**
$2 \longrightarrow 0$	-	3.136	2.916±0.038	3.095	2.988±0.038	2.888	$2.74^{+0.002}_{-0.003}$	2.861
$4 \longrightarrow 2$	-	4.490	-	4.429	-	4.131	$3.58^{+0.064}_{-0.021}$	4.091
$6 \longrightarrow 4$	-	4.964	-	4.893	-	4.560	$5.07^{+0.06}_{-0.086}$	4.515
$8 \longrightarrow 6$	-	5.222	-	5.143	-	4.788	$5.95^{+0.021}_{-0.019}$	4.740
$10 \longrightarrow 8$	-	5.398	-	5.310	-	4.936	$3.87^{+0.30}_{-0.037}$	4.885
$12 \longrightarrow 10$	-	5.533	-	5.437	-	5.046	$4.83^{+0.005}_{-0.012}$	4.992
$14 \longrightarrow 12$	-	5.646	-	5.541	-	5.134	$6.21^{+0.016}_{-0.002}$	5.077
$16 \longrightarrow 14$	-	5.744	-	5.632	-	5.209	$4.51^{+0.007}_{-0.004}$	5.141
$18 \longrightarrow 16$	-	5.825	-	5.706	-	5.246	$4.65^{+0.011}_{-0.037}$	5.152
$20 \longrightarrow 18$	-	5.867	-	5.753	-	5.242	$4.78^{+0.035}_{-0.041}$	5.243
$22 \longrightarrow 20$	-	5.862	-	5.764	-	5.343	$6.27^{+0.064}_{-0.018}$	5.269
$24 \longrightarrow 22$	-	5.964	-	5.853	-	5.383	$5.97^{+0.78}_{-1.881}$	5.290
$26 \longrightarrow 24$	-	5.987	-	5.888	-	5.359	-	5.312
$28 \longrightarrow 26$	-	5.762	-	5.734	-	5.333	-	5.288
$30 \longrightarrow 28$	-	5.502	-	5.639	-	5.312	-	5.254

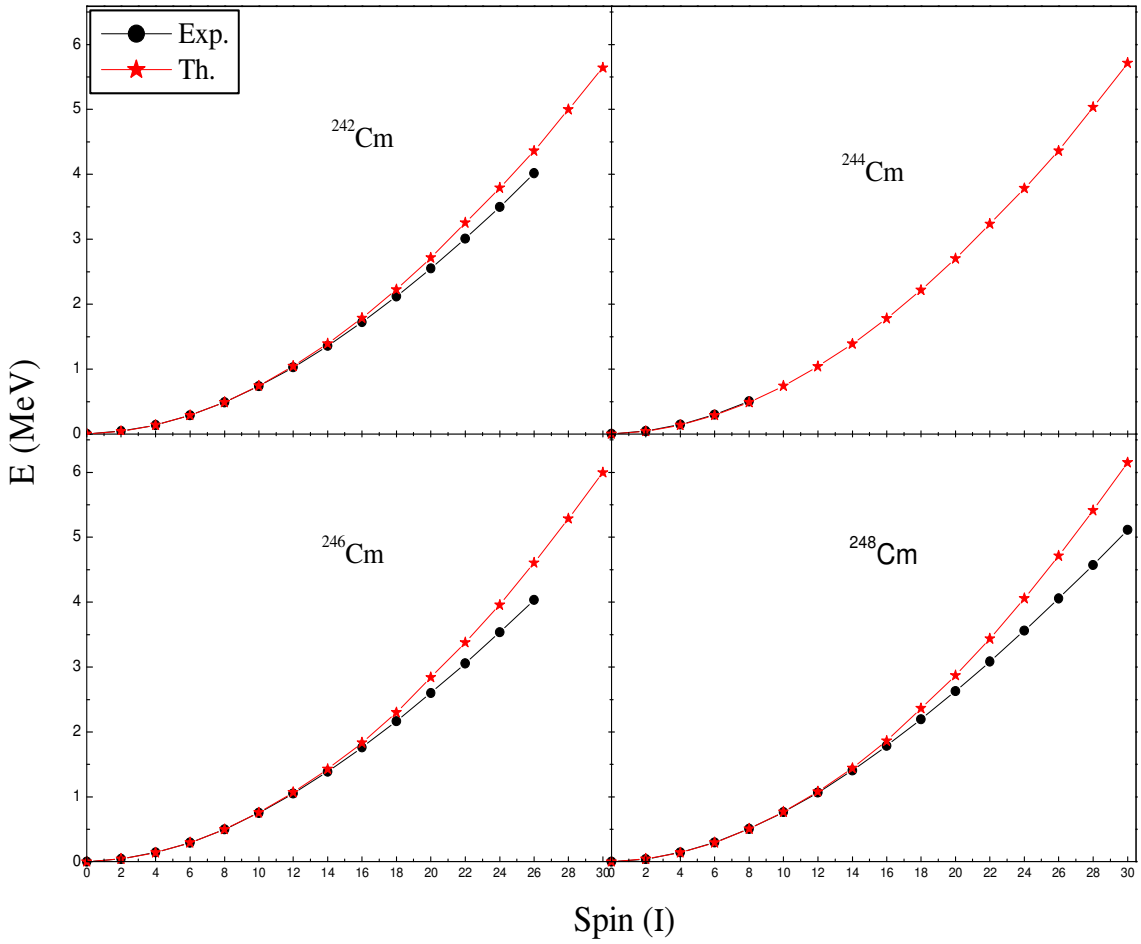

Fig. 3.1 Comparison of calculated (Th.) and experimental (Exp.) positive-parity yrast bands of $^{242\text{-}248}$Cm isotopes. The experimental data is taken from Refs. [131-134].

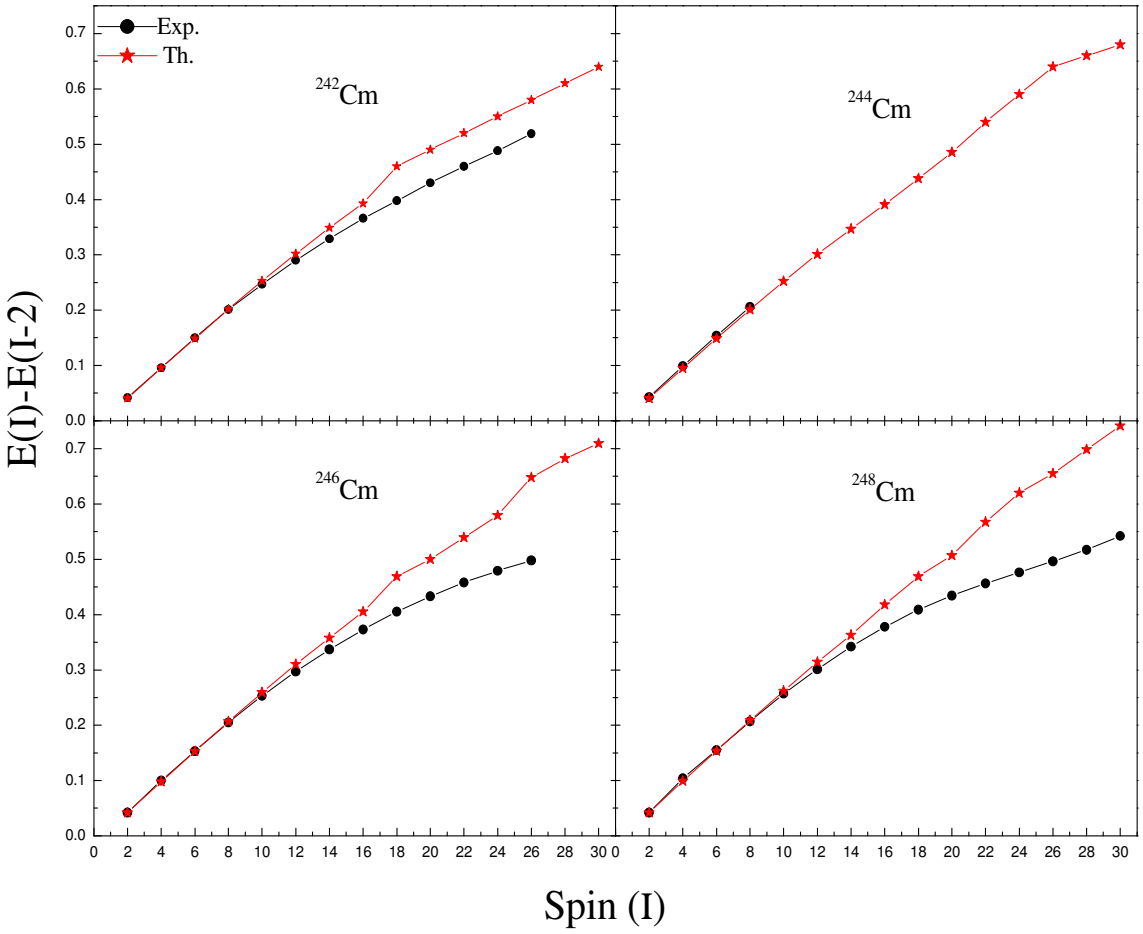

Fig. 3.2 Comparison of calculated (Th.) and experimental (Exp) transition energies [E(I)-E(I-2)] versus spin for even-even $^{242\text{-}248}$Cm isotopes. Exp. data taken from Refs. [131-134].

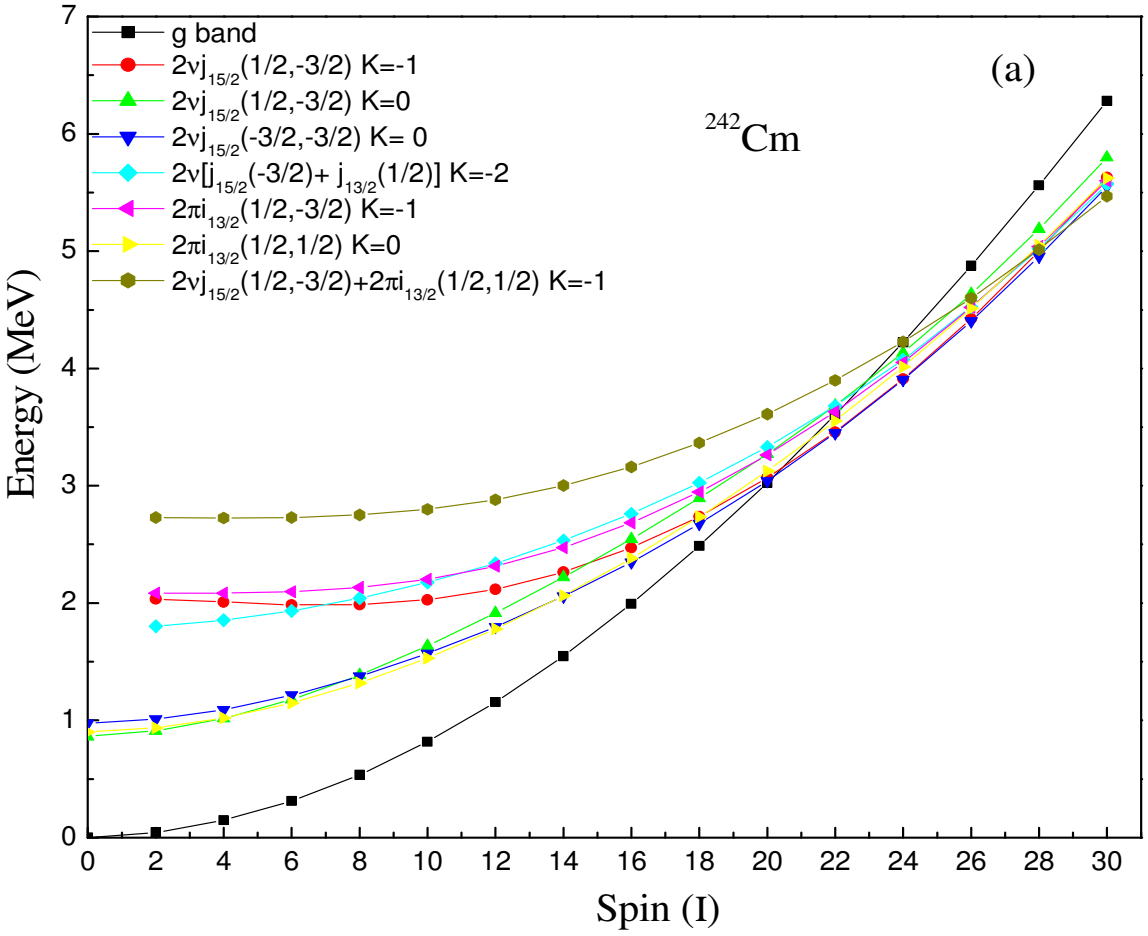

Fig. 3.3 Band diagrams for (a) ^{242}Cm, (b) ^{244}Cm, (c) ^{246}Cm and (d) ^{248}Cm isotopes.

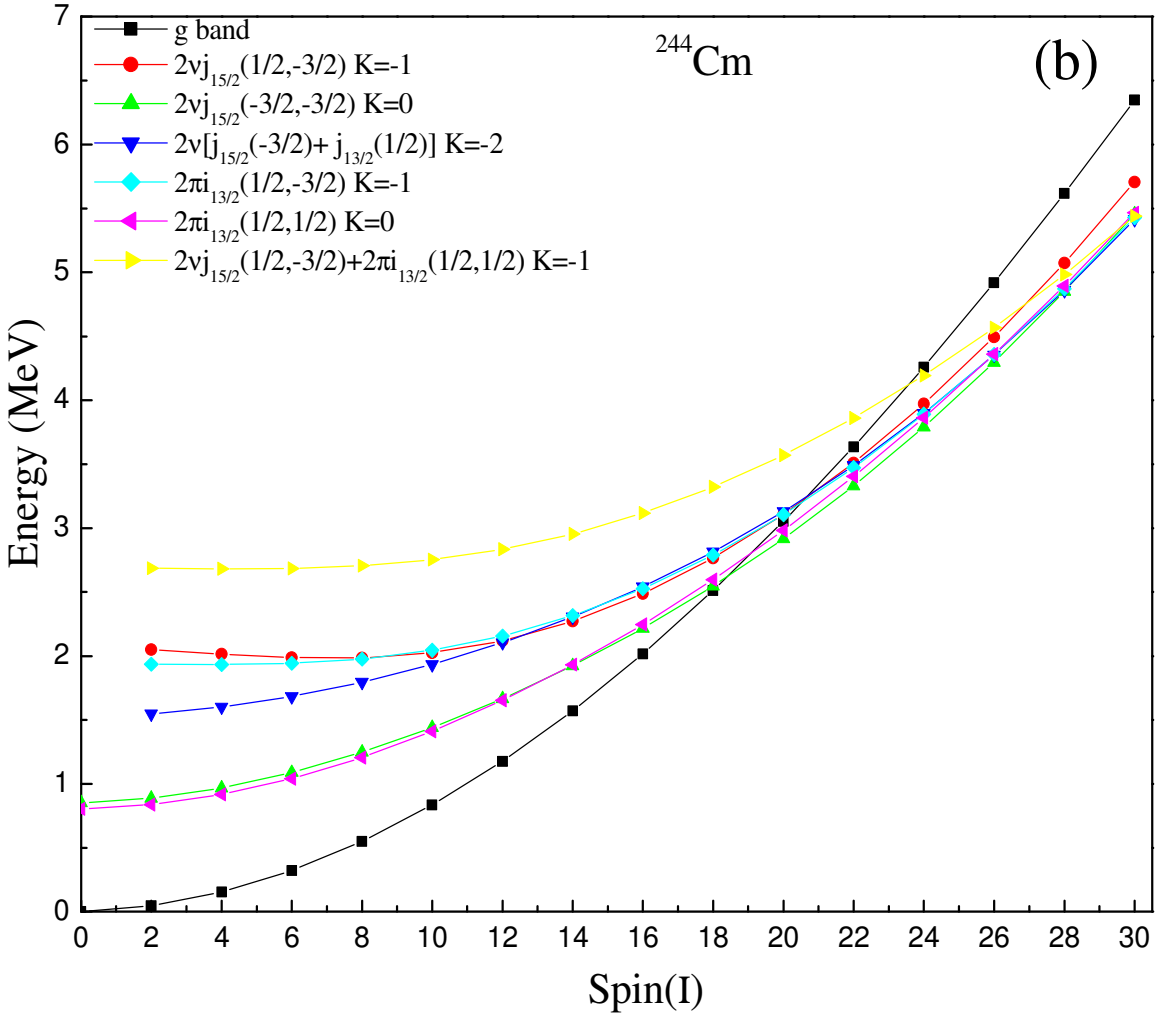

Fig. 3.3 (continued)

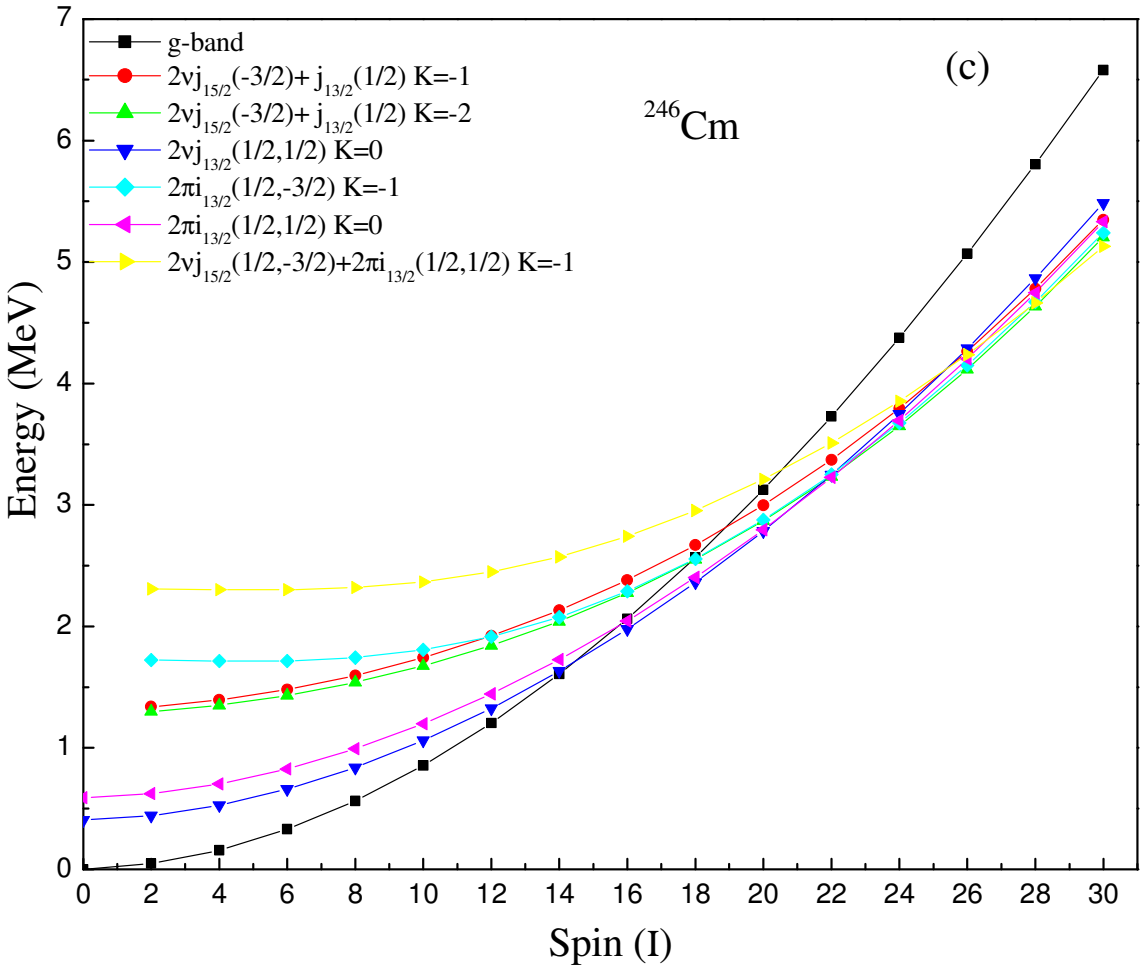

Fig. 3.3 (continued)

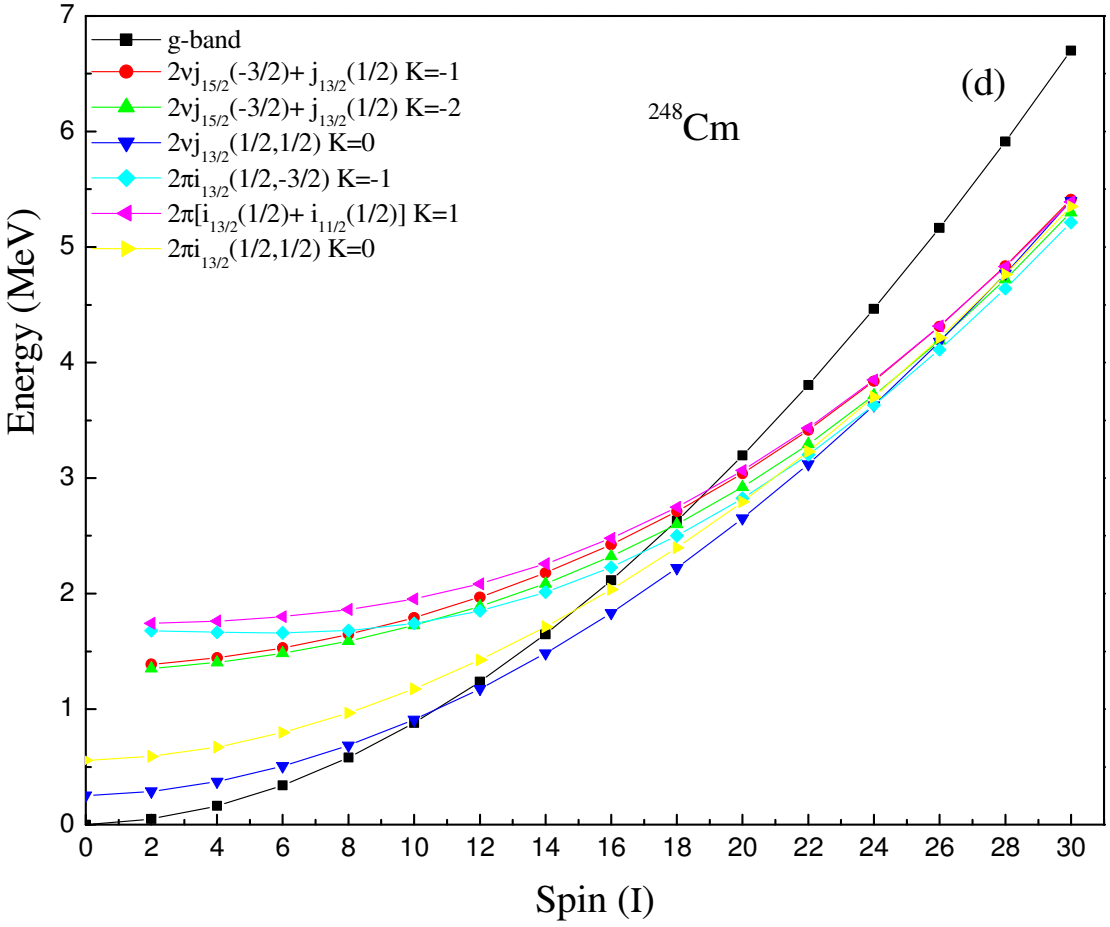

Fig. 3.3 (continued)

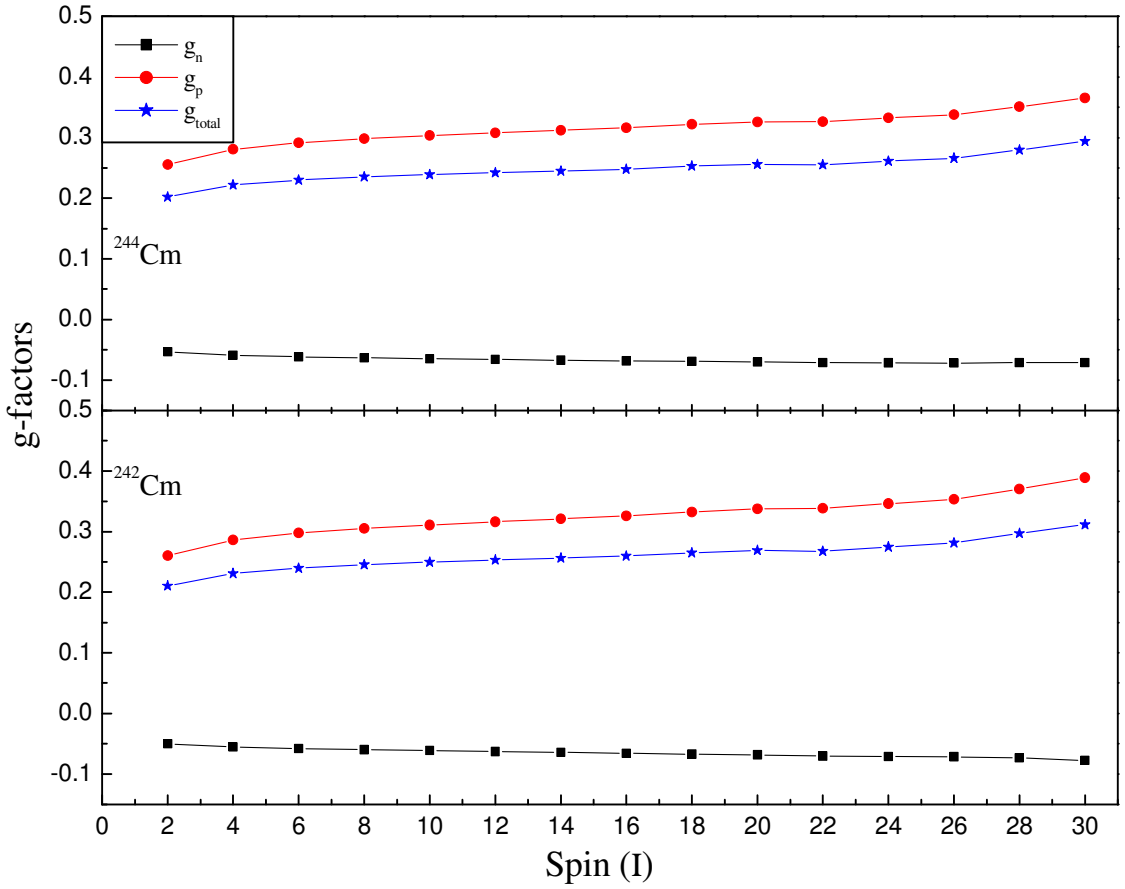

Fig. 3.4 Theoretical g-factors as a function of angular momentum for $^{242\text{-}248}$Cm isotopes.

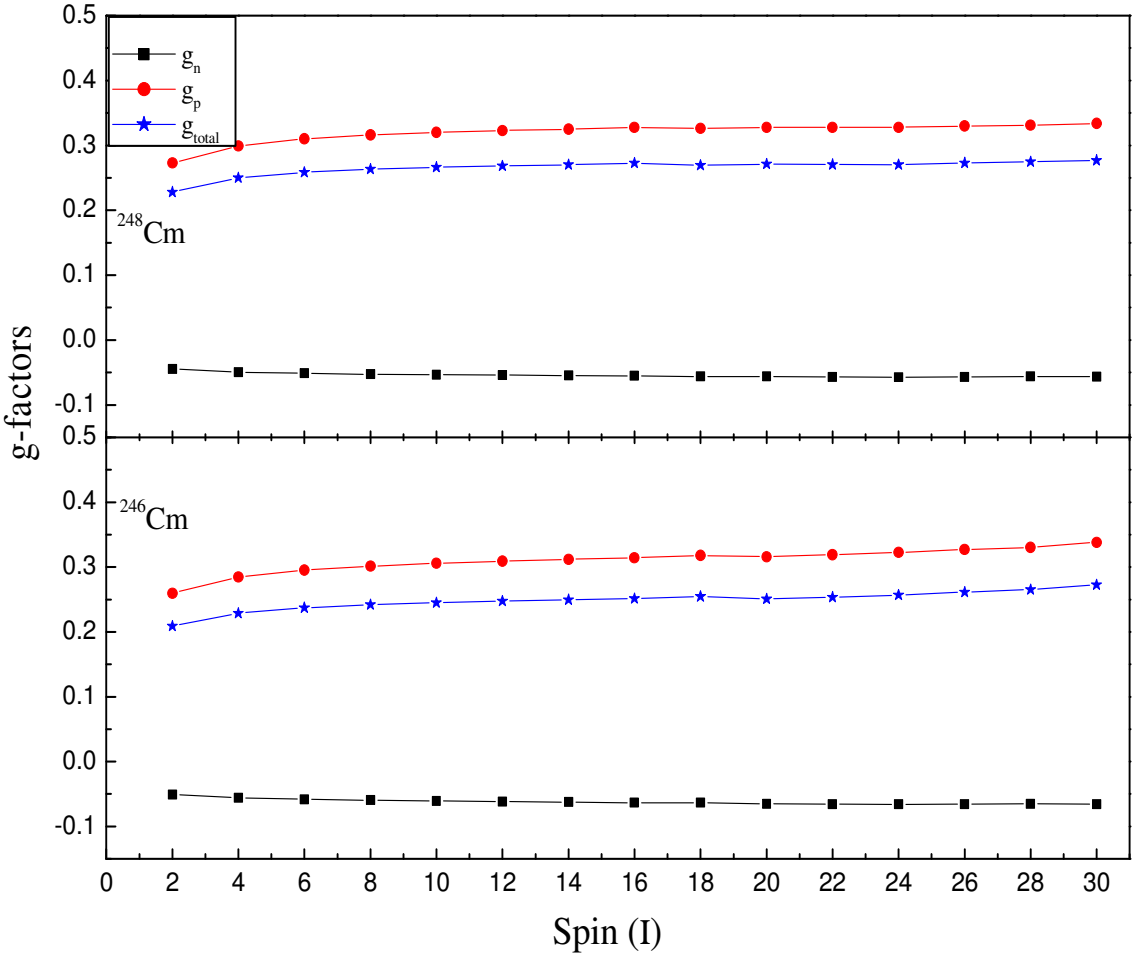

Fig. 3.4 (continued)

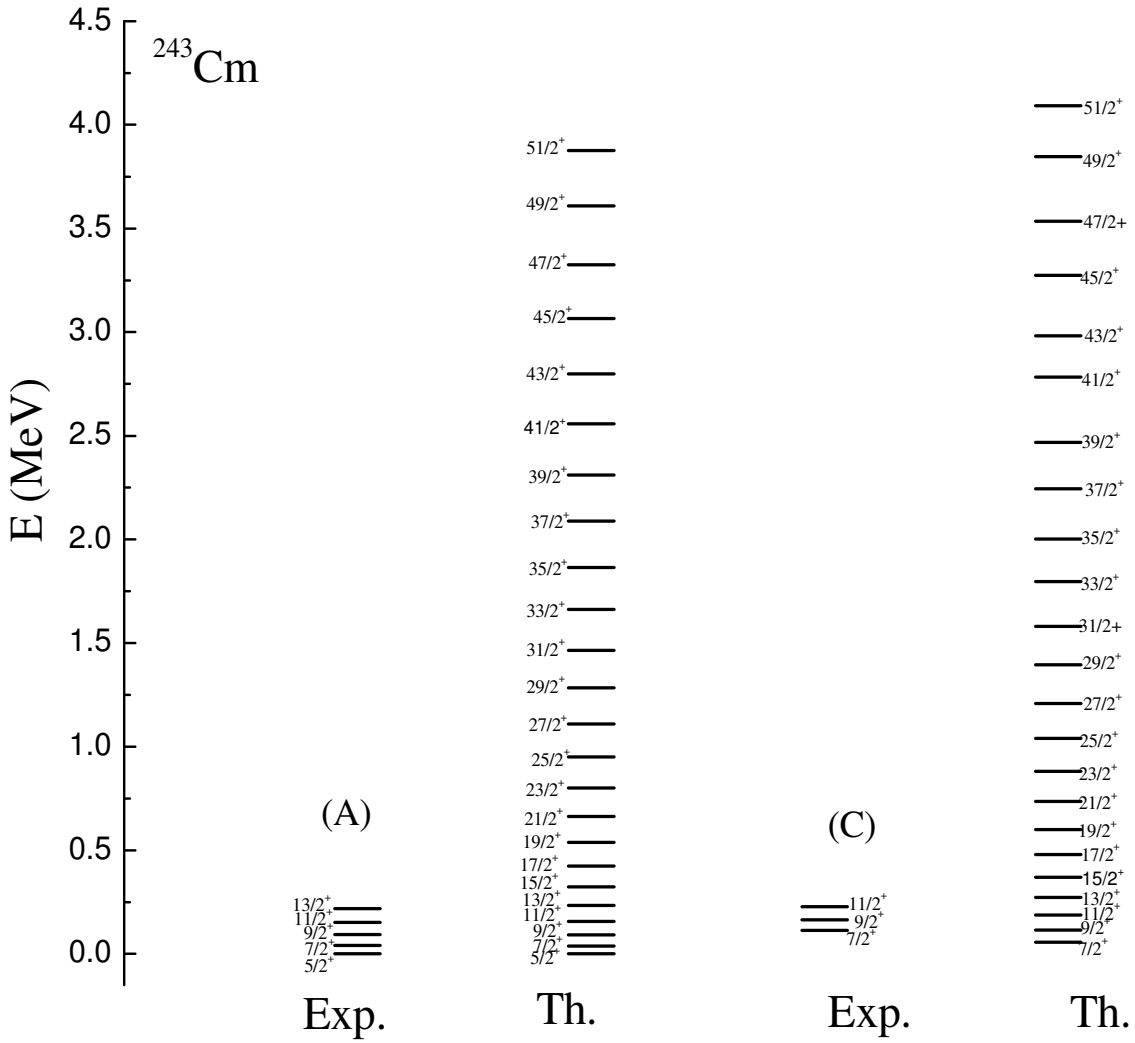

Fig. 3.5 Comparison of calculated (Th.) and experimental (Exp.) energy levels for ground state band (A) [136] and excited band (C) [136] of positive-parity of ^{243}Cm. The experimental data is taken from Ref. [136].

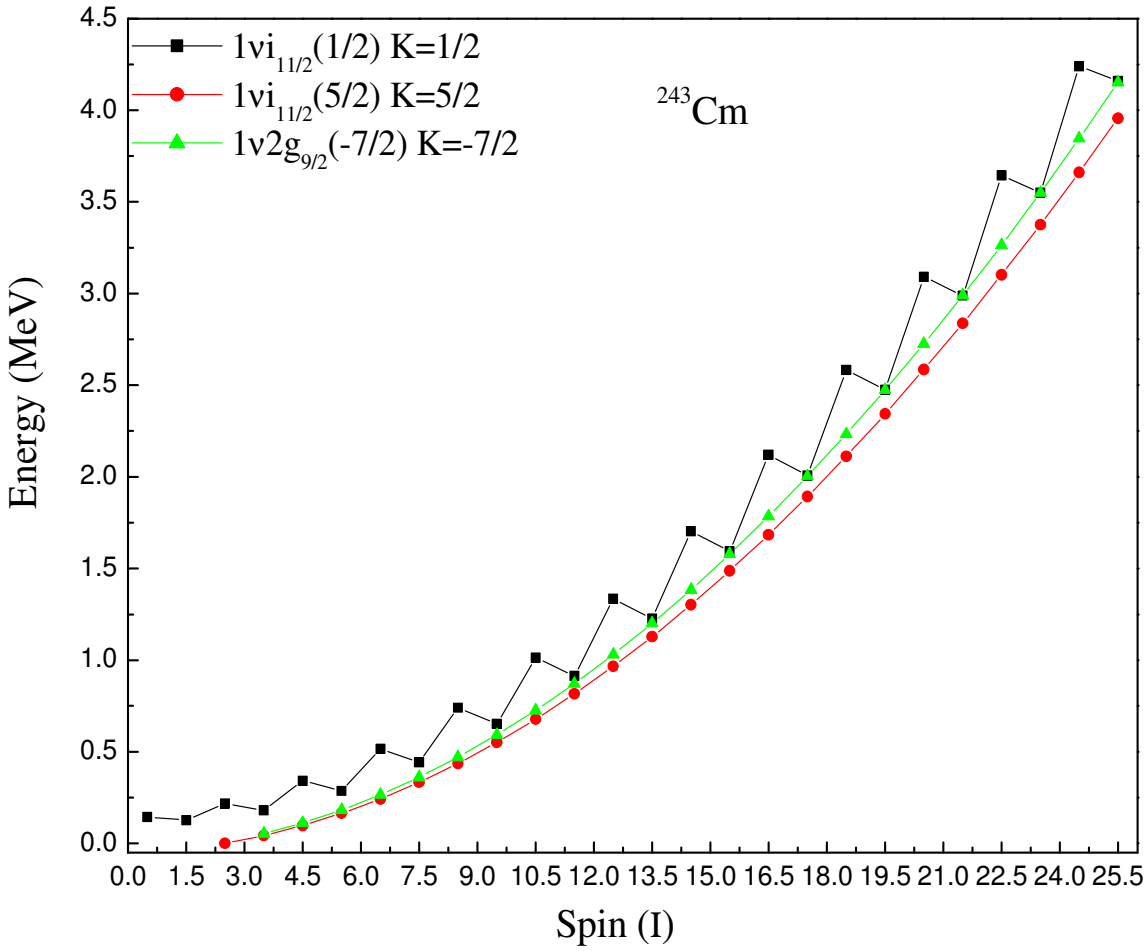

Fig. 3.6 Band diagram for ^{243}Cm.

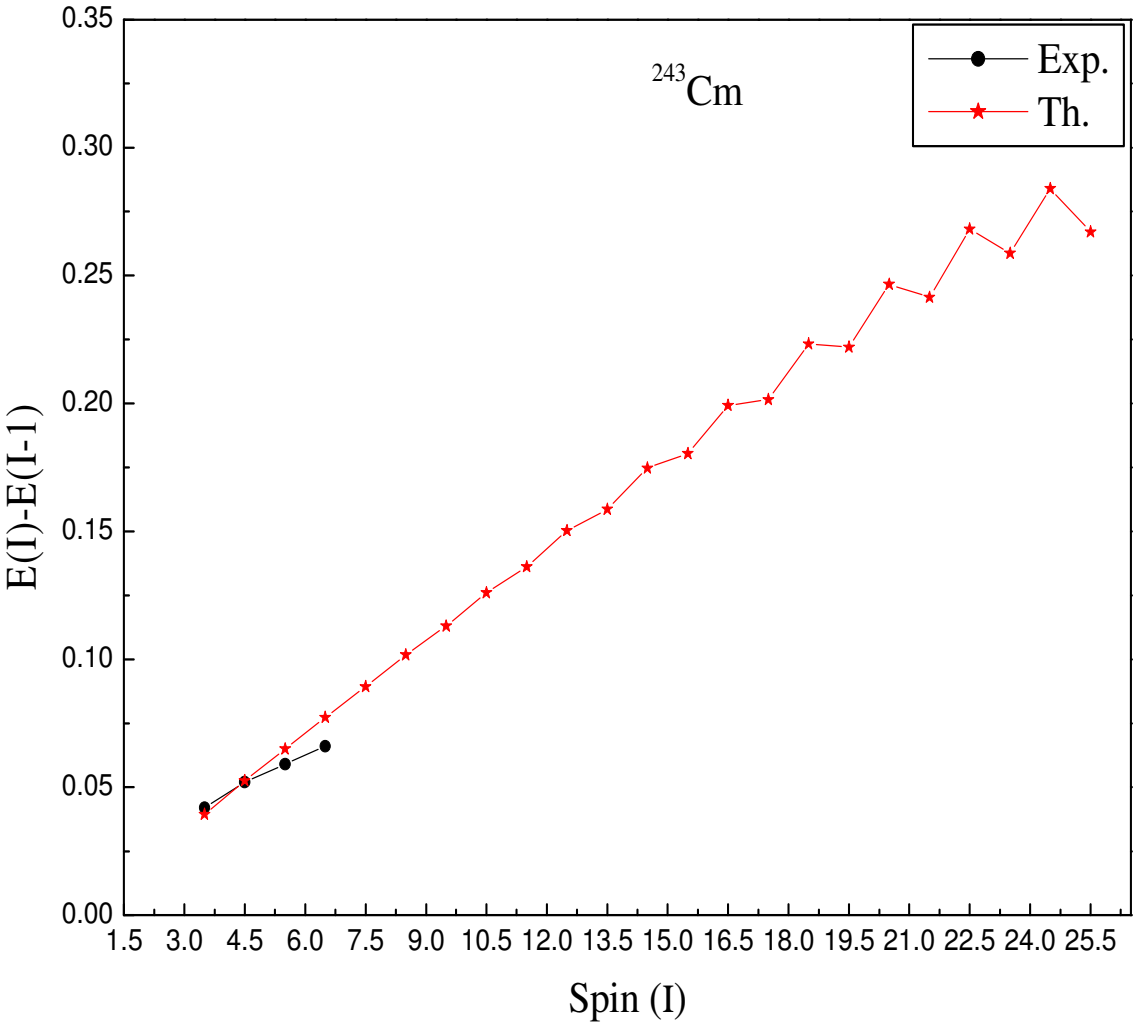

Fig. 3.7 Comparison of calculated (Th.) and experimental (Exp) transition energies [E(I)-E(I-1)] versus spin for ^{243}Cm.

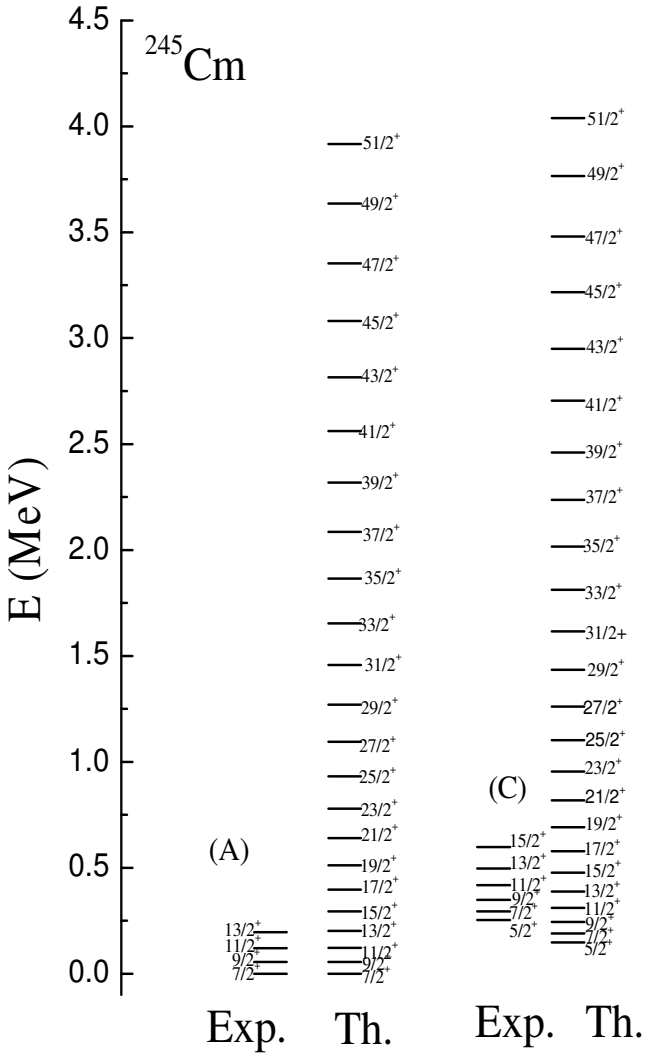

Fig. 3.8 Comparison of calculated (Th.) and experimental (Exp.) energy levels for ground state band (A) [137] and excited band (C) [137] of positive-parity of ^{245}Cm. The experimental data is taken from Ref. [137].

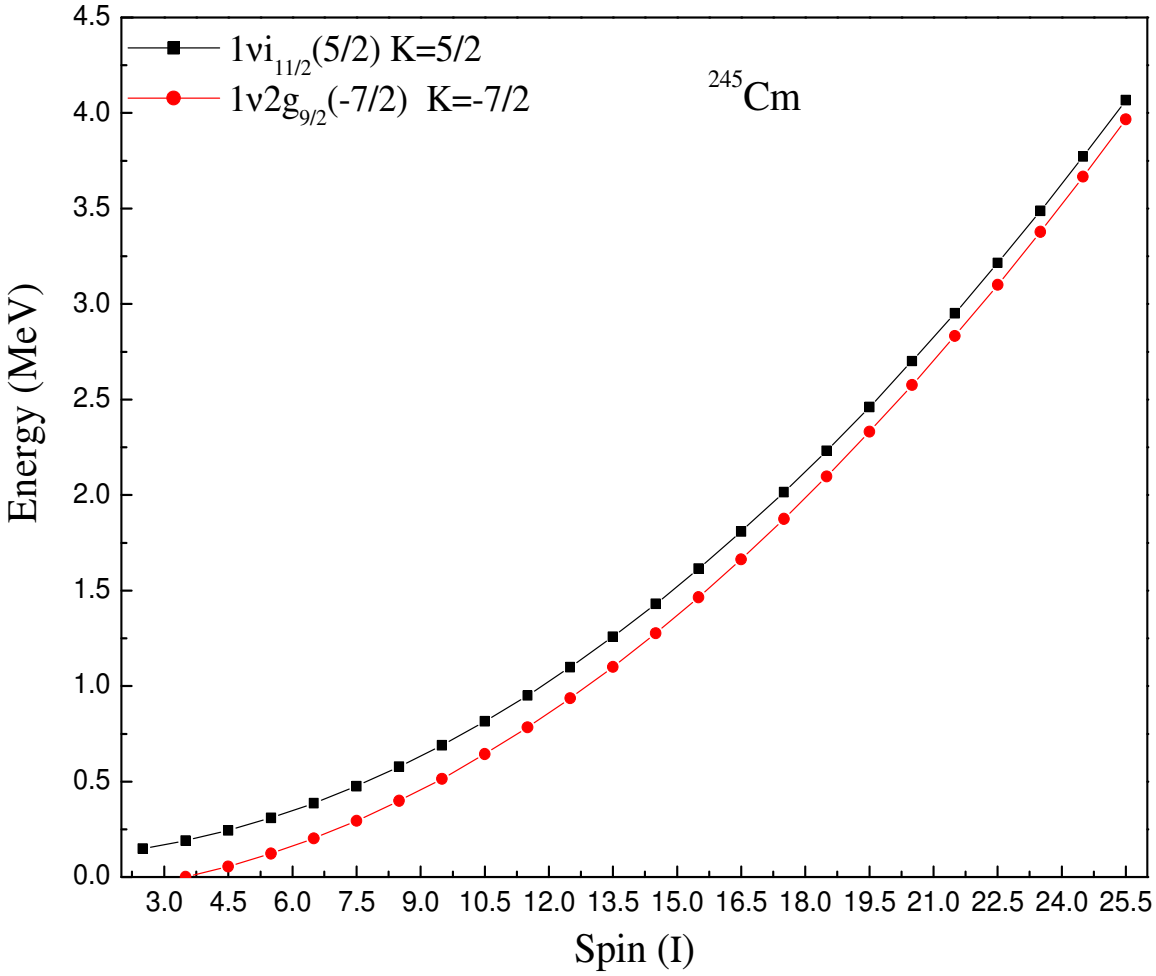

Fig. 3.9 Band diagram for ^{245}Cm.

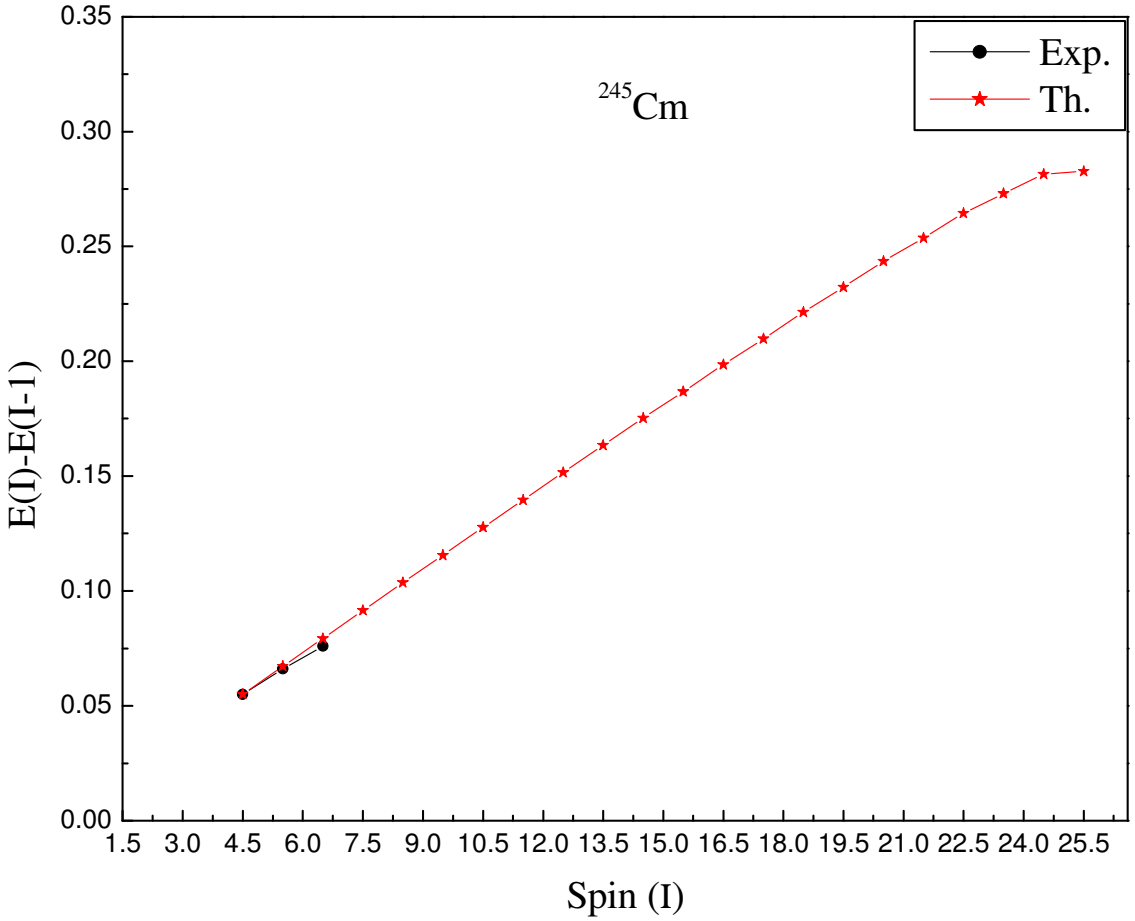

Fig. 3.10 Comparison of calculated (Th.) and experimental (Exp) transition energies [E(I)-E(I-1)] versus spin for ^{245}Cm.

.

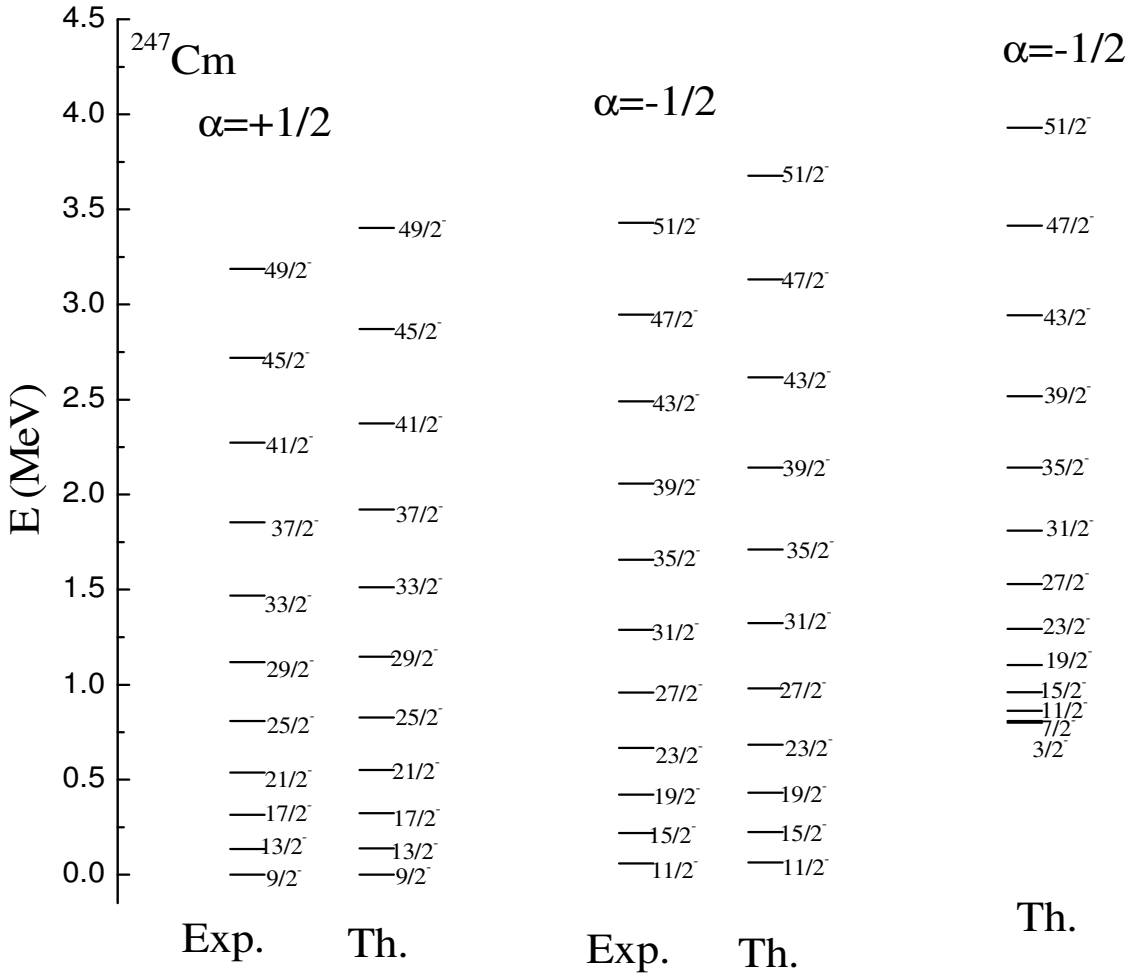

Fig. 3.11 Comparison of calculated (Th.) and experimental (Exp.) energy levels for ground state negative parity band of ^{247}Cm. The branch of band with signature α=-1/2 has not been as yet measured. However their energies are predicted. The experimental data are taken from Refs. [50,138].

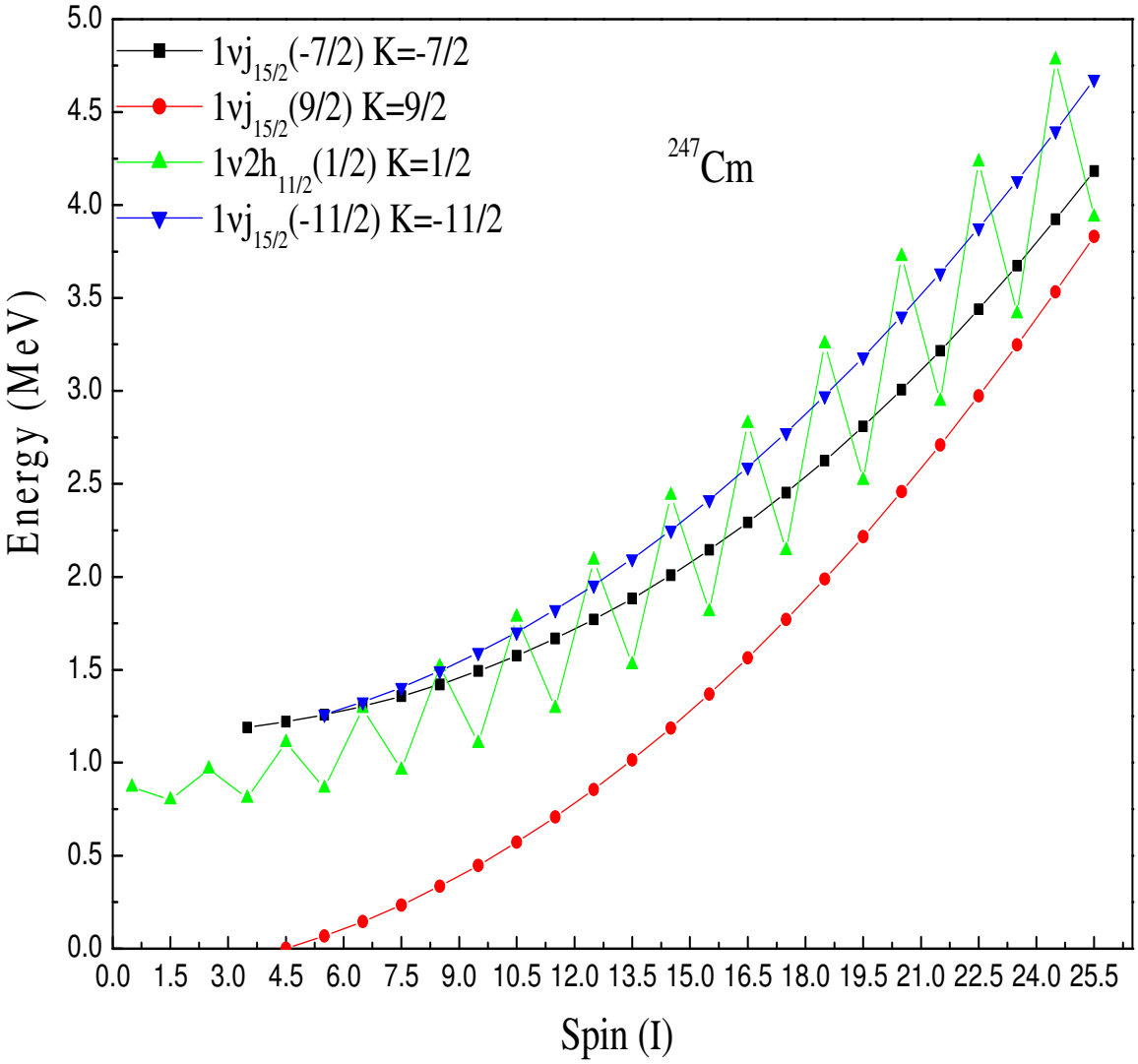

Fig. 3.12 Band diagram for ^{247}Cm.

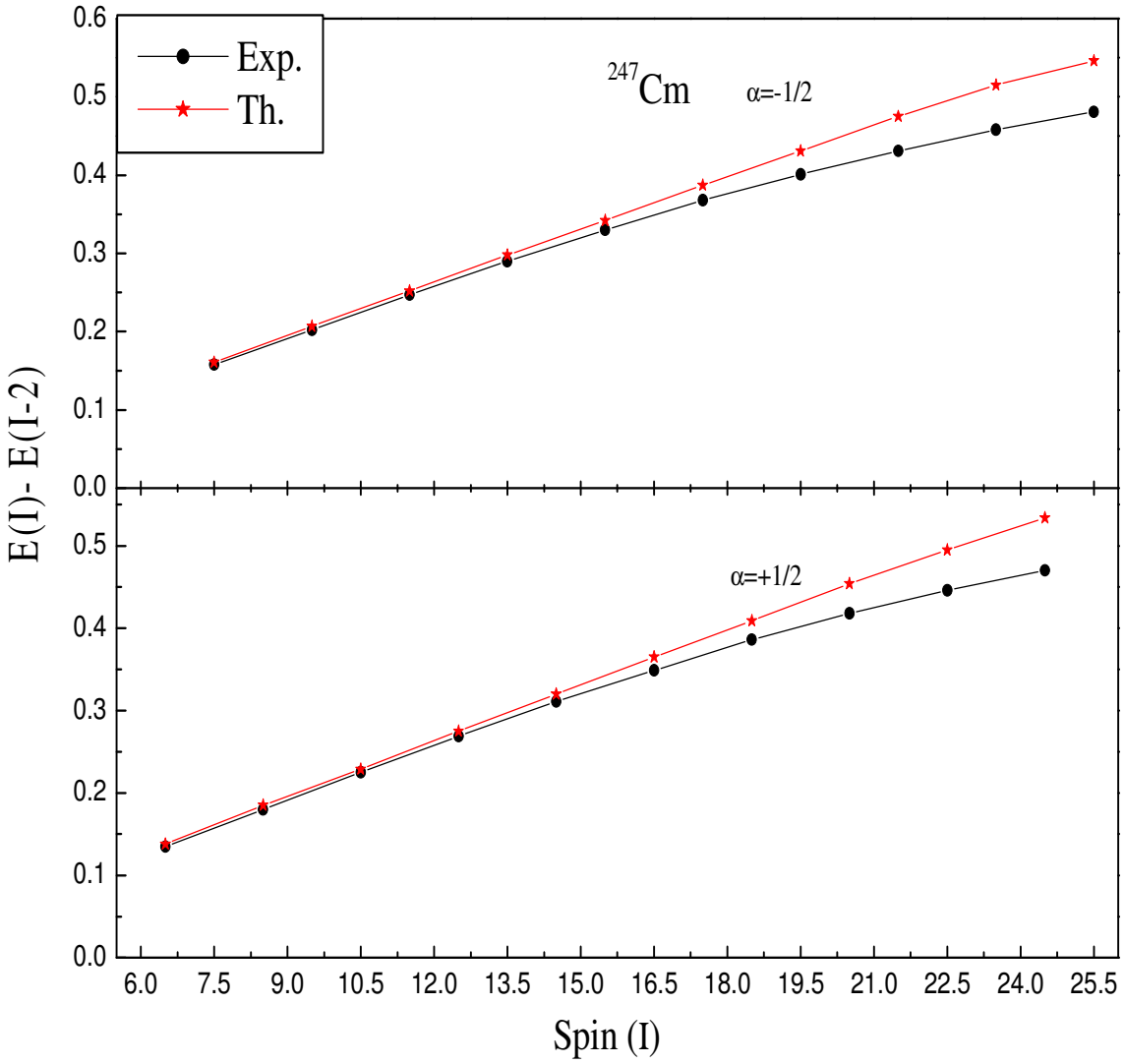

Fig. 3.13 Comparison of calculated (Th.) and experimental (Exp) transition energies [E(I)-E (I-2)] versus spin for ^{247}Cm. Exp. data taken from Refs. [50, 138].

Chapter 4

Summary of the work done

In this thesis a detailed study of some nuclei in the actinide mass region have been performed by using quadrupole-quadrupole plus monopole and quadrupole pairing force in the Hamiltonian within the framework of Projected Shell Model (PSM) approach. The results have been obtained for yrast levels, *B(E2)* transition probabilities and *g*-factors for even-even Uranium, Plutonium and Curium isotopes. The level energies and transition energies are also calculated for odd-A Curium isotopes.

Based on the research work presented in chapters 2 and 3, the following conclusions have been drawn:-

i. The projected shell model calculations performed with the quadrupole-quadrupole plus monopole and quadrupole pairing force reproduces correctly the observed deformation systematics in $^{230\text{-}240}$U and $^{236\text{-}242}$Pu isotopes. From the results of BCS subshell occupation numbers, it is seen that the observed deformation trends of low-lying states in U and Pu nuclei could be linked with the occupation of down-sloping components of high *j* orbits in the valence space.

ii. The experimental level schemes of positive parity yrast bands for $^{230\text{-}240}$U and $^{236\text{-}242}$Pu isotopes which are available up to spins 22^+, 20^+, 30^+, 30^+, 30^+, 12^+ and 16^+, 26^+, 30^+ 26^+ respectively, are reproduced by the PSM calculations. The maximum difference between the results of theory and experiment for highest known spins is 0.032, 0.210, 0.144, 0.019, 0.255, 0.067 MeV for $^{230\text{-}240}$U and 0.14, 0.019, 0.073, 0.286 MeV for $^{236\text{-}242}$Pu, respectively.

iii. The structure of the yrast bands of $^{230\text{-}240}$U and $^{236\text{-}242}$Pu investigated from band diagrams show that in the low spin region, the yrast states arise from 0-qp configuration in which all nucleons are paired. However, at the higher spins, the yrast bands have multi-quasiparticle structure i.e yrast band arise from 2-qp neutron and 2-qp proton bands.

iv. The calculated values of B(E2; $2_1^+ \rightarrow 0_1^+$) transition probability are in agreement with the available experimental data for all the $^{230\text{-}240}$U and $^{236\text{-}242}$Pu isotopes. In case of ^{236}U the experimental B(E2) values for higher transitions are available upto spin 20^+ which are also reproduced by the present calculation. The present calculation has predicted the B(E2) values for higher transitions for $^{230\text{-}234}$U, $^{238\text{-}240}$U and $^{236\text{-}242}$Pu isotopes.

v. In case of $^{230\text{-}232}$U the theoretical values of g-factors decrease at a certain spin, thereafter they show an increasing trend. In $^{234\text{-}240}$U isotopes, the theoretical values of g-factors show a reverse trend. In these isotopes the g-factors show an increase after the band crossing region due to the crossing of g-band by 2-qp proton bands. In case of ^{238}U, the theoretical values of g-factors follow the same trend as followed by the measured values and confirm the observed proton alignment in ^{238}U at higher spin.

vi. In case of $^{236\text{-}242}$Pu isotopes, the theoretical values of g-factors predict an increase at higher spins arising theoretically from the alignment of protons in $1i_{13/2}$ orbit. However, this feature in these isotopes remains to be verified experimentally.

vii. The experimental level schemes of positive parity yrast bands of $^{242\text{-}248}$Cm are available up to spins 26^+, 8^+, 26^+ and 30^+ respectively, which are reproduced by the PSM calculations. The maximum difference between theory and experiment for highest known spins is 0.34, 0.02, 0.57 and 1.04 MeV for $^{242\text{-}248}$Cm, respectively.

viii. The theoretical transition energies obtained for $^{242\text{-}248}$Cm, reproduces the available experimental data qualitatively.

ix. The structure of the yrast bands of $^{242\text{-}248}$Cm investigated from the band diagrams show that in the low spin region, the yrast states arise from 0-qp configuration in which all nucleons are paired. However, at the higher spin, the yrast bands have multi-quasiparticle structure.

x. The calculated values of B(E2; $2_1^+ \rightarrow 0_1^+$) transition probability are in agreement with the available experimental data for $^{244\text{-}248}$Cm isotopes. The experimental B(E2) values for higher transitions in ^{248}Cm are available upto spin 24^+ which are

reproduced by the present calculation. Besides, the present calculation has predicted the B(E2) values for higher transitions for $^{242\text{-}246}$Cm isotopes.

xi. The theoretical *g*-factors show an increasing trend in all the Curium isotopes. The small increase in the *g*-factors at higher spins in all these isotopes is due to crossing of *g*-band by 2-qp proton bands.

xii. Now coming to odd-A $^{243\text{-}245}$Cm, the theoretical values of energies of ground state and first excited state bands reproduce the available experimental data qualitatively. In case of ^{247}Cm the experimental level scheme of negative parity g-band is known upto spin 51/2 which is reproduced by the present calculation. The first excited negative parity band has also been predicted by the present calculation.

From the overall study, it is seen that the calculated results of band spectra and electromagnetic quantities are not in good agreement with the experimental data as one goes to higher spins. The reason for the discrepancy at the higher spins may be due to the assumption of fixed pairing used throughout the calculation of band spectra for all the nuclei. Besides this, the nuclei under study are known to have some degree of octupole deformation which has not been taken into consideration in the present study. Inclusion of these aspects will improve the agreement of theoretical results with the experimental data at higher spins.

Bibliography

[1] A. Bohr and B.R. Mottelson, Nuclear Structure, Vol II (Benjamin Inc., New Yrok, 1975).

[2] R.F. Casten, Nuclear Structure from a Simple Perspective, Second Edition (Oxford University Press, 2000).

[3] A. Guessous et al., Phys. Rev. Lett. **75**, 2280 (1995).

[4] X. Wu, A. Aprahamian, S.M. Fischer, W. Revoil, G. Liu and J.X. Saladin, Phys. Rev. C **49**, 1837 (1994).

[5] X. Wu, A. Aprahamian, S.M. Fischer, W. Revoil, G. Liu and J.X. Saladin, Phys. Lett. B **316**, 235 (1993).

[6] H.G. Borner, J. Jolei, S.J. Rabinson, B. Krusche, R. Piepenring, R.F. Lasten, A. Aprahamian and J.P. Draayer, Phys. Rev. Lett. **66**, 691 (1991).

[7] C. Baktash, J. X. Saladin, J.J. Obrien and J.G. Alessi, Phys. Rev. C **22,** 2383 (1980).

[8] K.J. Weeks and T. Tamura, Phys. Rev. Lett. **44**, 533 (1980).

[9] I.Y. Lee et al., Phys. Rev. C **12**, 1483 (1975).

[10] D.F. Winchell, M.S. Kaplan, J.X. Saladin, H. Takai, J.J. Kolata and J. Dudek, Phys. Rev. C **40**, 2672 (1989).

[11] D.F. Winchell, J. X. Saladin, M.S. Kaplan and H. Takai, Phys. Rev. C **41**, 1264 (1990).

[12] D.F. Winchell, L.Wehner, J.X. Saladin, M.S. Kaplan, E. Landulfo and A. Aprahamian, Phys. Rev. C **55,** 111 (1997).

[13] M.S. Kaplan, J.X. Saladin, D.F. Winchell, H. Takai and J. Dudek, Phys. Rev. C **44**, 668 (1991).

[14] F. Cristancho, J.X. Saladin, M.P. Metlay, W. Nazaewiez, C. Baktash, M. Halbert, I.Y. Lee, D.F. Fischer and M.K. Kabadiski, Phys. Rev. C **49**, 663 (1994).

[15] E. Landulfo et al., Phys. Rev. C **54**, 626 (1996).

[16] D.F. Winchell et al., Phys. Rev. C **61**, 044322 (2000).

[17] J.X. Saladin Proceeding of the International Conference on High Spin Physics and Gamma Soft Nuclei, World Scientific (1991).

[18] R. Boroda et al., Phys. Rev. Lett. **68**, 1671(1992).

[19] M. Schramm et al., Z. Phys. A **344**, 121(1992).

[20] M. Schramm et al., Z. Phys. A **344**, 363(1993).

[21] T. Pawlat et al., Nucl. Phys. A **574**, 623 (1994).

[22] B. Fornal et al., Phys. Rev. C **55**, 762 (1997).

[23] R. Boroda et al., Phys. Rev. Lett. **74**, 868 (1995).

[24] R. Boroda, P.Fornal, W. Krolas, T. Pawlet, J. Wrzesinski, D. Bazzacco, G.D. Angelis, S. Lunardi and C.R. Alvarez, Eur. Phys J. A **13**, 1 (2002).

[25] P.A. Butler, P.M. Jones, K.J. Cann, J.F.C. Cocks, G.d. Jones, R. Julin and W.H. Trzaska, Nucl. Instrum. Meth. A **381**, 433 (1996).

[26] H. Kankaanpaa et al., Nucl. Instrum. Meth. A **534**, 503 (2004).

[27] H. Mach, R.L. Gill and M. Moszynski, Nucl. Instrum. Meth. A **280**, 49(1989).

[28] M. Moszynski and H. Mach, Nucl. Instrum. Meth. A **277**, 407 (1989).

[29] H. Mach, F. L. Wohn, G. Molnar, K. Sistemich, J.C. Hell, M. Moszynski, R.J. Gill, W. Krips and D.S. Brenner, Nucl. Phys. A **523**, 197 (1991).

[30] R.D. Herzberg and P.T. Greenlees, Prog in Particles and Nuclear Physics **61**, 674 (2008).

[31] R.D. Herzberg and D. M. Cox, Radiochem Acta **99**, 441 (2011).

[32] H. Meldner, Arkiv fys. **36**, 593(1967).

[33] R. Smolanezuk and A. Sobiezewski, Proc. EPS Conf. Low energy Nuclear Dynamics, St Peterburg (Russia) April 18-22, Private Communication (1995).

[34] P. Moller, J.R. Nix, W.D. Myers and S.J. Swiatecki, At. Data. Nucl. Data Tables **59**, 185(1995).

[35] H. Ower et al., Nucl. Phys. A **388**, 421 (1982).

[36] D. Ward et al., Nucl. Phys. A **600**, 88 (1996).

[37] T. Ishii, S. Shigematsu, M. Asai, A. Makishima, M. Matsuda, J. Knaeko, I. Hossain, S. Ichikawa, T. Kohno and M. Ogawa, Phys. Rev. C **72**, 021301 (2005).

[38] T. Ishii et al., J. Phys. Soc. Jpn **75**, 043201 (2006).

[39] T. Ishii et al., Phys. of Atomic Nuclei **70**, 1457 (2007).

[40] O. Hausser et al., Phys. Rev. Lett. **48**, 383 (1982).

[41] I. Ahmad, M.P. Carpenter, R.R. Chasman, R.V.F. Janssens and T.L. Khoo, Phys. Rev. C **44**, 1204 (1991).

[42] R.S. Simon, R.P. Devito, H. Emling, R. Kulessa, C. Briancon and A.Lefebvre, Phys. Lett. B **108**, 87 (1982).

[43] E. Grosse et al., Phys. Scr. **24**, 337 (1981).

[44] W. Spreng et al., Phys. Rev. Lett. **51**, 1522 (1983).

[45] T. Czosnyka, D. Cline, L. Hasselgren and C.Y. Wu, R.M. Diamond, H. Kluge, C. Roulet, E.K. Hirlet, R.W. Lougheed and C. Baktash, Nucl. Phys. A **458**, 123 (1986).

[46] R.B. Piercey et al., Phys. Rev. Lett. **46**, 415 (1981).

[47] P. Reiter et al., Phys. Rev. Lett. **82**, 509 (1999).

[48] R.D. Herzberg et al., Phys. Rev. C **65**, 014303 (2001).

[49] J.L. Egido and L.M. Robledo, Phys. Rev. Lett. **85**, 1198 (2000).

[50] S.K. Tandel et al., Phys. Rev. C **82**, 041301(R) (2010).

[51] T.H. Braid, R.R. Chasman, J.R. Erskine and A.M. Friedman, Phys. Rev. C **4**, 247 (1971).

[52] S.S. Hota et al., Phys. Lett. B **739**, 13 (2014).

[53] I. Ahmed, R.R. Chasman, J.P. Greene, F.G. Kondev and E.F. Moore, Phys. Rev. C **68**, 044306 (2003).

[54] M.M. Abharam, L.A. Boatner, C.B. Finch, R.W. Reynolds and W.P. Unruh, Phys. Lett. A **44**, 527 (1973).

[55] S.W. Yates, I. Ahmed, A.M. Friedman, F.J. Lynch and R.E. Hollond, Phys. Rev. C **11**, 599 (1975).

[56] A. Sobiczewski, I. Muntain and Z. Patyk, Phys. Rev. C **63**, 034306 (2001).

[57] B. Nerlo-Pomorska, K. Pomorski and J. Bartel, Phys. Rev. C **84**, 044310 (2011).

[58] D. Vretenar, T. Niksic and P. Ring, Int. J. Mod. Phys. E **19**, 548 (2010).

[59] B. Kumar, S.K. Biswal, S.K. Singh, C. Lahiri and S.K. Patra, Int. J. Mod. Phys. E **25**, 1650020 (2016).

[60] T.M. Shneidman, G.G. Adamian, N.V. Antonenko and R.V. Jolos, Phys. Rev. C **74**, 034316 (2006).

[61] M. Brack, T. Ledergerber, H.C. Pauli and A.S. Jersen, Nucl. Phys. A **234**, 185 (1974).

[62] A.V. Afanasjev and O. Abdurazakov, Phys. Rev. C **88**, 014320 (2013).

[63] A.V. Afanasjev, Phys. Scr. **89**, 054001(2014).

[64] I. Muntian, Z. Patyk and A. Sobiczewski, Phys. Rev. C **60**, 041302 (1999).

[65] F.A. Khudair, G.L. Long and Y. Sun, Phys. Rev. C **79**, 034320 (2009).

[66] J.L. Egido and P. Ring, Nucl. Phys. A **423**, 93 (1984).

[67] H.C. Chiang, S.T. Hsieh and H.Z. Sun, Phys. Rev. C **49**, 1917 (1994).

[68] Z.H. Zhang, X.T. He, J.Y. Zeng, E.G. Zhoa and S.G. Zhou, Phys. Rev. C **85**, 014324 (2012).

[69] Z. H. Zhang, J.Y. Zeng, E.G. Zhao and S.G. Zhou, Phys. Rev. C **83**, 011304R (2011).

[70] A. Parkhomenko and A. Sobiczewski, Act. Phys. Pol. B **36**, 3115 (2005).

[71] M. Ploszajczak and A. Faesseler, J. Phys. G: Nucl. Phys. **8,** 709 (1982).

[72] N.Y. Shirikova, A.V. Sushkov, L.A. Malov and R.V. Jolos, Euro. Phys. J.A **51**, 21 (2015).

[73] S. Cwiok and W. Nazarewicz, Nucl. Phys. A **529**, 95 (1991).

[74] S. Hofmann and G. Munzenberg, Rev. Mod. Phys. **72**, 733 (2000).

[75] P. Armbruster, Annu. Rev. Nucl. Part. Sci.**50**, 411 (2000).

[76] S. Hofmann, Prog. Part. Nucl. Phys. **46**, 293 (2001).

[77] Y.T. Oganessian, Nucl. Phys. A**787**, 343c (2007).

[78] M. Leino and F.P. Hebberger, Annu. Rev. Nucl. Part. Sci. **54**, 175 (2004).

[79] R.D. Herzberg, J. Phys. G: Part. Phys. **30**, R123 (2004).

[80] P.T. Greenlees, Nucl. Phys. A **787**, 507c (2007).

[81] L.K. Peker, S. Pearlstein and J.H. Hamilton, Phys. Lett. B **100**, 281 (1981).

[82] M.S. Nadirbekov, G.A. Yuldasheva and V.Y. Denisov, Phys. Atomic Nuclei **78**, 215 (2015).

[83] M.S. Nadirbekov, N. Minkov, M. Strecker and W. Scheid, Int. J. Mod. Phys. E **25**, 1650022 (2016).

[84] L.I. Govor, A.M. Demodov, V.A. Kurkin and I.V. Mikhailov, Phys. of Atomic Nuclei **77**,131 (2014).

[85] A.I. Levon, P. Alexa, G. Grew, R. Hertenberger, S. Pascu, P.G. Thirolf and H.f. Wirth, Phys. Rev. C **92**, 064319 (2015).

[86] T.M. Shneidman, G.G. Adamin, N.V. Antonenko, R.V. Jolos and S.G. Zhou, Phys. Rev. C **92**, 034302 (2015).

[87] M. Diebel and U. Mosel, Z. Phys. A **303**, 131 (1981).

[88] K. Hara and Y. Sun, Int. J. Mod. Phys. E **4**, 637 (1995).

[89] B.A. Bian, Y.M. Di, G.L. Long, Y. Sun, J. Zhang, and J.A Sheikh, Phys. Rev. C **75**, 014312 (2007).

[90] C.J. Wei, Z.X. Rong, C.F. Qi, Y. Sun, W.C. Li, Chin. Phys. Lett. **2**, 022101 (2012).

[91] V.Velaquez, J.G. Hirsch, Y.Sun and M.W. Guidry, Nucl. Phys. A **653**, 355 (1999).

[92] V. Velaquez, J. G. Hirsch and Y. Sun, Nucl. Phys. A **643**, 39 (1998).

[93] Y. Sun and D. H. Feng, Phys. Rep. **264**, 375 (1996).

[94] Y.X. Lui, Y. Sun, X.Y. Zhou, Y.H. Zhang, S.Y. Yu, Y.C. Yang and H. Jin, Nucl. Phys. A **858**, 11 (2011).

[95] Y.Sun, Y.C. Yang, H.L. Lui, K. Kaneko, M. Haregewa and T. Mizusaki, Phys. Rev. C **80**, 054306 (2009).

[96] D. Ram, R. Devi and S.K. Khosa, Pramana J. Phys**. 80**, 953 (2013).

[97] Y. Sun and J.L. Egido, Nucl. Phys. A **580**, 1 (1994).

[98] M. Hamermesh, Group theory and its Applications to Physical Problems, Section 18, (Addison-Wesley, Reading, Massachusetts, 1964).

[99] A. Bohr and B.R. Mottelson, Nuclear Structure Vol. I (Benjanin, Inc., London, 1969).

[100] R.E. Pierls and I. Yoccoz, Proc. Phys. Soc. A **70,** 381 (1957).

[101] N. Onishi and S. Yoshida, Nucl. Phys. **80**, 367 (1966).

[102] N. Onishi and R.K. Sheline, S. Yoshida, Phys. Rev. C **2,** 1304 (1970).

[103] P. Rozmej, GSI Preprint 85-41(1985).

[104] S. Iwasaki and K. Hara, Phys. Lett. B **144**, 9 (1984).

[105] I.L. Lamm, Nucl. Phys. A **125**, 504 (1969).

[106] R. Bengtsson, Suppl. J. de Phys. **41**, C10 (1980).

[107] R.F. Casten, D. D. Warner, O. S. Brenner and R. L. Gill, Phys. Lett. **47**, 1433 (1981).

[108] E. Browne and J.K. Tuli, Nucl. Data Sheets **113**, 2113 (2012).

[109] E. Browne, Nucl. Data Sheets **107**, 2579 (2006).

[110] E. Browne and J.K. Tuli, Nucl. Data Sheets **108**, 681 (2007).

[111] E. Browne and J.K. Tuli, Nucl. Data Sheets **107**, 2649 (2006).

[112] E. Browne and J.K. Tuli, Nucl. Data Sheets **127**, 191 (2015).

[113] B. Singh and E. Browne, Nucl. Data Sheets **109**, 2439 (2008).

[114] Y.A. Akovali, Nucl. Data Sheets **96**, 177 (2002).

[115] B. Castel and I.S. Towner, Modern Theories of Nuclear Moments (Oxford-Clarendon, (1990).

[116] J. Rikovska et al., Phys. Rev. Lett. **85**, 1392 (2000).

[117] F.P. Hessberger, S. Hofman, D. Ackermann, P. Cagara, R.D. Herzberg, I. Kojouharov, P. Kuusiniemi, M. Leino and R. Mann, Eur. Phys. J. A **22**, 417 (2004).

[118] F.P. Hessberger et al., Eur. Phys. J. A **30**, 561(2006).

[119] F.P. Hessberger et al., Eur. Phys. J. A **12**, **57** (2001).

[120] B. Streicher et al., Eur. Phys. J. A **45**, 275(2010).

[121] A. Chatillon et al., Eur. Phys. J. A **30**, 397(2006).

[122] F.P. Hessberger et al., Eur. Phys. J. A **26**, 233 (2005).

[123] F.P. Hessberger, S. Antalic, D. Ackermann, S.Heinz, S. Hofmann, J. Khuyagbaatar, B. Kindler, I. Kojouharov, B. Lammel and R. Mann, Eur. Phys. J. A 43, 175 (2010).

[124] S. Antalic et al., Eur. Phys. J. A **43**, 35 (2010).

[125] Y. Oganessian, J. Phys. G **34**, R165 (2007).

[126] K. Pomorski and A. Sobiczewski, Acta. Phys. Pol. B **9,** 61 **(**1978).

[127] T.T. Ibrahim, S.M. Perez, S.M. Wyngardt, B. Buck and A.C. Merchant, Phys. Rev. C **85**, 044313 (2012).

[128] G.G. Adamian, N.V. Antonenko, S.N. Kuklin, B.N. Lu, L.A. Malav and S.G. Zhou Phys. Rev. C **84**, 024324 (2011).

[129] S. Sadiq, D. Ram, R. Devi and S. K. Khosa, Indian J. Phys. **89**, 713 (2015).

[130] Y. Sun, G.L. Long, F.A. Khudair and J.A. Sheikh, Phys. Rev. C **77**, 044307 (2008).

[131] K.A. Saleem, et al., Phys. Rev. C **70**, 024310 (2004).

[132] Y. A. Akovali, Nucl. Data Sheets **99**, 197 (2003).

[133] E. Browne, J. K. Tuli, Nucl. Data Sheets **112**, 1833 (2011).

[134] M. J. Martin, Nucl. Data Sheets **122**, 377 (2014).

[135] S. Raman, C.W. Nestor and P. Tikkanen, At. Data Nucl. Data Tables **78**, 1 (2001).

[136] C.D. Nesaraja, E.A. Maccutchan, Nucl. Data Sheets **121**, 695 (2014).

[137] E. Browne, J.K. Tuli, Nucl. Data Sheets **112**, 447 (2011).

[138] C.D. Nesaraja, Nucl. Data. Sheets **125**, 395 (2015).